

COMPUTATIONAL ADVANCES IN DATA-CONSISTENT INVERSION: MEASURE-THEORETIC
METHODS FOR PARAMETER ESTIMATION

by

MICHAEL PILOSOV

B.A., State University of New York: College at Geneseo, 2014

M.S., University of Colorado: Denver, 2017 Ph.D., University of Colorado: Denver, 2020

A thesis submitted to the
Faculty of the Graduate School of the
University of Colorado in partial fulfillment
of the requirements for the degree of
Doctor of Philosophy
Applied Mathematics Program
2020

This thesis for the Doctor of Philosophy degree by

Michael Pilosov

has been approved for the

Applied Mathematics Program

by

Dr. Stephen Billups, Chair

Dr. Troy Butler, Advisor

Dr. Varis Carey

Dr. Jan Mandel

Dr. Jimmy Kim

Date: December 12, 2020

Pilosov, Michael (Ph.D., Applied Mathematics)

Computational Advances in Data-Consistent Inversion: Measure-Theoretic Methods for Parameter Estimation

Thesis directed by Associate Professor Dr. Troy Butler

ABSTRACT

This work presents novel developments in the formulation and solution of stochastic inverse problems (SIPs) within a Data-Consistent Inversion (DCI) framework. This framework is grounded in measure theory. It leverages push-forward and pull-back measures to update initial descriptions of uncertainty. Consistent solutions are defined as distributions utilizing the ratios of observed and push-forward densities, which distinguishes DCI from the popular Bayesian approach of updating prior beliefs with likelihood functions.

A major contribution of this thesis is the extension of the DCI framework to address problems that seek to quantify uncertainties around a single “true” parameter from the aggregation and use of noisy data. Earlier developments focused on problems that quantified parameter variability inherent to natural processes (such as manufacturing or experimental setup), leaving no need to presume the existence of a single parameter value that explained variations in observational data. However, many scientific problems are inherently grounded in such a belief, which motivated this extension of the DCI framework to address such scenarios and providing a feasible alternative to Bayesian approaches.

This work sits at the intersection of applied mathematics, science, and computation. The scientific “laboratory” in which we perform the (simulated) experiments is the computer. A novel method whose implementation is difficult to use is unlikely to see widespread adoption, so in the interest of making this work as accessible as possible, a significant portion of this thesis is devoted to mathematical software development. This thesis demonstrates how open-source tools are leveraged and built to be made accessible to the broader scientific community.

The form and content of this abstract are approved. We recommend its publication.

Approved: Dr. Troy Butler

To Jacob and Anna Ratman.

ACKNOWLEDGEMENTS

I am indebted to Dr. Caroline Haddad, who first put the idea of pursuing graduate studies into my mind. Without her initial encouragement, I would have never started on this path. Jim Napolitano was the first mathematics teacher to seriously challenge and engage my skills, and did so at a time when my relationship with the subject was particularly fragile. I owe a thank you to Troy Butler, who was motivated to get all this finished even when I was not. If it were not his insistence on perfect not being the enemy of good, I would have kept refining this document indefinitely and never completed the program.

Thank you to Dr. Olympia Nicodemi for not giving up on me when I failed my first Real Analysis exam and spent every subsequent office hour patiently helping me compensate for my lack of proof-writing skills. Those sessions built a foundation that I desperately needed, and I will never forget the feeling of feeling frustrated outside your office while I did homework. Thank you to Dr. Gary Towsley, who bent some rules to ensure there was no lapse in my education, meeting with me at the town coffee shop every week to teach me Algebraic Geometry.

Thank you to the friends who have been by my side through too many late evenings to count. Making sure I would not let you down was a larger motivation at times than my own desire to finish. I have relied on y'all for perspective when I needed it most and am absolutely blessed to have you in my life. We're doing this in alphabetical order: Andrew, Christina, Daniel, Elliott, Gabriela, George, Govinda, Jordan, Joseph, Marta, Michael, Ron, Scott, Stephanie, Vincent.

And obviously, a very special thank you is reserved for my wonderful parents-Anna and Emil-for their love, support, and definitely for the grit that drove them to emigrate.

TABLE OF CONTENTS

CHAPTER

I. INTRODUCTION	1
1.1 Overview of Uncertainty Quantification	1
1.2 The Data-Consistent Framework	3
1.2.1 Terminology, notation, and the inverse problems	3
1.2.2 Problem Formulation and Solution	4
1.2.2.1 The Stochastic Inverse Problem (SIP)	5
1.2.2.2 The Deterministic Inverse Problem (DIP)	7
1.3 Comparing Inverse Problems and Solutions	8
1.3.0.1 The Bayesian Inverse Problem	8
1.3.1 Comparison of Data-Consistent and Bayesian Inversion	10
1.3.2 Illustrative Example	10
1.4 Properties and Assumptions of Consistent Update	14
1.4.1 Stability of the Consistent Solution	15
1.4.2 Numerical Approximation and Sampling	16
1.5 Towards a Reproducible Thesis	18
1.6 Outline of Remaining Chapters	20
II. DATA-DRIVEN MAPS AND CONSISTENT INVERSION FOR PARAMETER ESTIMATION	21
2.1 Comparing the Maximal Updated Density (MUD) and MAP points	21
2.1.1 MUD and MAP points for the “linear Gaussian” case	22
2.1.2 A Low-Dimensional Example	23
2.1.3 A Unifying Perspective and Closed Form Solutions	25
2.2 Higher-Dimensional Linear Gaussian Examples	27
2.2.1 Impact of Output Dimension	28
2.2.2 Impact of Rank: One Hundred (Deficient) $\mathbb{R}^{100 \times 100}$ matrices	30
2.3 Data-constructed QoI maps and MUD points	30

2.3.1 The Weighted Mean Error Map	31
2.3.2 Analysis of MUD point for the WME map	31
2.4 MUD points for nonlinear maps: Examples	32
2.4.1 ODE Example	33
2.4.2 PDE Example	35
2.4.3 Conclusions	38
III. GEOMETRY OF OUTPUT QUANTITIES AND CONSISTENT SOLUTIONS	40
3.1 A Brief Literature Review of Skewness	40
3.2 Set-Based Inversion for Consistent Measures	41
3.2.1 Numerical Approximation and Analysis	44
3.2.2 Descriptions of Error	45
3.2.3 Convergence	46
3.2.4 Accuracy of Set-Based Inversion	47
3.3 Numerical Results and Analysis	49
3.3.1 Overview of Examples	49
3.3.2 Rotational Invariance	51
3.3.3 Impact of Skewness on Accuracy	52
3.3.4 Dependence on Dimension	53
3.4 Conclusions	54
IV. EXTENSIONS AND APPLICATIONS OF MUD POINTS AND SKEWNESS	56
4.1 Skewness and Vector-Valued Data-Constructed QoI Maps	56
4.1.1 Revisiting Example 2.4.2	57
4.2 Extension to Higher Dimensions	60
4.2.1 A SIP with a Naive Initial Density	60
4.3 Improving Parameter Estimates by Solving Sequences of SIPs	62
4.3.1 Motivations for a New Initial Density	62
4.3.2 SIP Solutions using New Initial Density	64

4.3.3 Demonstration of Reduction in Uncertainty	65
4.4 Conclusions	66
V. CONCLUSIONS, FUTURE WORK, AND PRELIMINARY RESULTS	68
5.1 Concluding Remarks	68
5.2 Future Work and Preliminary Results	69
5.2.1 Optimal Experimental Design Considerations	69
5.2.2 Elliptic PDE Example	69
5.2.2.1 Uninformed Sensor Placement	70
5.2.2.2 Informed Sensor Placement	71
5.2.2.3 Comparison of SIP Solutions with Different QoI Maps	72
5.3 Sequential Inversion	73
5.3.1 Motivating Linear Example	74
5.3.2 Connection to Skewness	76
5.3.3 Comparisons and Convergence Results	76
REFERENCES	78
APPENDIX	
A. Proof of Lemma 1	81
B. ODE Example Revisited	83
2.1 Different Measurement Equipment	83
2.1.1 Impact of Equipment Precision	85
C. Description of Alternative 5-D Initial Density	87

LIST OF TABLES

TABLE

1.1 Updated density solving the SIP (left) and posterior density solving the Bayesian inverse problem (right)	10
2.1 Functionals to minimize to obtain λ that maximizes the updated PDF (bottom) and the Bayesian posterior PDF (top). Here, $T(\lambda)$ is the typical functional often associated with Tikhonov regularization, and the $J(\lambda)$ has an additional term subtracted from $T(\lambda)$ coming from the predicted density that serves as “unregularization” in data-informed directions.	23

LIST OF FIGURES

FIGURE

<p>1.1 (Left) The initial/prior PDF π_{in} (blue solid curve), updated PDF π_{up} (black dashed curve), and posterior PDF π_{post} (green dashed-dotted curve) on Λ. (Right) The push-forward (PF) of the initial/prior PDF π_{pr} (blue solid curve), observed/likelihood PDF (red solid curve), PF of the updated PDF π_{up} (black dashed curve), and the PF of the posterior PDF π_{post} (green dashed-dotted curve) for the QoI.</p> <p>1.2 (Top to Bottom): $S = 5, 10$, and, 20 samples are used to solve the SIP and DIP for comparison. (Left) The initial/prior PDF π_{in} (blue solid curve), updated PDF π_{up} (black dashed curve), and posterior PDF π_{post} (green dashed-dotted curve) on Λ. (Right) The push-forward (PF) of the initial/prior PDF π_{pr} (blue solid curve), observed/likelihood PDF (red solid curve), PF of the updated PDF π_{up} (black dashed curve), and the PF of the posterior PDF π_{post} (green dashed-dotted curve) for the QoI.</p> <p>2.1 Gaussian data mismatch over 2-D parameter space for a 2-to-1 linear map (left plots). Gaussian initial/prior lead to different regularization terms associated with updated/Bayesian PDFs (middle plots), which lead to different optimization functions (right plots) and parameter estimates that produce maximum PDF values for update/Bayesian PDF (red dot in right plots).</p> <p>2.2 Relative errors between λ^\dagger and (i) the least squares solution obtained through numpy's <code>linalg.pinv</code> module, (ii) the closed-form solution for the MUD point given in Eq (2.1.16), and (iii) the MAP point. (Left): Error for increasing dimensions of D for A taken to be a Gaussian Random Map. (Right): Error for increasing row-rank of A, generated with Gaussian vectors and a SVD.</p> <p>2.3 Curves for exponential decay model with various decay coefficients. Dashed curves denote 99% probability intervals for noise. The true signal is shown in solid black. Curves associated with the MUD estimates for the decay coefficient computed from 20 trials are shown in light red. Both sets of these curves encompass the true signal for $N = 20$ (top plot) and $N = 200$ (bottom plot) data points. The light red curves are almost indistinguishable in the bottom plot as they all lie nearly on the true signal which demonstrates the overall reduction in variance in MUD estimates around the true signal when using $N = 200$ data points.</p> <p>2.4 The mean (left) and variance (right) of absolute errors in MUD estimates as a function of the number of data points used. These statistics are computed over 20 trials.</p> <p>2.5 A representative noisy perturbation of the reference response surface. Locations of the randomly chosen spatial data used to construct both Q_{1D} and Q_{2D} are shown as black and red dots.</p> <p>2.6 In the left plot, the reference $g(x_2)$ is shown as the solid black curve with its interpolant onto the spline basis shown as a dotted red curve. The dashed blue line represents the sample from parameter space which most closely predicts noiseless data, which we refer to as the projection of g. The purple curves in the center and right plots show the variability in MUD estimates of $g(x_2)$ for the 20 different realizations of noisy data. The center plot uses Q_{1D} and the right plot uses Q_{2D} to construct the MUD estimates.</p> <p>2.7 A plot of the variance in 2-norm of MUD solutions acquired from solving the SIP with Q_{1D} and Q_{2D} as more measurements are incorporated. The solid black line represents Q_{1D} and the dashed blue line represents Q_{2D}.</p>	<p>11</p> <p>13</p> <p>24</p> <p>29</p> <p>34</p> <p>35</p> <p>37</p> <p>37</p> <p>38</p>
---	---

3.1	The first step (S1) defines (i) the formulation of the SIP by specification of the model, (ii) the measure spaces of parameters and (iii) observable outputs, and (iv) the probability measure on the latter. The second step (S2) defines a unique solution to the SIP on the space Λ equipped with the contour σ -algebra \mathcal{C}_Λ using the definition of the push-forward measure. In (S3), the Disintegration Theorem and Ansatz are applied to define a unique solution on the space of interest $(\Lambda, \mathcal{B}_\Lambda)$ equipped with a probability measure \mathbb{P}_Λ	42
3.2	Voronoi-cell discretization (partition) induced by $N = 25$ uniform i.i.d. random samples in $\Lambda = [0, 1]^2$	45
3.3	Two different Voronoi partitions induced by $N_1 = N_2 = 25$ uniform i.i.d. random samples.	48
3.4	(Left/Right): The two partitions from Figure 3.3 will be projected onto a third reference partition (center), in order to compare them on a common σ -algebra. Center: A possibly over-resolved reference sample set, generated using $N = 500$ uniform i.i.d. random samples.	50
3.5	The results of $d_{\text{TV}}^2(\mathbb{P}_{\Lambda, M, N}, \mathbb{P}_{\Lambda, \bar{N}})$ for three maps generated by random rotations of orthogonal linear maps.	52
3.6	The results of $d_{\text{TV}}^2(\mathbb{P}_{\Lambda, M, N}, \mathbb{P}_{\Lambda, M, \bar{N}})$ for $M = 1, \bar{N} = 40,000$, with $a, b, c = 1, 2, 4$ in two dimensions.	53
3.7	The results of $d_{\text{TV}}^2(\mathbb{P}_{\Lambda, M, N}, \mathbb{P}_{\Lambda, M, \bar{N}})$ for $M = 1, \bar{N} = 8,000,000$, with $a, b, c = 1, 2, 4$ in three dimensions.	54
4.1	Comparison of Q_{2D} (left) and Q'_{2D} (right). Partitioning of Ω into the two components of each map is shown in the top half of the figure. In the bottom half, the vector-valued QoI map is constructed for all $N = 1000$ parameter evaluations using $D = 20, 60$, and 100 measurements, and the two resulting component vectors are plotted against one another for both methods of partitioning Ω	58
4.2	Side-by-side comparison of an example solution to the SIP using Q_{1D} (left) compared to using Q'_{2D} , juxtaposed against a plot of g	59
4.3	One thousand initial parameter samples (our model evaluation “bugdet”) were used to estimate g , constructed by taking independent uniform samples from $[-4, 0]$ for each direction are shown in purple.	61
4.4	(Left): Layout for 5-D vector-valued map and comparison of the two MUD solutions in parameter space. (Right): Example MUD solutions for Q_{5D} and Q_{1D}	61
4.5	SIP solutions using Q_{5D} and Q_{1D} for twenty realizations of noise polluting the hundred measurements used to construct the map. (Left): Scalar-valued solutions. (Right): Vector-valued solutions.	62
4.6	100 measurements are used to solve the SIP for the PDE problem with Q_{1D} and Q_{2D}	63
4.7	Initial density constructed for the second attempt at the five-dimensional inverse problem, with the structure of solutions learned from the 2-D example incorporated into the selection of bounds in each direction.	64
4.8	Solutions to the SIP using one hundred measurements for $D = 20$ (top) and 100 (bottom). (Left): Scalar-valued solutions for alternative approach to the five-dimensional problem. (Right): Vector-valued solutions.	65

4.9	Comparison of the 2D initial errors to the 5D ones, as well as the reduction of uncertainty that solving a SIP problem for each provides.	66
5.1	(Left): The function response surface for u solving (5.2.1) with $S = 100$ measurement locations highlighted in white. The twenty most sensitive location markers are filled. (Right): The derivative $\partial M_i / \partial \lambda$ is computed for the 100 measurement locations and the distribution of the resulting collection of slopes is plotted. (Center): The values of the response surface at the measurements is shown. The true parameter value λ^\dagger is highlighted with a vertical line, and the values of the response surface conditioned on λ^\dagger are used to form the histogram plotted vertically on the right. Many measurements are near zero.	71
5.2	The same panels as in Figure 5.1 but for the placement of sensors informed by the observations about sensitivity incorporated into the experimental design. The alternative placement eliminates redundancy induced by the symmetry of the response surface, and is concentrated in the regions which exhibit more sensitivity to changes in λ . As a result of these choices, we observe less measurements near zero (bottom histogram), and slopes with larger magnitude (top).	72
5.3	Convergence of the MUD point (given $N = 1E3$ model evaluations) for increasing numbers of observations for randomly placed sensors. We observe similar rates of convergence for both arrangements of measurement locations, with a marked improvement in both accuracy and precision when an informed placement is used.	73
5.4	Dotted lines show the solution contours for each row of the operator A . (Left): First epoch for iterating through 10 QoI. (Right): Three more epochs allows our estimate to get much closer to the true value.	75
5.5	Iterating through five epochs of two QoI, each formed by picking two of the ten available rows of A at random. The random directions chosen on the left exhibit more redundancy than those on the right, so the same amount of iteration results in less accuracy.	75
5.6	(Left): Iterating through a single epoch with a QoI formed by picking rows of A which exhibit mutual orthogonality. (Right): Iterating through the rows of A at a random order for a single epoch results in considerably more accuracy than doing so in the original order of rows of A	76
5.7	Twenty different initial means are chosen and iterated on for three approaches. Individual experiments are transparent and the mean error is shown as solid lines. In the <i>Ordered</i> approach, we iterate through the rows of A as they are given to us for ten epochs. <i>Shuffled QoI</i> refers to establishing a different random ordering of the rows of A for each trial, and then using this ordering for ten epochs. Finally, in the <i>Random QoI</i> approach, we choose a QoI at random for each of 100 iterations, where the ordering still ensures each row gets used ten times, representing the same overall set of inverse problems solved as the other two.	77
2.1	Gray lines are the initial parameter samples. The true signal (black) is well-recovered by the MUD estimates (red). (Top): First twenty measurements used to solve the original problem. (Middle): First twenty measurements used to solve the alternative problem. (Bottom): The entire value λ_i ($1 \leq i \leq N$), in the sampled parameter set.	84
2.2	Convergence of the MUD point given $N = 1E3$ model evaluations for increasing numbers of observations for randomly placed sensors. Convergence rates are estimated using first-order linear regressions in \log_{10} -space. 100Hz equipment demonstrates a reduction of uncertainty and improvement in precision as S increases towards 200. We observe the same rates of convergence for the alternative equipment and note the (slightly) lower overall error for equal numbers of measurements ($S = 200$ corresponding to $t \in (1, 2)$ in this formulation).	85

2.3	Convergence of the MUD point given $N = 1E3$ model evaluations incorporating measurements at a fixed point in time. As more precise measurements are incorporated, the accuracy and precision of the MUD solution improves.	86
3.1	Knowledge of the behavior of g at the boundaries allows for more than half of each of the three remaining intervals in five dimensions to be ruled out as infeasible regions when we look at high-probability samples from the 2-D SIP solution.	87
3.2	Generating proposal samples for the two directions informed by solving the 2-D inverse problem, aided by singular-value decompositions and an ad-hoc sampling procedure.	88

CHAPTER I

INTRODUCTION

1.1 Overview of Uncertainty Quantification

In the last several decades, there has been an increasing reliance on quantitative predictions from computational, simulation-based models of physical systems to inform engineering design, predict the behavior of physical systems, and even shape public policy, e.g., see O’Malley and Vesselinov (2015b,a); Mattis *et al.* (2015a); Harp and Vesselinov (2013), for just a few such examples. It is therefore more important than ever to quantify, and whenever possible, reduce, the uncertainties impacting such models. Unfortunately, many key characteristics governing system behavior, described as model inputs (referred to here as parameters), are often hidden from direct observation. When observable model output data are sensitive to variations in these parameters, we formulate and solve inverse problems using the output data to quantify uncertainties in parameters. Inverse problems therefore play a vital role in the uncertainty quantification (UQ) community.

In UQ, uncertainties are categorized as being either aleatoric (i.e., irreducible) or epistemic (i.e., reducible) in nature, which are often quantitatively described and interpreted in distinct ways. Below, we use abstractions of conceptual examples to distinguish how both types of uncertainties arise in parameters, and subsequently impact the type of inverse problem that is solved to quantify these uncertainties. This distinction further serves to highlight the contributions of this thesis.

Consider modeling the manufacturing process of an engineered system involving various electrical or mechanical components. The intrinsic variability in component properties, e.g., due to impurities in raw materials used in their construction, are aleatoric in nature. Component properties define a sample space (the set of all possible outcomes), and combining this sample space with a description of measurable events along with a probability measure defines a probability space. Scalar-valued model parameters associated with component properties defines a random vector (i.e., a measurable function) from this probability space of components into the parameters required by the model. Subsequently, the mapping from parameters to observable model outputs defines what we refer to as a Quantities of Interest (QoI) map. Observation of a probability measure on the range of the QoI map leads to the formulation of a stochastic inverse problem (SIP), where the goal is to pullback the observed probability measure onto the space of parameters. Conceptually, a pullback measure is data-consistent in the sense that its push-forward through the QoI map matches the observed probability measure.

While it is possible to construct explicit approximations to data-consistent measures in terms of estimating measurable events and their probabilities in the parameter space (e.g., see Butler *et al.*

(2014a)), such “set-based” approximations become computationally intractable for high-dimensional parameter spaces or geometrically complex and/or computationally expensive QoI maps. A recently developed density-based approach (Butler *et al.*, 2018a,b, 2020) solves the SIP in a novel way by first solving a stochastic forward problem (SFP). Specifically, an *initial* probability measure is first specified on the parameters to encode any prior knowledge of parameter variability. Then, a SFP is solved where the push-forward of the initial probability measure is used to define a *predicted* probability measure on the QoI. The discrepancy between the predicted and *observed* probability measures on the QoI, expressed as a ratio of probability density functions (more generally, Radon-Nikodym derivatives), is then used to *update* the initial probability density. The *updated* probability measure associated with this density is then data-consistent. Moreover, the updates to the initial probability measure only occur in directions informed by the QoI. In other words, the initial probability measure serves to regularize the space of all pullback measures solving the SIP to produce a unique solution.

The SIP and its solution methodologies are based on rigorous measure theory using the Disintegration Theorem (Dellacherie and Meyer, 1978; Change and Pollard, 1997) as the central tool in establishing existence, uniqueness, and stability of solutions. Updated probability measures often have complex structures that are not well approximated by a family of parametrically defined distributions (e.g., Gaussian). This attribute of the solution further distinguishes this measure-theoretic approach from typical Bayesian-inspired approaches, e.g., Hierarchical Bayesian methods (Smith, 2013; Tarantola, 2005; Wikle *et al.*, 1998), that specify prior distributions from a parametric family of distributions along with additional prior distributions on the so-called hyper-parameters introduced by this parametric family (e.g., the means and variances of a Gaussian). Subsequently, solutions to the SIP using Bayesian approaches will not, in general, produce solutions (defined as posterior distributions) whose push-forward matches the observed distribution. In fact, the push-forward of the posterior is not even of general interest in most Bayesian paradigms. Instead, the posterior predictive, which defines the distribution of possible unobserved values is of central interest (Smith, 2013). The posterior predictive is constructed as a conditional distribution on the observations but makes practical use of the posterior through a marginalization. These differences are actually not surprising when one considers that the Bayesian inverse problem that is perhaps most familiar in the UQ community solves an inverse problem involving epistemic uncertainty, as we describe below and expand upon in Section 1.3.

In a typical Bayesian framework (Fitzpatrick, 1991; Kennedy and O’Hagan, 2001; Tarantola, 2005; Marzouk *et al.*, 2007; Cotter *et al.*, 2010; Stark and Tenorio, 2010; Alexanderian *et al.*, 2014; Bui-Thanh and Ghattas, 2014; Ernst *et al.*, 2014; Calvetti *et al.*, 2014; Cui *et al.*, 2016; Stuart, 2010; Cockayne *et al.*, 2017), one of the initial assumptions is that data obtained on a QoI are polluted by measurement error,

i.e., the data are “noisy.” Measurement errors can theoretically be reduced using improved measurement instruments (i.e., they are epistemic in nature). A data-likelihood function is used to express the relative likelihoods that all of the data came from a particular choice of the parameter. Encoding any initial assumptions about which parameters are more likely than others as a prior density allows the formal construction of a posterior density as a conditional density that describes the difference in relative likelihoods of any parameter value given the data.

It is common to use specific point estimators such as the maximum a posteriori (MAP) point given by the mode of the posterior as the actual solution to the inverse problem. The posterior is then re-interpreted as providing descriptions of uncertainty in that specific point estimate. The Bernstein-von Mises theorem (von Mises and Doob, 1941) provides conditions under which the posterior will become concentrated around the single true parameter in the limit of infinite data (Smith, 2013).

Returning to the hypothetical example of modeling a manufacturing process, the typical Bayesian paradigm described above is most applicable to a specific instance of the manufactured system. In other words, suppose a single system is extracted from the end of the production line. We subject this system to experiments for which we collect data on the system response, and we are interested in using this data to determine the precise parameter values associated with this single system. The Bayesian framework is fundamentally designed to address such a problem while the measure-theoretic framework as presented in Butler *et al.* (2018a,b, 2020) is not. The SIP is concerned with modeling the variability in the outputs of the production line as a collection, which is of particular interest to quality control.

The main contributions of this thesis are the extension of the SIP framework to address the reduction of epistemic uncertainty. This is accomplished by formulating parameter identification problems as ones involving pullbacks of distributions of residuals. In the following section we provide background and history for the SIP and subsequently define the Deterministic Inverse Problem (DIP), which is the term we use to refer to the problem addressed by the Bayesian framework. We then compare the two frameworks and provide some illustrative examples to draw attention to the key differences between them. The chapter will conclude with a summary of the assumptions, properties, and stability of the solutions to the SIP which will be considered throughout this thesis.

1.2 The Data-Consistent Framework

1.2.1 Terminology, notation, and the inverse problems

We provide a summary of the notation, definitions, problem-formulation, and assumptions that reoccur throughout this work. For more details on the original sources and derivations, we refer the interested reader to Butler *et al.* (2012); Butler and Estep (2013); Butler *et al.* (2014a, 2018a, 2020). To make

comparisons more clear, we first introduce shared notation between the SIP and Bayesian inverse problems.

Let u be the solution to a model, mathematically represented by $\mathcal{M}(u, \lambda) = 0$, where λ represents a parameter into such a model, e.g. the permeability of the medium in the subsurface through which a contaminant is spreading. Such parameters are often uncertain, and we begin the quantification of uncertainty by identifying the set of all physically plausible parameters denoted by $\Lambda \subset \mathbb{R}^P$. Since different choices of $\lambda \in \Lambda$ often lead to different model solutions, we write $u(\lambda)$ to make this dependence on the parameter space explicit.

In general, we cannot observe the entire solution $u(\lambda)$ due to practical limitations. For example, one cannot observe air pressure at every point throughout a room, but one can perform experiments and take measurements to infer pressure at specific locations within the room. Put more precisely, we are often limited in our ability to observe data related to some QoI that are mathematically defined as functionals of $u(\lambda)$. We let Q denote the (potentially vector-valued) QoI map from the solution space of the model to the space of observable data.

Then, given $\lambda \in \Lambda$, we obtain $u(\lambda)$ and compute $Q(u(\lambda))$ to get the QoI predicted by the model. The QoI map depends on λ through the dependency of u on λ , so we write $Q(\lambda)$ to simplify our notation. We generally assume this map is at least piecewise-differentiable. The data space $\mathcal{D} \subset \mathbb{R}^D$ is defined as the range of the QoI map Q , i.e.

$$\mathcal{D} = Q(\Lambda).$$

In other words, we use \mathcal{D} to denote the space of all physically plausible data for the QoI that the model can predict.

Let \mathcal{B}_Λ and $\mathcal{B}_{\mathcal{D}}$ denote (the Borel) σ -algebras on Λ and \mathcal{D} , respectively. A σ -algebra is a collection of subsets representing the set of all measurable events, i.e., events for which it makes sense to assign a probability. The map Q between measurable spaces $(\Lambda, \mathcal{B}_\Lambda)$ and $(\mathcal{D}, \mathcal{B}_{\mathcal{D}})$ is immediately measurable by the smoothness assumption. Then, equipping Λ and \mathcal{D} with (dominating) measures μ_Λ and $\mu_{\mathcal{D}}$, respectively, is the final necessary component for constructing the Radon–Nikodym derivatives defining probability density functions (pdfs) from probability measures defined on the measure spaces $(\Lambda, \mathcal{B}_\Lambda, \mu_\Lambda)$ and $(\mathcal{D}, \mathcal{B}_{\mathcal{D}}, \mu_{\mathcal{D}})$. In practice, μ_Λ and $\mu_{\mathcal{D}}$ are often taken to be Lebesgue measures when Λ and \mathcal{D} are finite-dimensional Butler *et al.* (2014a, 2018a). In general, these measure allow for the description of commonly known probability measures as familiar pdfs.

1.2.2 Problem Formulation and Solution

We begin with defining the types of forward and inverse problems considered in this thesis.

Definition 1 (Stochastic Forward Problem (SFP)). Given a probability measure \mathbb{P}_Λ on $(\Lambda, \mathcal{B}_\Lambda)$, and QoI map Q , the *stochastic forward problem* is to determine a measure, $\mathbb{P}_\mathcal{D}$, on $(\mathcal{D}, \mathcal{B}_\mathcal{D})$ that satisfies

$$\mathbb{P}_\mathcal{D}(E) = \mathbb{P}_\Lambda(Q^{-1}(E)), \quad \forall E \in \mathcal{B}_\mathcal{D}. \quad (1.2.1)$$

Definition 2 (Stochastic Inverse Problem (SIP)). Given a probability measure, $\mathbb{P}_\mathcal{D}$, on $(\mathcal{D}, \mathcal{B}_\mathcal{D})$ the *stochastic inverse problem* is to determine a probability measure, \mathbb{P}_Λ , on $(\Lambda, \mathcal{B}_\Lambda)$ satisfying

$$\mathbb{P}_\Lambda(Q^{-1}(E)) = \mathbb{P}_\mathcal{D}(E), \quad \forall E \in \mathcal{B}_\mathcal{D}. \quad (1.2.2)$$

Any probability measure \mathbb{P}_Λ satisfying (1.2.2) is referred to as a *consistent solution* to the inverse problem, and (1.2.2) is referred to as the *consistency condition*. If \mathbb{P}_Λ or $\mathbb{P}_\mathcal{D}$ are absolutely continuous with respect to μ_Λ or $\mu_\mathcal{D}$, respectively, then we write

$$\pi_\Lambda := \frac{d\mathbb{P}_\Lambda}{d\mu_\Lambda} \quad \text{or} \quad \pi_\mathcal{D} := \frac{d\mathbb{P}_\mathcal{D}}{d\mu_\mathcal{D}}$$

to denote the Radon-Nikodym derivatives (i.e., pdfs) of \mathbb{P}_Λ and $\mathbb{P}_\mathcal{D}$, respectively. In such a case, we can rewrite (1.2.1) and (1.2.2) using these pdfs. For example, here is a variant of (1.2.2) using these pdfs:

$$\mathbb{P}_\Lambda(Q^{-1}(E)) = \int_{Q^{-1}(E)} \pi_\Lambda(\lambda) d\mu_\Lambda = \int_E \pi_\mathcal{D}(Q(\lambda)) d\mu_\mathcal{D} = \mathbb{P}_\mathcal{D}(E), \quad \forall E \in \mathcal{B}_\mathcal{D}.$$

1.2.2.1 The Stochastic Inverse Problem (SIP)

In measure-theoretic terms, $\mathbb{P}_\mathcal{D}$ in Definition 1 is a push-forward measure of \mathbb{P}_Λ , and in Definition 2, \mathbb{P}_Λ is a pull-back measure of $\mathbb{P}_\mathcal{D}$. From the perspective of a forward problem, we seek \mathbb{P}_Λ such that its *push-forward measure is equivalent to $\mathbb{P}_\mathcal{D}$* . In other words, *the solution we seek to the inverse problem is constrained by a forward problem*. Below, we formalize some of the vocabulary involved in the formulation and solution of the SIP. We refine the concept of push-forward measures as solutions to the SFP mentioned in the introduction, formally introducing the requisite vocabulary of *initial*, *observed*, and densities. This helps frame the SIP more clearly as the direct inversion of the SFP.

Definition 3 (Observed Distribution). When the measure $\mathbb{P}_\mathcal{D}$ in (1.2.2) is defined by the quantitative characterization of uncertainty in the QoI data, it is referred to as the *observed measure*, \mathbb{P}_{ob} . If a domi-

nating measure $\mu_{\mathcal{D}}$ exists on $(\mathcal{D}, \mathcal{B}_{\mathcal{D}})$, the *observed density* π_{ob} is given by the Radon-Nikodym derivative of \mathbb{P}_{ob} with respect to the measure $\mu_{\mathcal{D}}$.

The map Q impacts the structure of any solution to the SIP since the underlying data space \mathcal{D} itself depends on Q . In the event that the map Q is a bijection, then the consistency condition (1.2.2) defines a unique measure \mathbb{P}_{Λ} given the specification of an observed density. However, there are many applications of interest where Q fails to be a bijection, either due to differences in the dimensions of the parameter and data spaces, nonlinearities inherent in the model itself, or both.

Therefore, we do not generally expect that there is a unique \mathbb{P}_{Λ} solving the SIP in Definition 2, but rather there is a class of pullback measures that solve the SIP. In Butler *et al.* (2014a), a disintegration theorem (Change and Pollard, 1997; Dellacherie and Meyer, 1978) along with an ansatz is used to establish the existence of solutions to the SIP that are unique up to the choice of ansatz. An algorithm is provided in Butler *et al.* (2014a) for explicitly approximating pullback measures by applying a specified ansatz to approximations of contour events, i.e., approximations of $Q^{-1}(E_i)$ where $\{E_i\}_{i \in \mathcal{I}}$ is a partitioning of \mathcal{D} according to some (finite) index set \mathcal{I} . In Butler *et al.* (2018a), a density-based approach is presented that is computationally simpler to implement, and scales well with increasing parameter dimension. The density-based approach makes explicit use of a solution to the SFP in constructing a solution to the SIP. We make use of the following definitions in this approach.

Definition 4 (Initial Distribution). When the measure \mathbb{P}_{Λ} in (1.2.1) is defined by the quantitative characterization of uncertainty in parameter variability before observations on QoI are taken into account, it is referred to as the initial measure \mathbb{P}_{in} . If a dominating measure μ_{Λ} exists on $(\Lambda, \mathcal{B}_{\Lambda})$, the *initial distribution* π_{in} is given by the Radon-Nikodym derivative of \mathbb{P}_{in} with respect to the measure μ_{Λ} .

To construct a density-based solution to the SIP, we first push-forward the initial density using the QoI map. In other words, we first solve the SFP of (1.2.1). We refer to the push-forward of the initial measure as the *predicted measure* since it may be constructed before any observed data are known. This also helps to distinguish it from the *observed* measure used in the formulation of the SIP. To make this precise, we use the following:

Definition 5 (Predicted Distribution). The push-forward density of π_{in} under the map Q is denoted as π_{pr} , and is referred to as the *predicted distribution* (or density). It is given as the Radon-Nikodym derivative (with respect to $\mu_{\mathcal{D}}$) of the push-forward probability measure (1.2.1) given by

$$\mathbb{P}_{\text{pr}}(E) = \mathbb{P}_{\text{in}}(Q^{-1}(E)), \quad \forall E \in \mathcal{B}_{\mathcal{D}}. \quad (1.2.3)$$

We now have all of the definitions required to summarize the density-based solution to the SIP, known as the *updated density* as:

$$\pi_{\text{up}}(\lambda) := \pi_{\text{in}}(\lambda) \frac{\pi_{\text{ob}}(Q(\lambda))}{\pi_{\text{pr}}(Q(\lambda))}. \quad (1.2.4)$$

We refer the interested reader to Butler *et al.* (2018a) for the theoretical and algorithmic details of implementing the solution to the SIP, though some are summarized in 1.4. For now, we note that the solution in (1.2.4) is stable with respect to perturbations in the initial and observed probability measures, and that the solution given by (1.2.4) requires only the forward-problem construction of π_{pr} , since π_{in} and π_{ob} are specified in the SIP. Additional properties of π_{up} are given in 1.4 alongside the conditions for the existence and uniqueness of π_{up} of the form given by (1.2.4).

In order to ensure that π_{up} is in fact a density, a predictability assumption is required Butler *et al.* (2018a). A practical form of the predictability assumption is that there exists a constant $C > 0$ such that $\pi_{\text{ob}}(q) \leq C \pi_{\text{pr}}(q)$ for a.e. $q \in \mathcal{D}$. Conceptually, we interpret the predictability assumption as stating that we are able to predict the observed data. This also helps to frame the special role of π_{in} in the SIP compared to the role of the prior density used in the Bayesian inverse problem that is discussed below. Specifically, π_{in} allows us to perform (1) robust predictions, and (2) define a particular data-consistent solution.

1.2.2.2 The Deterministic Inverse Problem (DIP)

A typical Bayesian approach to an inverse problem focuses on first modeling epistemic uncertainties in data on a QoI obtained from a true, but unknown, parameter value, which we denote by λ^\dagger . This is in contrast to the SIP and its data-consistent solutions that are defined as pullback measures of an observed probability measure on the QoI. To make the distinction between the two approaches more clear, we introduce the following two definitions to frame the problems addressed by the Bayesian framework:

Definition 6 (Deterministic Forward Problem (DFP)). Given a space Λ , and QoI map Q , the *deterministic forward problem* is to determine the values, $q \in \mathcal{D}$ that satisfy

$$q = Q(\lambda), \forall \lambda \in \Lambda. \quad (1.2.5)$$

Definition 7 (Deterministic Inverse Problem (DIP) Under Uncertainty). Given a noisy datum (or data-vector) $d = q + \xi$, $q \in \mathcal{D}$, the *deterministic inverse problem* is to determine the parameter $\lambda \in \Lambda$ which minimizes

$$\|Q(\lambda) - d\| \quad (1.2.6)$$

where ξ is a random variable (or vector) drawn from a distribution characterizing the uncertainty in observations due to measurement errors.

In the above definition, ξ is some unobservable perturbation to the true output, arising from epistemic uncertainty (e.g. the precision of available measurement equipment). The Bayesian inversion framework is perhaps the most popular approach in the UQ community for incorporating uncertainties in inverse solutions. As mentioned in the introduction, the data-consistent framework developed in Butler *et al.* (2018a,b, 2020) is designed to quantify aleatoric sources of uncertainty while the typical Bayesian framework (Fitzpatrick, 1991; Kennedy and O'Hagan, 2001; Marzouk *et al.*, 2007; Cotter *et al.*, 2010; Stark and Tenorio, 2010; Alexanderian *et al.*, 2014; Bui-Thanh and Ghattas, 2014; Ernst *et al.*, 2014; Calvetti *et al.*, 2014; Cui *et al.*, 2016; Stuart, 2010; Cockayne *et al.*, 2017) is designed to quantify epistemic sources of uncertainty. These conceptual differences have significant impacts on the solutions to inverse problems formulated within these distinctive frameworks. We provide more details in Section 1.3 to further clarify these impacts for the reader. Moreover, the details provided below play a vital role in Section 2.1 where features of the data-consistent framework are used to motivate its extension to parameter estimation problems.

1.3 Comparing Inverse Problems and Solutions

The objective of the Bayesian approach is to determine a single “true” parameter that explains all of the observed data (Smith, 2013; O. Aguilar and Tenorio, 2015; Allmaras *et al.*, 2013; Stuart, 2010; Tarantola, 2005). The philosophical underpinnings of Bayesian inference is akin to asking the following:

How does one incorporate collected data to shift prior beliefs about specific parameter values?

However, the Data-Consistent approach reflects the goal of constructing a distribution (or probability measure), which is akin to asking:

How does one update initial beliefs in such a way that the modified predictions match the description of uncertainty in observed data?

We now develop a typical Bayesian inverse problem following the framework described in Stuart (2010); Smith (2013), in order to make a formal comparison to the Data-Consistent SIP.

1.3.0.1 The Bayesian Inverse Problem

Let d denote the “noisy” data obtained on $Q(\lambda^\dagger)$, which is often represented as

$$d = Q(\lambda^\dagger) + \xi,$$

where ξ is a random variable used to model the measurement error that is often assumed to follow a Gaussian distribution. Then, the data-likelihood function, often written as a conditional density, $L_{\mathcal{D}}(q|\lambda)$, is formed. This describes the differences in relative likelihoods that the data could have been generated from a particular λ . Ideally, the largest values of $L_{\mathcal{D}}(q|\lambda)$ occur whenever λ is a close approximation of the true parameter λ^\dagger . The data-likelihood function is distinct from the observed density used in the data-consistent framework.

The next step in constructing a Bayesian inverse problem is the specification of a prior density denoted by $\pi_{\text{prior}}(\lambda)$. The prior describes the different relative likelihoods assumed for the true parameter before data are collected. This is also distinct from the role of the *initial* density used in the data-consistent framework.

The posterior density (i.e., the formal solution to the Bayesian inverse problem) is given by a conditional density, denoted by $\pi_{\text{post}}(\lambda|d)$, proportional to the product of the prior and data-likelihood function (R. Walpole and Ye, 2007; Berger, 1985; Allmaras *et al.*, 2013; Smith, 2013). In other words,

$$\pi_{\text{post}}(\lambda|q) \propto \pi_{\text{prior}}(\lambda)L_{\mathcal{D}}(q|\lambda)$$

This form of the density follows from Bayes' rule (not from the Disintegration Theorem as with the updated density). The posterior can be interrogated to assess the difference in relative likelihoods of a fixed parameter given the observed data. Subsequently, the posterior is often used to produce a “best” estimate of the true parameter. For example, the maximum a posteriori (MAP) point is the parameter that maximizes the posterior density.

Unlike the updated density, the posterior is often interrogated indirectly without knowledge of the normalizing constant C required to represent it as a density. In other words, the posterior is a density of the form

$$\pi_{\text{post}}(\lambda) := \pi_{\text{prior}}(\lambda) \frac{L_{\mathcal{D}}(q|\lambda)}{C}, \quad (1.3.1)$$

where we emphasize the use of π_{post} to distinguish the *posterior* from the updated density π_{up} in (1.2.4). Here, the denominator C (known as the *evidence* Smith (2013)), ensures the posterior density integrates to one, and is given by

$$C = \int_{\Lambda} \pi_{\text{prior}}(\lambda) L_{\mathcal{D}}(q|\lambda) d\lambda.$$

Note that there are no constraints or requirements that likelihood function be a density. In fact, $L_{\mathcal{D}}$ need not even be in $L^1(\Lambda)$ since it is actually only the product $\pi_{\text{prior}}(\lambda)L_{\mathcal{D}}(q|\lambda)$ that is required to

be in $L^1(\Lambda)$ to form a posterior. In other words, $L_{\mathcal{D}}(q|\lambda)$ and $\pi_{\text{ob}}(Q(\lambda))$ can model completely different things with respect to uncertainty in the data. As stated above, $L_{\mathcal{D}}(q|\lambda)$ is used to assess the relative likelihood that a single parameter $\lambda \in \Lambda$ explains all of the observed data, whereas $\pi_{\text{ob}}(Q(\lambda))$ describes the relative likelihood of a predicted datum associated with $\lambda \in \Lambda$. In the Bayesian framework, there is a different notion of consistency of solutions, referring to certain asymptotic properties of π_{post} in the limit of infinite data (Barron *et al.*, 1999; Silverman, 1986; Stark and Tenorio, 2010).

1.3.1 Comparison of Data-Consistent and Bayesian Inversion

We summarize the posterior and updated densities side-by-side in Table 1.1 and comment on a few notable aspects not mentioned above. Observe for the posterior density that the data-likelihood function appears in both the numerator and denominator. In particular, the data-likelihood function informs the normalizing constant, commonly referred to as the evidence term, in the denominator. This is in contrast to the denominator of the updated density, which is given by the predicted density, which is in general not a constant, and can be constructed independently of π_{ob} .

Table 1.1: Updated density solving the SIP (left) and posterior density solving the Bayesian inverse problem (right).

$\pi_{\text{up}}(\lambda) = \pi_{\text{in}}(\lambda) \frac{\pi_{\text{ob}}(q)}{\pi_{\text{pr}}(q)}$	$\pi_{\text{post}}(\lambda q) = \frac{\pi_{\text{prior}}(\lambda) L_{\mathcal{D}}(q \lambda)}{\int_{\Lambda} L_{\mathcal{D}}(q \lambda) \pi_{\text{prior}}(\lambda) d\mu_{\Lambda}}$
---	--

A practical implication of this difference is that the updated density only alters the structure of the initial density in what we refer to as the “data-informed” parameter directions. Specifically, for a fixed $q \in \mathcal{D}$, let $C_q := \{\lambda \in \Lambda : Q(\lambda) = q\}$, i.e., C_q is a “contour” in parameter space. Then, for any $\lambda \in C_q$, we immediately have $\pi_{\text{up}}(\lambda) = r(q) \pi_{\text{in}}(\lambda)$ where $r(q)$ is a fixed constant of proportionality for all $\lambda \in C_q$. By contrast, while the posterior does not have to agree with the prior in any direction in parameter space, the prior does impact the structure of the posterior in all directions.

The previous paragraph is not—and should not be interpreted as—a criticism of the Bayesian inverse framework. It is simply meant to highlight that the data-consistent and Bayesian frameworks formulate and solve inverse UQ problems from different perspectives and with different (although at times seemingly compatible) assumptions. Consequently, the solutions for an inverse problem formulated under either framework may differ significantly. As the example (adopted from Butler *et al.* (2018a,b)) below demonstrates, this is true even if we arbitrarily force the inverse problems to appear as similar as possible.

1.3.2 Illustrative Example

Despite the differences in the statistical interpretations, we formulate a problem where π_{ob} and π_{in} match the forms of $L_{\mathcal{D}}$ and π_{prior} . However, we still observe differences between π_{up} and π_{post} due to the use of a normalizing constant C in π_{post} and the use of π_{pr} in π_{up} . We explore the impact of this difference in the denominators of the solutions in the following example.

Example 1. Suppose $\Lambda = [-1, 1] \subset \mathbb{R}$ and $Q(\lambda) = \lambda^5$ so that $\mathcal{D} = [-1, 1]$. For the data-consistent framework, we assume $\pi_{\text{in}} \sim \mathcal{U}([-1, 1])$ and $\pi_{\text{ob}} \sim N(0.25, 0.1^2)$. The push-forward of initial PDF, the observed PDF, and the updated PDF are shown in Fig. 1.1.

For the Bayesian inverse problem, we assume $d \in \mathcal{D}$ with $d = Q(\lambda^\dagger) + \xi$ where $\xi \sim N(0, 0.1^2)$. We then construct $\pi_{\text{post}}(\lambda | d)$ for this example assuming a uniform prior (to match the initial density) with an assumed observed value of $d = 0.25$ so that the data-likelihood function matches the observed density. The posterior and its push-forward are also shown in Fig. 1.1.

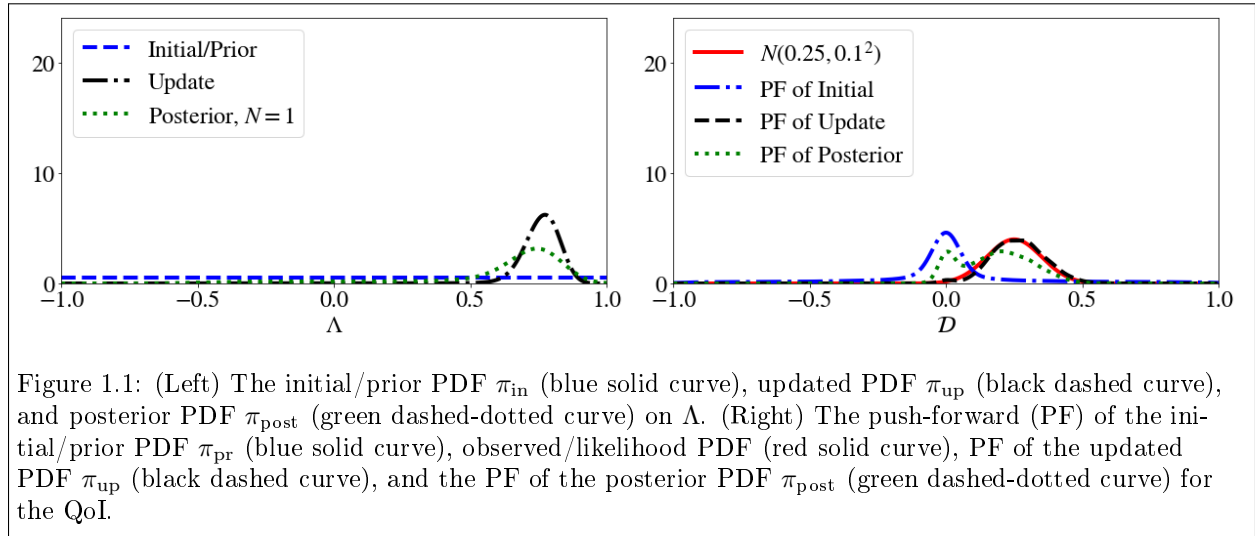


Figure 1.1: (Left) The initial/prior PDF π_{in} (blue solid curve), updated PDF π_{up} (black dashed curve), and posterior PDF π_{post} (green dashed-dotted curve) on Λ . (Right) The push-forward (PF) of the initial/prior PDF π_{pr} (blue solid curve), observed/likelihood PDF (red solid curve), PF of the updated PDF π_{up} (black dashed curve), and the PF of the posterior PDF π_{post} (green dashed-dotted curve) for the QoI.

While the updated and posterior densities in Fig. 1.1 share certain similarities (e.g., they are unimodal with similar locations of the mode), they are otherwise visibly distinct. The differences between these densities is made more evident by examining their push-forwards. The push-forward of the updated density agrees well with the observed density, which is to be expected. However, the push-forward of the posterior is bi-modal and does not match the observed density, which we recall is identical to the data-likelihood function in this case.

The takeaway to the above discussion and example is that each density is solving a *different* inverse problem. The posterior density is intended to provide point estimates of a true parameter value whereas the updated density is intended to quantitatively characterize natural variations in parameter val-

ues. We reformulate the previous example to make the role of data collection more central in the follow example.

Example 2. For the (Bayesian) Deterministic Inverse Problem, suppose $Q(\lambda^\dagger) = 0.25$ and noisy measurement data are drawn from a $N(0.25, 0.1^2)$, i.e., we assume that each datum is given by $d = Q(\lambda^\dagger) + \xi$ where $\xi \sim N(0, 0.1^2)$. For the SIP, we use the sample mean and variance of data to estimate the “exact” observed $N(0.25, 0.1^2)$ distribution. The observed density and data-likelihood become significantly different from one another as more data are collected. The data-likelihood is in fact given by a product of normal densities.

We draw $M = 5, 10$, and, 20 samples to form estimates of π_{ob} and the likelihood functions. We show the results in Figure 1.2.

For all values of M , the push-forward of the initial remains the same, and the push-forward of the update matches the observed. By contrast, the posterior increases in confidence alongside the predictions it produces. This further illustrates that the DIP and SIP are fundamentally different problems (they are addressing different questions). As more data are incorporated, the goal of the DIP is to reduce epistemic uncertainty; for the SIP, it is to quantify the aleatoric uncertainty.

In summary, it is not the goal of Bayesian inference to construct a pullback distribution. Bayesian inverse problems are fundamentally posed as parameter-identification problems, not distribution estimation problems. However, one could assume that a posterior on Λ can be expressed as a Gaussian distribution, and solve for the most likely mean and standard deviation that characterizes it (Smith, 2013; Tarantola, 2005). This defines what is commonly referred to as a Hierarchical Bayesian Inverse Problem.

More complex densities can be approximated by mixture models. For example, one can assume that the posterior can be given by a linear combination of four Gaussian distributions, and solve for eight parameter values (four standard deviations and means). However, the operative word here is *assume*; in order to capture a density using a Bayesian framework, one needs to impose some sort of explicit structure on the posterior. No such assumption is required in the DCI framework. Distributions (or measures) can be solved for directly, regardless of any nonlinear/non-parameteric structure by leveraging the measure-theoretic approaches described in Butler and Estep (2013) or Butler *et al.* (2018a).

It is important to note that Hierarchical Bayesian inverse problem still casts a distribution-estimation problem in the context of parameter identification. As a complementary line of reasoning, we seek to formulate a parameter identification problem in a DCI framework. For example, the mean of the updated density could be used as an estimator to address the parameter identification problem. However, collecting more data does not improve confidence if used to estimate π_{ob} as described above unless

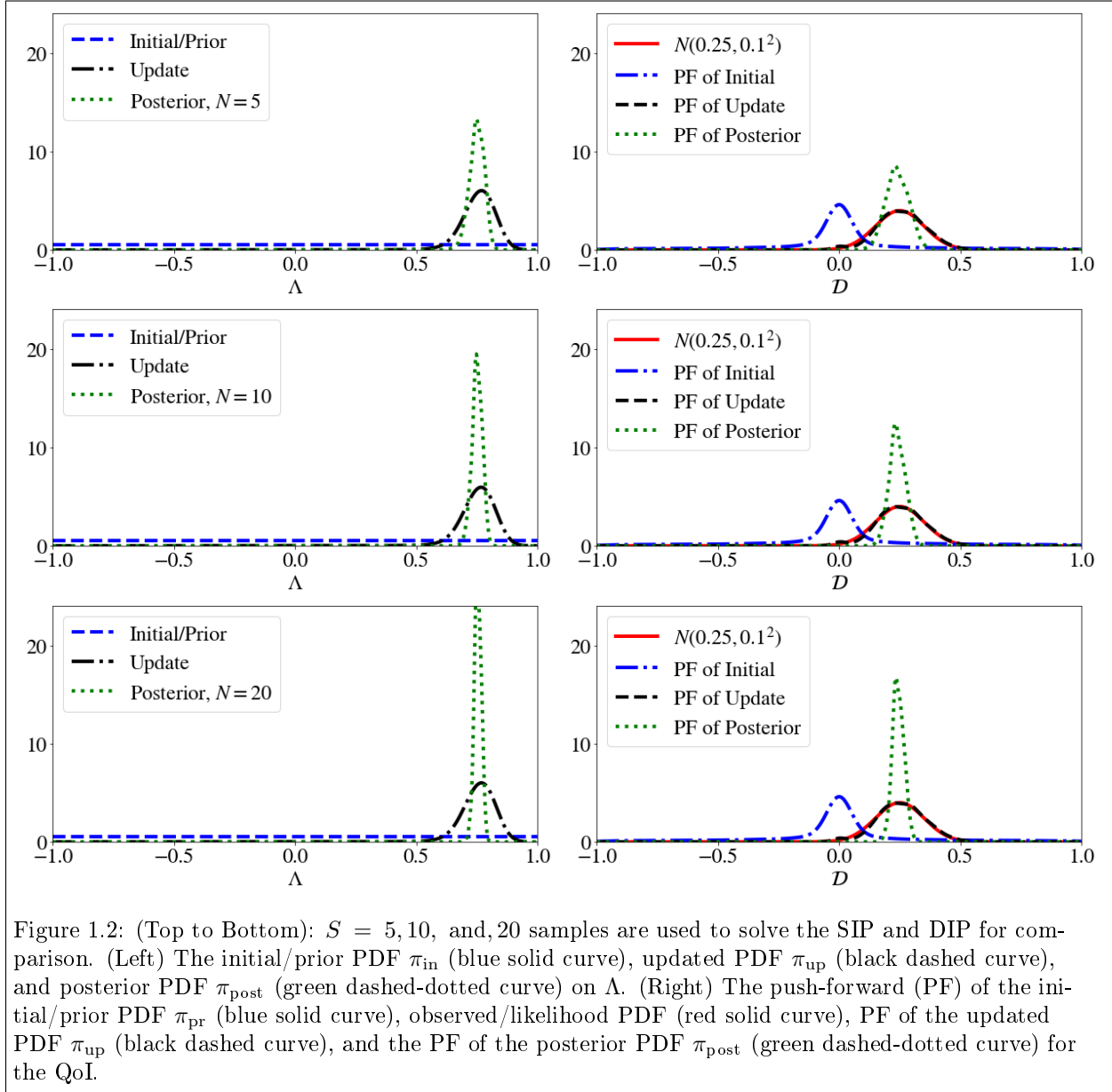


Figure 1.2: (Top to Bottom): $S = 5, 10$, and, 20 samples are used to solve the SIP and DIP for comparison. (Left) The initial/prior PDF π_{in} (blue solid curve), updated PDF π_{up} (black dashed curve), and posterior PDF π_{post} (green dashed-dotted curve) on Λ . (Right) The push-forward (PF) of the initial/prior PDF π_{pr} (blue solid curve), observed/likelihood PDF (red solid curve), PF of the updated PDF π_{up} (black dashed curve), and the PF of the posterior PDF π_{post} (green dashed-dotted curve) for the QoI.

we revisit the results with a focus on parameter estimation by considering alternative data-driven ways to construct the QoI (and subsequently π_{ob}).

In Chapter II, we motivate the use of the maximal updated density point (maximizing the update), as a means of providing a useful point estimate to parameters. Before we proceed, we finish summarizing key results about the stability and numerical convergence of the updated solution (1.2.4) in the next section.

1.4 Properties and Assumptions of Consistent Update

Recall that the SIP is defined as finding a measure \mathbb{P}_{Λ} such that the push-forward of it matched \mathbb{P}_{ob} . The following assumption guarantees the existence of a solution to the SIP in the form of an update to the initial distribution. It implies that any event which is assigned a positive probability by the observations must also have a positive predicted probability.

Assumption 1.4.1 (Predictability Assumption (Theoretical Form)). The measure associated with π_{ob} is absolutely continuous with respect to the measure associated with π_{ob} .

If this is unsatisfied, one source of information (the data) suggests certain events are probable while another source of information (the model and initial beliefs) have a priori ruled that almost surely these events should not occur. Therefore, either initial beliefs, the model under consideration, or the description of uncertainty encoded in π_{pr} should be subjected to a critical reevaluation.

The following establishes a more practical form (from the perspective of numerical implementation), of 1.4.1 which states that the predicted measure must dominate the observed.

Assumption 1.4.2 (Predictability Assumption (Practical Form)). The requirement given in Assumption 1.4.1 is guaranteed if the following is satisfied:

$$\exists C > 0 \text{ such that } \pi_{\text{ob}}(q) \leq C \pi_{\text{pr}}(q) \text{ for a.e. } d \in \mathcal{D}, \quad (1.4.1)$$

where it is understood that $q = Q(\lambda)$ for some $\lambda \in \Lambda$.

Assumption 1.4.2 is particularly useful in that it is the same condition required for applying rejection sampling, which we summarize in Algorithm 1. Specifically, this allows us to sample from the updated density using the initial density as follows:

Now, assuming (1.4.1) holds, we state the following theorem from Butler *et al.* (2018a) based upon the disintegration of measures:

Algorithm 1: Rejection Sampling Leveraging Ratio from Density-Based Approach

Draw N independent identically distributed (i.i.d.) initial samples from the initial density **for**
 $i = 1, \dots, N$ **do**
 └ Compute $(Q(\lambda_i)) = Q(\lambda^{(i)})$.
Approximate π_{pr} , the push-forward of π_{in} , by some method such as kernel density estimation. **for**
 $i = 1, \dots, N$ **do**
 └ Compute $r(\lambda_i) = \frac{\pi_{\text{ob}}(Q(\lambda_i))}{\pi_{\text{pr}}(Q(\lambda_i))}$.
Normalize r by dividing it by $\max(r)$. **for** $i = 1, \dots, N$ **do**
 └ Draw a sample from a standard uniform distribution. If the value of $r(\lambda_i)$ exceeds the value of
 the random sample, keep $r(\lambda_i)$.

Theorem 1.4.1 (Existence and Uniqueness). *For any set $A \in \mathcal{B}_\Lambda$, the probability measure \mathbb{P}_{up} defined by*

$$\mathbb{P}_{\text{up}}(A) = \int_{\mathcal{D}} \left(\int_{\Lambda \in Q^{-1}(q)} \pi_{\text{in}}(\lambda) \frac{\pi_{\text{ob}}(Q(\lambda))}{\pi_{\text{pr}}(Q(\lambda))} d\mu_{\Lambda,q}(\lambda) \right) d\mu_{\mathcal{D}}(q), \quad \forall A \in \mathcal{B}_\Lambda \quad (1.4.2)$$

is a consistent solution to the SIP given in (1.2.2), and is uniquely defined up to the specification of the initial probability measure π_{in} on $(\Lambda, \mathcal{B}_\Lambda)$. Here, $\mu_{\Lambda,d}$ denotes the disintegration of the dominating measure μ_Λ .

The updated density (1.4.3) in the iterated integral in (1.4.2) has no normalization constant because it is in fact a density (i.e., it integrates to 1), which is summarized in Corollary 3.1 in Butler *et al.* (2018a) and restated in simplified form below:

Corollary 1. $\mathbb{P}_{\text{up}}(\Lambda) = 1$.

These definitions are combined to identify the form of the *updated density*, originally derived in Butler *et al.* (2018a):

Definition 8 (Updated Distribution). A solution satisfying (1.4.2) is referred to as an updated distribution, with an updated density

$$\pi_{\text{up}}(\lambda) = \pi_{\text{in}}(\lambda) \frac{\pi_{\text{ob}}(Q(\lambda))}{\pi_{\text{pr}}(Q(\lambda))}, \quad \forall \lambda \in \Lambda. \quad (1.4.3)$$

1.4.1 Stability of the Consistent Solution

The Total Variation (TV) metric on a space of probability measures, absolutely continuous with respect to a dominating measure μ , is defined as

$$d_{\text{TV}}(\mathbb{P}_f, \mathbb{P}_g) := \int |\pi_f - \pi_g| d\mu, \quad (1.4.4)$$

where π_f, π_g are the densities (Radon-Nikodym derivatives with respect to μ), associated with measures $\mathbb{P}_f, \mathbb{P}_g$, respectively. The stability results below are all with respect to the TV metric, which is widely used in the literature and is also known as *statistical distance* (Gibbs and Su, 2002; Smith, 2013; Silverman, 1986). We first define stability with respect to perturbations in the data.

Definition 9 (Stability of Updated Densities I). Given \mathbb{P}_{in} and \mathbb{P}_{ob} , let $\widehat{\mathbb{P}}_{\text{ob}}$ be any perturbation to \mathbb{P}_{ob} on $(\mathcal{D}, \mathcal{B}_{\mathcal{D}})$ satisfying (1.4.1). Let \mathbb{P}_{up} and $\widehat{\mathbb{P}}_{\text{up}}$ denote the consistent solutions associated with \mathbb{P}_{ob} and $\widehat{\mathbb{P}}_{\text{ob}}$, respectively. We say that \mathbb{P}_{up} is *stable* with respect to perturbations in \mathbb{P}_{ob} if for all $\varepsilon > 0$, there exists a $\delta > 0$ such that

$$d_{\text{TV}}(\mathbb{P}_{\text{ob}}, \widehat{\mathbb{P}}_{\text{ob}}) < \delta \implies d_{\text{TV}}(\mathbb{P}_{\text{up}}, \widehat{\mathbb{P}}_{\text{up}}) < \varepsilon. \quad (1.4.5)$$

In Butler *et al.* (2018a), it is shown that $d_{\text{TV}}(\widehat{\mathbb{P}}_{\text{up}}, \mathbb{P}_{\text{up}}) = d_{\text{TV}}(\widehat{\mathbb{P}}_{\text{ob}}, \mathbb{P}_{\text{ob}})$, which immediately proves the following:

Theorem 1.4.2. \mathbb{P}_{up} is stable with respect to perturbations to \mathbb{P}_{ob} .

This next definition and result are useful in analyzing the sensitivity of the updated density with respect to the initial beliefs.

Definition 10 (Stability of Updated Densities II). Given \mathbb{P}_{in} and \mathbb{P}_{ob} , let $\widehat{\mathbb{P}}_{\text{in}}$ be any perturbation to \mathbb{P}_{in} on $(\Lambda, \mathcal{B}_{\Lambda})$ satisfying (1.4.1). Let \mathbb{P}_{up} and $\widehat{\mathbb{P}}_{\text{up}}$ denote the consistent solutions associated with \mathbb{P}_{ob} and $\widehat{\mathbb{P}}_{\text{ob}}$, respectively. Let $\{\mathbb{P}_{\Lambda, d}\}_{d \in \mathcal{D}}$ and $\{\widehat{\mathbb{P}}_{\Lambda, d}\}_{d \in \mathcal{D}}$ be the conditional probabilities defined by the disintegration of \mathbb{P}_{in} and $\widehat{\mathbb{P}}_{\text{in}}$, respectively. We say that \mathbb{P}_{up} is *stable* with respect to perturbations in \mathbb{P}_{in} if for all $\varepsilon > 0$, there exists a $\delta > 0$ such that for almost every $d \in \text{supp}(\mathbb{P}_{\text{ob}})$,

$$d_{\text{TV}}(\mathbb{P}_{\Lambda, d}, \widehat{\mathbb{P}}_{\Lambda, d}) < \delta \implies d_{\text{TV}}(\mathbb{P}_{\text{up}}, \widehat{\mathbb{P}}_{\text{up}}) < \varepsilon. \quad (1.4.6)$$

The following important stability theorem is also proven in Butler *et al.* (2018a):

Theorem 1.4.3. \mathbb{P}_{up} is stable with respect to perturbations to \mathbb{P}_{in}

Taken together, these stability results provide assurance that the updated density we obtain is accurate up to the level of experimental error polluting \mathbb{P}_{ob} and error in incorrectly specifying initial assumptions using \mathbb{P}_{in} . Given that specifying the definition of a “true” initial density is somewhat nebulous, we are less interested in the consequences of the latter conclusion. However, generating samples from \mathbb{P}_{up} generally requires a numerical approximation to the predicted distribution, which introduces additional errors in \mathbb{P}_{up} . In Section 1.4.2, the TV metric is used to bound the error in the updated density in terms of the error in the approximation to the push-forward of the initial.

1.4.2 Numerical Approximation and Sampling

If $\widehat{\pi}_{\text{pr}}$ denotes a computational approximation to the push-forward of the initial density obtained with $\widehat{\pi}_{\text{pr}}$ substituted for π_{pr} in (1.4.2), then the conditional densities from the Disintegration Theorem (c.f. Chapter III for more details), are given as

$$\frac{\widehat{d\mathbb{P}_{\Lambda,d}}}{d\mu_{\Lambda,d}(\lambda)} = \frac{\pi_{\text{in}}(\lambda)}{\widehat{\pi_{\text{pr}}(Q(\lambda))}},$$

where $\widehat{\mathbb{P}_{\Lambda,d}}$ denotes the disintegration of $\widehat{\mathbb{P}_{\text{up}}}$.

We assume the following for the approximation of the push-forward of the initial density:

Assumption 1.4.3. There exists some $C > 0$ such that

$$\pi_{\text{ob}}(d) \leq C\widehat{\pi_{\text{pr}}(d)} \text{ for a.e. } d \in \mathcal{D}.$$

If this assumption is satisfied, then from Butler *et al.* (2018a), we have the following:

Theorem 1.4.4. *The error in the approximate updated density is bounded above:*

$$d_{TV}(\mathbb{P}_{\text{up}}, \widehat{\mathbb{P}_{\text{up}}}) \leq Cd_{TV}(\mathbb{P}_{\text{pr}}, \widehat{\mathbb{P}_{\text{pr}}}), \quad (1.4.7)$$

where the C is the constant taken from Assumption 1.4.3.

A straightforward approach to construct $\widehat{\pi}_{\text{pr}}$ is to use a forward propagation of samples from Λ to \mathcal{D} and then apply kernel density estimation (KDE) (Butler *et al.*, 2018a). Then, we may evaluate π_{up} directly for any sample of Λ at the cost of one model solve per sample. While this allows us to incorporate sophisticated sampling techniques such as Markov-Chain Monte Carlo (MCMC) (Smith, 2013; Tarantola, 2005) to generate samples according to the updated distribution, we often opt for a simpler route based on rejection sampling by re-using the initial set of propagated samples. This avoids any additional model evaluations (as would be required by techniques relying on proposal samples such as MCMC). We leverage the re-use of samples in the results herein extensively.

By Theorem 1.4.4, the accuracy of the computed updated density relies on the accuracy of the approximation of the push-forward of the initial. Throughout this thesis, we utilize a KDE with a Gaussian kernel to produce the non-parametric estimates of π_{pr} . Such KDEs are known to converge at a rate of $\mathcal{O}(N^{-4/(4+D)})$ in mean-squared error and $\mathcal{O}(N^{-2/(4+D)})$ in L^1 -error, where D is the dimension of \mathcal{D} , and N is the number of samples from π_{in} propagated through Q (Silverman, 1986).

For simplicity, we introduce the following notation to capture the role of the ratio involved in (1.4.2) to demonstrate properties we can leverage for generating samples from π_{up} . We let

$$\pi_{\text{up}}(\lambda) = \pi_{\text{in}}(\lambda) r(Q(\lambda)), \text{ where } r(Q(\lambda)) = \frac{\pi_{\text{ob}}(Q(\lambda))}{\pi_{\text{pr}}(Q(\lambda))}.$$

Many standard calculations about the updated density involve integrals of functions of $r(Q(\lambda))$ with respect to the prior. For any measurable function f , we establish the connection of calculating quantities over Λ with those over \mathcal{D} by leveraging the following identity:

$$\int_{\Lambda} f(r(Q(\lambda))) d\mathbb{P}_{\text{in}} = \int_{\mathcal{D}} f(r(q)) d\mathbb{P}_{\text{pr}}$$

We use several throughout this thesis, including the integral of the updated density:

$$I(\pi_{\text{up}}) = \int_{\Lambda} r(Q(\lambda)) d\mathbb{P}_{\text{in}} = \int_{\mathcal{D}} r(q) d\mathbb{P}_{\text{pr}},$$

which we can use to validate that $I(\pi_{\text{up}}) = 1$ in order to numerically validate that the predictability assumption given in (1.4.7) was not violated. The sample average of $r(q)$ can be used to estimate $I(\pi_{\text{up}})$. This convenience is afforded by the fact that the i.i.d. samples provide us with the ability to take a Monte Carlo estimate of the integral.

Taken together, the results summarized in this section demonstrate that the Data-Consistent framework and density-based solution (1.4.2) have been rigorously constructed and studied. They give an experimenter assurance that there are not unexpected consequences for small mistakes in problem formulation. In the following section, we provide a similar sense of assurance for a central practical consideration involved in this work: that the results depend on computational implementations of the aforementioned theory, i.e., software. We directly address how to establish a complementary level of rigor to the implementation of the work as was invested in the construction of the theory. We leverage modern advances in software engineering with an emphasis on results being reproducible in an accessible manner.

1.5 Towards a Reproducible Thesis

In some respects, the practice of writing software has diverged from the motivations of an academic researcher. The latter seeks to generate new knowledge and may write a set of example scripts/programs to demonstrate some novel idea or method. By contrast, the motivations of a software engineer are related to resiliency. Not only must they ensure the code works as expected given a myriad of ways users may interact with it, but it is necessary to write the code in a manner compatible with maintaining it into

the future. Much of the work of writing “good software” is concerned with writing appropriate documentation to express the intended usage and logic underlying architectural decisions. Without proper context and an understandable architecture, new ideas that are implemented in programs are unlikely to be adopted. There are many ways to write a functioning program to demonstrate a proof-of-concept, but creating something that is *user-friendly*, and scales to different computational environments/resources, requires an entirely different approach.

Decisions made early in the software design cycle have lasting impacts on future features and functionality. Rigor is added to libraries through the writing of *unit tests*, and eventually *functional tests*, which validate individual components and entire workflows, respectively. The practice of *continuous integration* ensures that the download and installation process is predictable and reproducible by running the requisite steps (and tests) in an ephemeral environment as an independent verification that programs execute as expected. Code that only runs on the one’s computer is impractical, since any thorough review of the results requires validation by an independent third party. Having continuous integration (and deployment for packaging the software), tests, and documentation, allows a repository of code to be functionally and practically accessible to the larger research community.

This thesis is concerned not only with a demonstration of novel mathematical content—showcasing new ways to make inferences from noisy data in a novel Data-Consistent framework—it also serves to set a precedent for guaranteeing that the results presented are **fully reproducible**. In mathematics, reproducibility is ensured through the use of proofs, which motivate the original work presented here. However, as the title of this thesis suggests, much of the work involves computational implementation of the novel research into Data Consistent Inversion, studying the impact of using computers to perform the task of making conclusions based on data. Mathematics is implemented on computers through software. We are therefore concerned with verifying and validating the expected functionality of that software, which aligns with our training as mathematicians; we care deeply about making sure things are rigorous.

In short, we want to make sure that theory aligns with practice, and that both live up to high standards of intellectual scrutiny. Every computational result, illustrative figure, table, plot, etc. presented in this thesis is associated with the scripts that generate them, and are included in the publicly-available GitHub repository. With a minimal set of instructions, everything (including this document itself), can be reproduced. The specific tools and frameworks through which the reproduction of these results can be accomplished change over time. The GitHub repository (Pilosov, 2020) for this dissertation provides a num-

ber of pathways for generating the results, including ones that do not require any installation of software on local or remote resources.

1.6 Outline of Remaining Chapters

In Chapter II, we propose a way by which parameter identification can be performed in the DCI framework by posing the problem as a SIP and maximizing π_{up} . Central to how this contribution is accomplished in practice is the definition of a data-constructed QoI map. The impact of a QoI's inherent geometric properties on our ability to approximate solutions to SIPs using finite sampling is then summarized in Chapter III. The focus there is on the property called skewness, which is connected to the QoI maps introduced in II through a case study of a PDE-based example in Chapter IV. Finally, we provide some concluding remarks and directions for future research in Chapter V alongside several examples demonstrating preliminary results for novel extensions of the work presented in this thesis.

CHAPTER II

DATA-DRIVEN MAPS AND CONSISTENT INVERSION FOR PARAMETER ESTIMATION

In this chapter, we extend the data-consistent framework to solve problems involving epistemic uncertainties in model parameters. This requires constructing QoI maps in an *a posteriori* fashion using noisy data, which is a novel way to define QoI maps in the data-consistent framework. The theory of existence, uniqueness, and convergence of maximal updated density (MUD) points are also provided for linear data-constructed QoI maps using typical assumptions found in the Bayesian literature. Comparisons to other parameter estimates such as those obtained using a least-squares or Bayesian approach are also provided. The applicability of the approach to nonlinear data-constructed QoI maps is also numerically demonstrated for ordinary and partial differential equation models of dynamical and stationary systems.

While there are several on-going and future research directions that are outside the scope of this thesis, we do not wish to hide certain technical challenges in implementing this approach in certain scenarios. We therefore address several technical challenges where appropriate to both point out these challenges as well as the heuristics we currently employ to handle these challenges.

The rest of this chapter is outlined as follows. We first compare the estimators induced by the solutions to the DIP and SIP by taking the point of maximal density of the respective distributions in Section 2.1. There, we present closed-form derivations for the novel estimator presented in this work: the MUD point. In Section 2.2, we present an example involving high-dimensional linear maps, connecting rank and dimension to the accuracy and convergence of the estimators. Following the example, we show in 2.3 how a QoI map can be constructed from an arbitrary collection of noisy data. We leverage the theory of the MUD point from the earlier section to provide a general framework for reducing epistemic uncertainty in a point-estimate as more data are collected. Finally, in Section 2.4, we demonstrate that the presented QoI map can be used to form accurate point estimates by solving the SIP even on nonlinear maps and initial densities which violate the assumptions of the theoretical construction.

2.1 Comparing the Maximal Updated Density (MUD) and MAP points

We formally define the maximal updated density (MUD) point as

$$\lambda^{\text{MUD}} := \arg \max \pi_{\text{up}}(\lambda). \quad (2.1.1)$$

We motivate the use of the MUD point as an alternative to the MAP point for parameter estimation problems. In this section, we assume linear (or affine) QoI maps with Gaussian distributions, which are often used in the UQ literature to provide a common framework for comparing methods and their solutions.

This section is structured into several subsections to help focus the interpretations and results.

In Section 2.1.1, we present some useful details, notation, and terminology used for this comparison framework. To build intuition, we compare both the MUD and MAP points in Section 2.1.2 using a low-dimensional example. A unifying perspective is provided for affine maps in Section 2.1.3 along with derivations of closed form expressions for the MUD and MAP points in this comparison framework. These results are summarized in a theorem of existence and uniqueness of the MUD point in this comparison framework.

2.1.1 MUD and MAP points for the “linear Gaussian” case

Let $\|\mathbf{x}\|_C^2 := (\mathbf{x}, \mathbf{x})_C = \mathbf{x}^T C \mathbf{x}$ denote the square of the induced norm associated with a positive-definite operator $C : \mathbb{R}^n \rightarrow \mathbb{R}^n$ and the usual (Euclidean) inner product. In what follows, the inverse covariances associated with non-degenerative multivariate Gaussian distributions will play the role of C .

Suppose that the initial and prior densities are both given by the same $\mathcal{N}(\lambda_0, \Sigma_{\text{init}})$ distribution. Additionally, suppose the map Q is linear and that the data-likelihood and observed densities are both given by the same $\mathcal{N}(\mathbf{y}, \Sigma_{\text{obs}})$ distribution.

The linearity of Q implies that $Q(\lambda) = A\lambda$ for some $A \in \mathbb{R}^{d \times p}$, and that the predicted density follows a $\mathcal{N}(Q(\lambda_0), \Sigma_{\text{pred}})$ distribution where

$$\Sigma_{\text{pred}} := A\Sigma_{\text{init}}A^\top. \quad (2.1.2)$$

While it is not technically necessary to ensure that the predictability assumption holds (i.e., that π_{up} is in fact a density) in order to formally define a MUD point using (2.1.1), it is useful when discussing certain theoretical results involving data-constructed QoI maps as we see in Sections 2.1.3 and 2.3. Conceptually, the predictability assumption holds when the predicted variance is larger in all directions than the observed variance. This condition is consistent with the desired outcome of a parameter estimation problem where the incorporation of observed data produces not only an improvement to the initial point estimate but also serves to reduce the uncertainty in this point estimate (quantified in this case by the covariance). Mathematically, this occurs when the smallest eigenvalue value of Σ_{pred} is larger than the largest eigenvalue value of Σ_{obs} .

Table 2.1: Functionals to minimize to obtain λ that maximizes the updated PDF (bottom) and the Bayesian posterior PDF (top). Here, $T(\lambda)$ is the typical functional often associated with Tikhonov regularization, and the $J(\lambda)$ has an additional term subtracted from $T(\lambda)$ coming from the predicted density that serves as “unregularization” in data-informed directions.

Tikhonov	$T(\lambda) := \ Q(\lambda) - \mathbf{y}\ _{\Sigma_{\text{obs}}^{-1}}^2 + \ \lambda - \lambda_0\ _{\Sigma_{\text{init}}^{-1}}^2$
Data-Consistent	$J(\lambda) := T(\lambda) - \ Q(\lambda) - Q(\lambda_0)\ _{\Sigma_{\text{pred}}^{-1}}^2$

When Σ_{obs} is non-degenerative (i.e., the smallest eigenvalue is positive), the predictability assumption can always be satisfied if $d \leq p$ and A is full rank by choosing Σ_{init} to have sufficiently large eigenvalues (i.e., if we choose initial variances to be sufficiently large). To simplify the theoretical presentation of this section, we assume these conditions are met so that the predictability assumption holds and π_{up} does in fact define a density. However, in Section 2.2, we still compute the formal MUD point for a high-dimensional example involving rank-deficient A to demonstrate the overall usefulness of the MUD point even in situations where π_{up} may fail to be an actual density.

With these assumptions, the parameters that maximize the posterior and updated densities are described as the arguments that minimize certain quadratic functionals. Table 2.1 presents a scaling of these functionals defined by the negative logarithm of the associated posterior and updated densities. Note that the functional, $T(\lambda)$, obtained from the posterior density is immediately identified as the typical functional used in Tikhonov regularization (Tarantola, 2005).

The data-mismatch term given by

$$\|Q(\lambda) - \mathbf{y}\|_{\Sigma_{\text{obs}}^{-1}}^2$$

comes from the data-likelihood/observed density whereas the regularization term defined by

$$\|\lambda - \lambda_0\|_{\Sigma_{\text{init}}^{-1}}^2$$

comes from the prior/initial density. We refer to this term as the Tikhonov regularization term.

The functional, $J(\lambda)$, obtained from the updated density is written as a modification of the $T(\lambda)$ function where the subtraction of

$$\|Q(\lambda) - Q(\lambda_0)\|_{\Sigma_{\text{pred}}^{-1}}^2$$

comes from the predicted density.

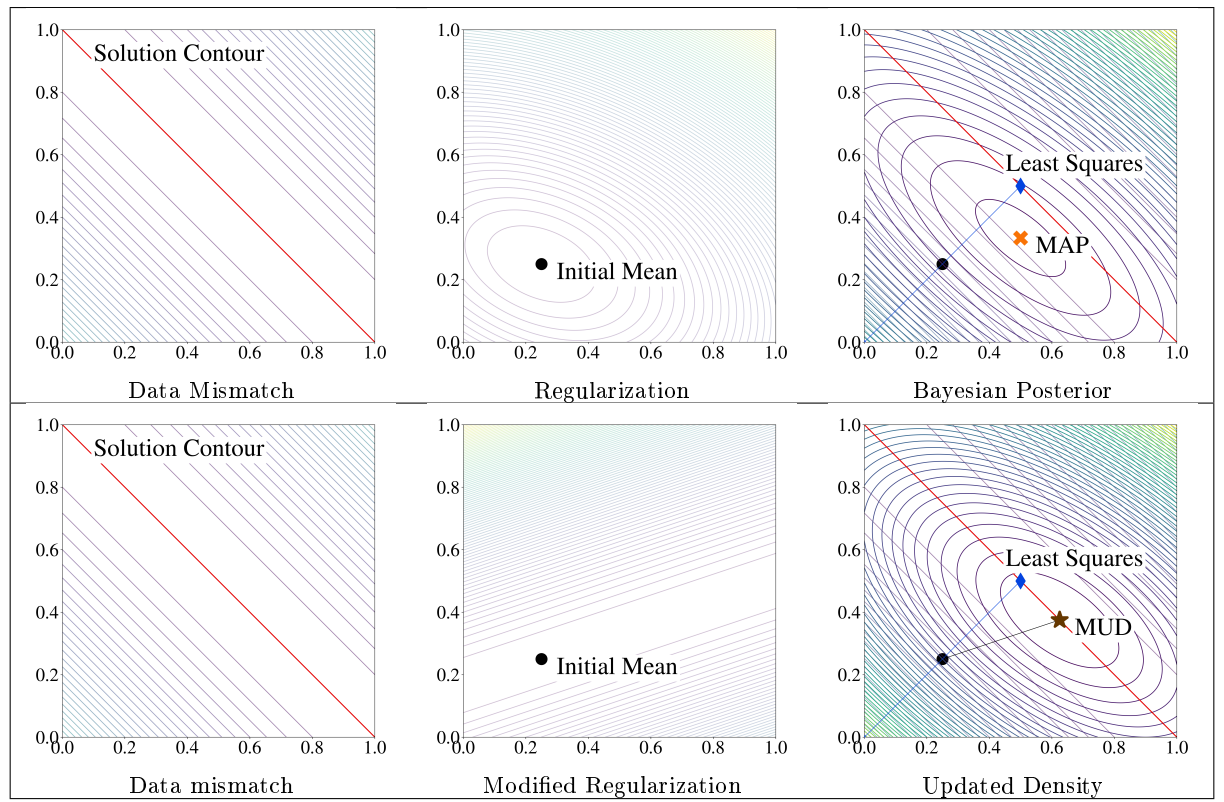


Figure 2.1: Gaussian data mismatch over 2-D parameter space for a 2-to-1 linear map (left plots). Gaussian initial/prior lead to different regularization terms associated with updated/Bayesian PDFs (middle plots), which lead to different optimization functions (right plots) and parameter estimates that produce maximum PDF values for update/Bayesian PDF (red dot in right plots).

2.1.2 A Low-Dimensional Example

To build intuition around the fundamental differences of MAP and MUD points, we consider an example where the linear QoI map is defined by $A = [1 \ 1]$, i.e., the parameter space is 2-dimensional while the data space is 1-dimensional.

In this example, the parameters in the initial and observed densities are given by

$$\lambda_0 = [0.25 \ 0.25]^\top, \Sigma_{\text{init}} = \begin{bmatrix} 1 & -0.25 \\ -0.25 & 0.5 \end{bmatrix}, \mathbf{y} = 1, \text{ and } \Sigma_{\text{obs}} = [0.25].$$

The top row of Fig. 2.1 shows contour plots in the parameter space for the data-mismatch term (left), Tikhonov regularization term (middle), as well as the functional $T(\lambda)$ (right). Conceptually, the regularization term is a radially symmetric function that penalizes parameters that are far away from the initial mean.

The bottom row of Fig. 2.1 shows contour plots in the parameter space for the data-mismatch term (left), modified regularization term (middle), as well as the functional $J(\lambda)$ (right). Here, we see that

the modified regularization term only penalizes the movement of parameters in certain directions away from the initial parameter mean.

2.1.3 A Unifying Perspective and Closed Form Solutions

Assume that the QoI map, Q , now takes the slightly more general form

$$Q(\lambda) = A\lambda + \mathbf{b} \quad (2.1.3)$$

where $\mathbf{b} \in \mathbb{R}^d$ may be viewed as a bias in the QoI map. The inclusion of this term makes it relevant for drawing conclusions involving the data-constructed QoI maps presented in Section 2.3. Using the same Gaussian distribution assumptions as described in Section 2.1.1, we again identify the MAP and MUD points as the values that minimize the functionals $T(\lambda)$ and $J(\lambda)$, respectively, shown in Table 2.1.

The posterior covariance is formally given by

$$\Sigma_{\text{post}} := (A^\top \Sigma_{\text{obs}}^{-1} A + \Sigma_{\text{init}}^{-1})^{-1}. \quad (2.1.4)$$

Applying the Woodbury matrix identity and (2.1.2), we rewrite the posterior covariance as

$$\Sigma_{\text{post}} = \Sigma_{\text{init}} - \Sigma_{\text{init}} A^\top [\Sigma_{\text{pred}} + \Sigma_{\text{obs}}]^{-1} A \Sigma_{\text{init}}, \quad (2.1.5)$$

which allows us to interpret Σ_{post} as a rank d correction (or update) of Σ_{init} . Note that $\Sigma_{\text{pred}} + \Sigma_{\text{obs}}$ is invertible because it is the sum of two symmetric positive definite matrices. With either version of Σ_{post} given above, we rewrite the closed form expression for the MAP point given in Tarantola (2005) as

$$\lambda^{\text{MAP}} = \lambda_0 + \Sigma_{\text{post}} A^\top \Sigma_{\text{obs}}^{-1} (\mathbf{y} - b - A\lambda_0). \quad (2.1.6)$$

We now derive an alternative representation of $J(\lambda)$ to draw comparisons to the posterior covariance and MAP point. First, define

$$R := \Sigma_{\text{init}}^{-1} - A^\top \Sigma_{\text{pred}}^{-1} A. \quad (2.1.7)$$

Using this R , rewrite $J(\lambda)$ as

$$J(\lambda) := \|\mathbf{y} - Q(\lambda)\|_{\Sigma_{\text{obs}}^{-1}}^2 + \|\lambda - \lambda_0\|_R^2. \quad (2.1.8)$$

In this form, we identify R as the *effective regularization* in $J(\lambda)$ due to the formulation in the data-consistent framework.

Observe that if $d = p$, then, by the assumption that A is full-rank, A is invertible. In this case, R is the $p \times p$ zero matrix and (2.1.8) reduces to the data-discrepancy term so that the MUD point is recognizable as the least squares solution, i.e., the point that minimizes the data-discrepancy term. Moreover, in this case we can immediately identify that $\lambda^{\text{MUD}} = A^{-1}(\mathbf{y} - b)$. This is also evident from the perspective of the densities. Specifically, in this case, π_{up} is defined by applying a change of variables formula to π_{ob} .

Suppose instead that $d < p$ so that the inverse-problem is under-determined. In this case, we observe that constructing R only requires specification of the initial/prior density and the QoI map, i.e., R may be defined prior to any collection of data on the QoI. Subsequently, we can interpret $J(\lambda)$ as coming from a modified Bayesian inverse problem with a prior defined by a $N(\lambda_0, \Sigma_R)$ distribution where $\Sigma_R = R^{-1}$. In other words, the MUD and MAP points can both be interpreted as solutions to different Bayesian inverse problems.

However, Σ_R is in fact a degenerative covariance, i.e., R is not technically invertible. This implies that Σ_R cannot be directly substituted in for Σ_{init} in (2.1.5) to define a closed form expression for Σ_{up} . We therefore first substitute Σ_{post} and $\Sigma_{\text{init}}^{-1}$ in (2.1.5) with Σ_{up} and R , respectively, to get

$$\Sigma_{\text{up}} := (A^\top \Sigma_{\text{obs}}^{-1} A + R)^{-1}. \quad (2.1.9)$$

Since R is not invertible, Woodbury's identity cannot be applied (yet). Using (2.1.7), we can form

$$\Sigma_{\text{up}} = (A^\top \Sigma_{\text{obs}}^{-1} A + \Sigma_{\text{init}}^{-1} - A^\top \Sigma_{\text{pred}}^{-1} A)^{-1}, \quad (2.1.10)$$

which is re-arranged as

$$\Sigma_{\text{up}} = (A^\top [\Sigma_{\text{obs}}^{-1} - \Sigma_{\text{pred}}^{-1}] A + \Sigma_{\text{init}}^{-1})^{-1}. \quad (2.1.11)$$

Recall from Section 2.1.1 that the predictability assumption in this case is that the smallest eigenvalue of Σ_{pred} is larger than the largest eigenvalue of Σ_{obs} . The roles are reversed when we consider the inverses of these matrices. Subsequently, $\Sigma_{\text{obs}}^{-1} - \Sigma_{\text{pred}}^{-1}$ is a symmetric positive definite matrix and thus invertible. Applying the Woodbury identity yields

$$\Sigma_{\text{up}} = \Sigma_{\text{init}} - \Sigma_{\text{init}} A^\top \left([\Sigma_{\text{obs}}^{-1} - \Sigma_{\text{pred}}^{-1}]^{-1} + \Sigma_{\text{pred}} \right)^{-1} A \Sigma_{\text{init}}. \quad (2.1.12)$$

Applying Hua's identity and simplifying gives

$$\left([\Sigma_{\text{obs}}^{-1} - \Sigma_{\text{pred}}^{-1}]^{-1} + \Sigma_{\text{pred}} \right)^{-1} = \Sigma_{\text{pred}}^{-1} [\Sigma_{\text{pred}} - \Sigma_{\text{obs}}] \Sigma_{\text{pred}}^{-1}. \quad (2.1.13)$$

Substituting (2.1.13) into (2.1.12) gives

$$\Sigma_{\text{up}} = \Sigma_{\text{init}} - \Sigma_{\text{init}} A^\top \Sigma_{\text{pred}}^{-1} [\Sigma_{\text{pred}} - \Sigma_{\text{obs}}] \Sigma_{\text{pred}}^{-1} A \Sigma_{\text{init}}. \quad (2.1.14)$$

We can now modify the expression for the MAP point given in (2.1.6) by substituting Σ_{up} for Σ_{post} to write the MUD point that minimizes J as

$$\lambda^{\text{MUD}} = \lambda_0 + \Sigma_{\text{up}} A^\top \Sigma_{\text{obs}}^{-1} (\mathbf{y} - b - A\lambda_0). \quad (2.1.15)$$

Substituting (2.1.14) into (2.1.15) and simplifying, we have

$$\lambda^{\text{MUD}} = \lambda_0 + \Sigma_{\text{init}} A^\top \Sigma_{\text{pred}}^{-1} (\mathbf{y} - b - A\lambda_0). \quad (2.1.16)$$

Comparing (2.1.16) to (2.1.6), we see that the MUD point does not depend on the observed covariance whereas the MAP point does. Moreover, applying Q to (2.1.16) and substituting accordingly reveals that $Q(\lambda^{\text{MUD}}) = \mathbf{y}$.

Overall, this motivates the MUD point as an *alternative parameter estimate* with predictive accuracy and properties directly correlated to the relationship between \mathbf{y} and the true signal for which noisy data are generated.

These ideas are explored further in Section 2.2 and utilized in the analysis of QoI maps constructed from noisy measurement data associated with a true parameter value in Section 2.3. We end this section by summarizing the above results in the following theorem stating the existence and uniqueness of a MUD point for the linear Gaussian case.

Theorem 2.1.1. *Suppose $Q(\lambda) = A\lambda + b$ for some full rank $A \in \mathbb{R}^{d \times p}$ with $d \leq p$ and $b \in \mathbb{R}^d$. If $\pi_{\text{in}} \sim N(\lambda_0, \Sigma_{\text{init}})$, $\pi_{\text{ob}} \sim N(\mathbf{y}, \Sigma_{\text{obs}})$, and the predictability assumption holds, then*

- (a) *There exists a unique parameter, denoted by λ^{MUD} , that maximizes π_{up} .*
- (b) *$Q(\lambda^{\text{MUD}}) = \mathbf{y}$.*
- (c) *If $d = p$, λ^{MUD} is given by A^{-1} . If $d < p$, λ^{MUD} is given by (2.1.16) and the covariance associated with this point is given by (2.1.14).*

2.2 Higher-Dimensional Linear Gaussian Examples

We first describe the relationship of MUD, MAP, and least squares estimates to the set-valued inverses of Q in order to establish a conceptual framework for interpreting the numerical results that follow. While this discussion is somewhat abstract, we refer to Figure 2.1 to make these ideas more clear.

The MUD point exists on the generalized contour defined by $Q^{-1}(\mathbf{y})$. We say generalized contour in this case because if A is a p -to- d full rank linear map with $d < p$, then $Q^{-1}(\mathbf{y})$ exists as a $(p - d)$ -dimensional linear hyperplane in Λ .

This means that the MUD point retains the “predictive precision” of a least squares solution to the inverse problem (i.e., a parameter that minimizes the data-mismatch term $\|\mathbf{y} - Q(\lambda)\|_{\Sigma_{\text{obs}}^{-1}}$) while incorporating the flexibility of prior beliefs in directions not informed by the QoI. This is illustrated in the bottom right plot of Figure 2.1. For under-determined or ill-conditioned problems, this suggests that “good” prior beliefs may be used to produce a MUD point that is more accurate than a least squares solution. This is explored in the following examples involving high-dimensional linear maps.

By contrast, the MAP point exists on a line connecting the initial mean, λ_0 , and the generalized contour defined by $Q^{-1}(\mathbf{y})$. Substituting (2.1.5) into (2.1.6), we see that this line is in the direction of the orthogonal nullspace of the image of A under Σ_{init} ; i.e., $\mathcal{N}(\Sigma_{\text{init}} A)^\perp$. In fact, this line intersects the generalized contour defined by $Q^{-1}(\mathbf{y})$ precisely at the MUD point. If one parameterizes the line between λ_0 and λ^{MUD} , then one can also identify λ^{MAP} as a convex sum of these two points. The weights of this convex sum, which determine the position of the MAP point on this line, are determined by the “precision of data” (i.e., on Σ_{obs}) and the “strength of prior beliefs” (i.e., on Σ_{init}). This is seen by comparing the location of the MAP point in the top right plot of Figure 2.1 to the line segment connecting the initial mean to the MUD point in the bottom right plot of this same figure. The impact of this is also explored in the following examples.

2.2.1 Impact of Output Dimension

We consider QoI defined by $A\lambda + \mathbf{b}$ for $A \in \mathbb{R}^{k \times 100}$ where $k = 1, 2, \dots, 100$ to demonstrate how the various estimates of a true parameter λ^\dagger are impacted by the number of available QoI. To generate the matrices, we first generate 10,000 independent identically distributed (i.i.d.) random numbers from a $N(0, 1)$ distribution that are arranged into a reference $\mathbb{R}^{100 \times 100}$ matrix.

The same distribution is also used for generating the components of the 100-dimensional vectors defining a reference bias vector \mathbf{b} and reference parameter λ^\dagger . A multivariate Gaussian distribution is used for the initial density, with zero mean and Σ_{init} chosen as a diagonal covariance with random entries drawn from $U[0.5, 1.5]$ and sorted in descending order. The prior density is also a zero mean multivariate

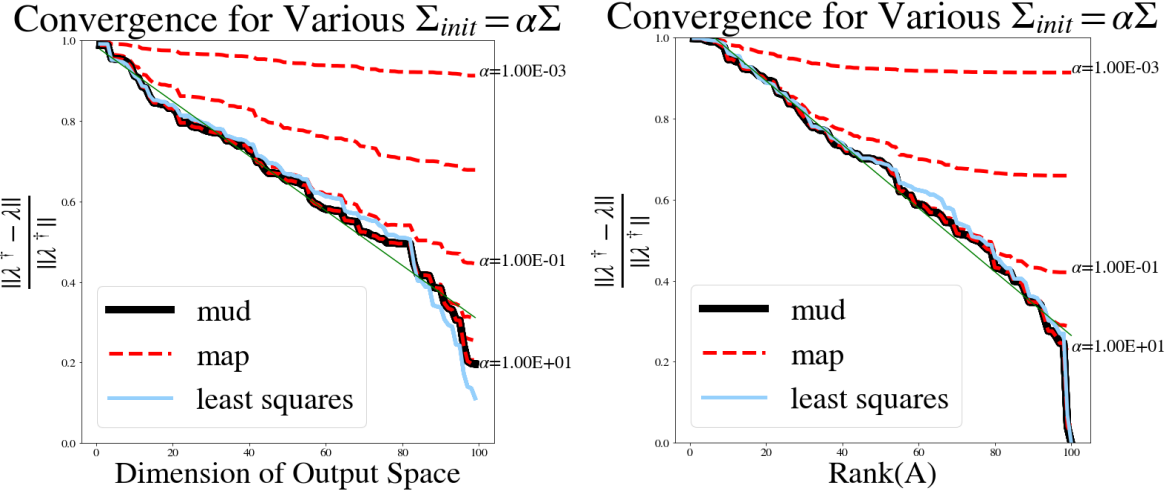


Figure 2.2: Relative errors between λ^\dagger and (i) the least squares solution obtained through numpy’s `linalg.pinv` module, (ii) the closed-form solution for the MUD point given in Eq (2.1.16), and (iii) the MAP point. (Left): Error for increasing dimensions of D for A taken to be a Gaussian Random Map. (Right): Error for increasing row-rank of A , generated with Gaussian vectors and a SVD.

Gaussian distribution. However, to demonstrate the impact of the strength of prior beliefs on the MAP point, we choose the prior covariance to be $\alpha \Sigma_{\text{init}}$ for $\alpha = 0.001, 0.01, 0.1$, and 10 . Here, smaller values of α correspond to a “stronger” belief in the prior since the prior density becomes more concentrated near the prior mean.

To study the impact of dimension on the MUD, MAP, and least squares estimates, we solve a sequence of inverse problems by truncating the rows of the reference matrix and bias vector. The results are summarized in the left plot of Figure 2.2, which shows convergence towards λ^\dagger for all the problems considered with the exception of several MAP estimates corresponding to strongly-held beliefs in the prior.

We note that the MUD solution is the same for all choices of α and corresponds to the same level of accuracy that the MAP point achieves when α is chosen to be large. In other words, the MUD point is not impacted by a scaling of the initial covariance, providing *consistent* solutions which demonstrate levels of accuracy that MAP points only exhibit for larger values of scaling factors.

Of interest is also that the MUD point can sometimes out-perform the least squares estimate while generally achieving similar levels of accuracy. This suggests that the MUD point has several favorable qualities. Not only is it robust to the specification of prior assumptions, but it manages to offer the flexibility of incorporating good prior specifications without paying the additional cost of hyper-parameter optimization (i.e., choosing an appropriate α) that would be required for the MAP estimates to achieve comparable results.

While omitted in the interest of space, if Σ_{init} is chosen as αI , where I denotes the identity matrix of appropriate dimensions, then the MUD point will always agree with the least squares estimate. Taking these results together, this implies that only a good “relative spatial structure” of prior beliefs is required to improve the MUD point’s accuracy over both MAP and least squares estimates.

2.2.2 Impact of Rank: One Hundred (Deficient) $\mathbb{R}^{100 \times 100}$ matrices

Here, we investigate whether the previous dimension-dependent example extend to matrices A which are of a fixed dimension but varying rank. This is of interest in applications where many QoI are available to construct an operator but a great deal of redundancy may be present in the data collected, and feature-engineering new quantities is somehow prohibitive (perhaps due to gradient estimation).

The rank of A corresponds to the number of unique directions of information present in the operator, i.e., how many directions in the parameter space are informed by the QoI map. The operators in the previous example were all full rank, so the dimension of each map also corresponded to the rank of A . When A is rank-deficient, Σ_{pred} is non-invertible, so we must modify the form of (2.1.16) to substitute a pseudo-inverse for the predicted covariance.

In this example, the dimension of the data space remains fixed at $d = 100$ across all experiments. However, we sequentially increase the row-rank of A from $r = 1, \dots, 100$. To control the rank of A , we first construct a reference $\mathbb{R}^{100 \times 100}$ matrix as in the previous example using 10,000 i.i.d. $N(0, 1)$ random numbers. We then compute a singular value decomposition of this reference matrix of the form USV^\top and construct 100 rank-1 matrices of the form $A_i = \mathbf{u}_i s_i \mathbf{v}_i^\top$ for $i = 1, \dots, 100$ where \mathbf{u}_i and \mathbf{v}_i denote the i th columns of U and V , respectively and s_i denotes the i th singular value. Then, we analyze the impact of $A = \sum_i^r A_i$ for $r = 1, \dots, 100$. Aside from the differing construction of A , the rest of the choices involved in the experiment (λ^\dagger , the reference bias vector, and the distributions involved) is identical to the previous example.

In the right plot of Figure 2.2, we again find that the MUD point is generally as accurate as the least squares estimate, but incorporates an initial description of uncertainty, which may allow it to outperform the least squares estimate. Also, we again see that the MAP estimates are impacted by the strength of prior beliefs.

2.3 Data-constructed QoI maps and MUD points

Suppose there exists d measurement devices for which repeated noisy data are obtained. For each $1 \leq j \leq d$, denote by $\mathcal{M}_j(\lambda^\dagger)$ the j th measurement device, and denote by N_j the number of noisy data obtained for $\mathcal{M}_j(\lambda^\dagger)$. Let $d_{j,i}$ denote the i th noisy datum obtained for the j th measurement where $1 \leq i \leq N_j$. To simplify the presentation and some of the resulting notation, we assume an unbiased additive error

model for the measurement noise with independent identically distributed (i.i.d.) Gaussian errors so that

$$d_{j,i} = M_j(\lambda^*) + \xi_i, \quad \xi_i \sim N(0, \sigma_j^2), \quad 1 \leq i \leq N_j. \quad (2.3.1)$$

2.3.1 The Weighted Mean Error Map

We now construct a d -dimensional vector-valued map from data obtained on the d measurement devices. The data-defined QoI map we consider in this work is referred to as the weighted mean error (WME) map, denoted by $Q_{\text{WME}}(\lambda)$ with j th component, denoted by $Q_{\text{WME},j}(\lambda)$, given by

$$Q_{\text{WME},j}(\lambda) := \frac{1}{\sqrt{N_j}} \sum_{i=1}^{N_j} \frac{M_j(\lambda) - d_{j,i}}{\sigma_j}. \quad (2.3.2)$$

By a substitution of (2.3.1) into (2.3.2) and rationalizing the denominator of the multiplicative factor, $Q_{\text{WME},j}(\lambda^\dagger)$ is identified as the sample average of N_j random draws from an i.i.d. $N(0, N_j)$ distribution. By assumption, the observed data are generated according to the fixed true physical parameter vector given by λ^\dagger in (2.3.1). Subsequently, each component of $Q_{\text{WME}}(\lambda^\dagger)$ is a random draw from an $N(0, 1)$ distribution. Therefore, with this choice of data-defined QoI map, we specify π_{ob} as a $N(\mathbf{0}_{d \times 1}, \mathbf{I}_{d \times d})$ distribution.

2.3.2 Analysis of MUD point for the WME map

Below, we consider issues of existence, uniqueness, and convergence of λ^{MUD} for the WME map under certain assumptions. In 2.4.3, we provide some remarks on how we plan to generalize this analysis in future work.

For each $1 \leq j \leq d$, assume that the observable maps M_j are linear maps of λ (affine maps require minor modifications to the results below). For notational simplicity below, assume that M_j is written explicitly as a $1 \times p$ row vector and that the d -vectors form a linearly independent set. Then, it is possible to rewrite $Q_{\text{WME}}(\lambda)$ as

$$Q_{\text{WME}}(\lambda) = A(\mathbf{N})\lambda + b(\mathbf{N}), \quad (2.3.3)$$

where the j th component of $\mathbf{N} \in \mathbb{R}^d$ is given by N_j and the j th row of $A(\mathbf{N}) \in \mathbb{R}^{d \times p}$ is given by

$$\frac{1}{\sqrt{N_j}} \sum_{i=1}^{N_j} \frac{M_j}{\sigma_j} = \frac{\sqrt{N_j}}{\sigma_j} M_j, \quad (2.3.4)$$

and the bias vector, $\mathbf{b}(\mathbf{N}) \in \mathbb{R}^d$, is defined by the data, with j th component, denoted by \mathbf{b}_j , given by

$$\mathbf{b}_j(\mathbf{N}) = -\frac{1}{\sqrt{N_j}} \sum_{i=1}^{N_j} \frac{d_{j,i}}{\sigma_j}. \quad (2.3.5)$$

Since $A(\mathbf{N})\Sigma_{\text{init}}A(\mathbf{N})^\top$ defines a predicted covariance, and the observed covariance is the identity map, the predictability assumption is immediately satisfied if each diagonal component of the predicted covariance is significantly greater than 1.

The off-diagonal components of the predicted covariance (which are dictated in large part by the structure of the measurement operators M_j) dictate how much larger than 1 each diagonal component must be to ensure the predictability assumption holds. However, we demonstrate below that this will happen once a minimum number of data points N_{\min} are obtained for each measurement.

First, observe that the j th diagonal component of the predicted covariance matrix is given by the predicted variance associated with using the scalar-valued map $Q_{\text{WME},j}$. Then, the associated predicted variance is given by

$$\frac{N_j}{\sigma_j^2} M_j \Sigma_{\text{init}} M_j^\top \quad (2.3.6)$$

Since Σ_{init} is assumed to be non-degenerative and M_j is a non-trivial row vector, this predicted variance grows linearly with N_j . In other words, the j th diagonal component of the predicted covariance has the form $\beta_j N_j$ for some $\beta_j > 0$. Let $N_{\min,j}$ denote the minimum N_j for $1 \leq j \leq N$ necessary to make the j th diagonal components sufficiently large so that the smallest eigenvalue of the predicted covariance is larger than 1 (which is the repeated eigenvalue for the observed covariance).

The following result is now an immediate consequence of Theorem 2.1.1,

Corollary 2.3.1. If $\pi_{\text{in}} \sim N(\lambda_0, \Sigma_{\text{init}})$ and data are obtained for d linearly independent measurements on Λ with an additive noise model with i.i.d. Gaussian noise for each measurement, then there exists a minimum number of data points obtained for each of the measurements such that there exists a unique λ^{MUD} and $Q_{\text{WME}}(\lambda^{\text{MUD}}) = 0$.

2.4 MUD points for nonlinear maps: Examples

We now use MUD points as parameter estimates for nonlinear data-constructed maps using simulated noisy temporal and spatial data associated with solutions to differential equations. The previously derived closed form expressions for λ^{MUD} do not apply in these examples. Instead, in each example we use a fixed set of i.i.d. samples drawn from the initial density to approximate the updated density and subsequently choose the sample that maximizes this approximation. Future work will consider how to leverage

more sophisticated optimization approaches for estimating λ^{MUD} , e.g., through iterative quasi-Newton approaches based on repeated approximate linearizations that can exploit the closed form expressions for λ^{MUD} .

The two examples below have distinct points of emphasis. The first example focuses on the improved accuracy and precision of scalar λ^{MUD} estimates as more data are incorporated into the construction of Q_{WME} . The second example focuses on how the utilization of subsets of the data into different components of a vector-valued Q_{WME} can improve the estimates across multiple components of a λ^{MUD} estimate for a parameter vector. Despite these differences, both examples share the following details.

- Sets of i.i.d. samples from the initial densities are used to both approximate the predicted density (and thus the updated density) and to form a discrete space in which to search for the MUD point.
- A reference parameter is chosen and used to establish a (noiseless) reference solution (in space or time).
- An i.i.d. additive noise model with $\xi \sim N(0, \sigma^2)$ is used to perturb the reference temporal and spatial solutions.
- Since the magnitude of solutions in both examples is $\mathcal{O}(1)$, noise variances are chosen so that $\mathbb{P}(|\xi| < \tau) = 99\%$, with $\tau = 0.1$. In other words, we simulate an “engineering accuracy” by permitting measurement noise to vary by approximately 10% of the signal magnitude.

2.4.1 ODE Example

Consider the exponential decay problem with uncertain decay rate λ :

$$\begin{cases} \frac{\partial u}{\partial t} = \lambda u(t), & 0 < t \leq 3, \\ u(0) = 0.75, \end{cases}$$

with solution

$$u(t; \lambda) = u_0 \exp(-\lambda t), \quad u_0 = 0.75, \quad (2.4.1)$$

and measurements begin at $t = 1$.

The initial uncertainty in the decay rate is given by a uniform density on $\lambda \in \Lambda = (0, 1)$, and 10,000 samples from this density are used to estimate the push-forward and updated densities as well as the MUD points. Noisy data are simulated over the interval $t \in [1, 3]$ assuming a 100Hz measurement sensor. An example of this setup is shown in Figure 2.3, with the solid line representing the “true” signal

obtained by evaluating the solution for $\lambda^\dagger = 0.5$, and a particular realization of noisy data shown as perturbed points around it.

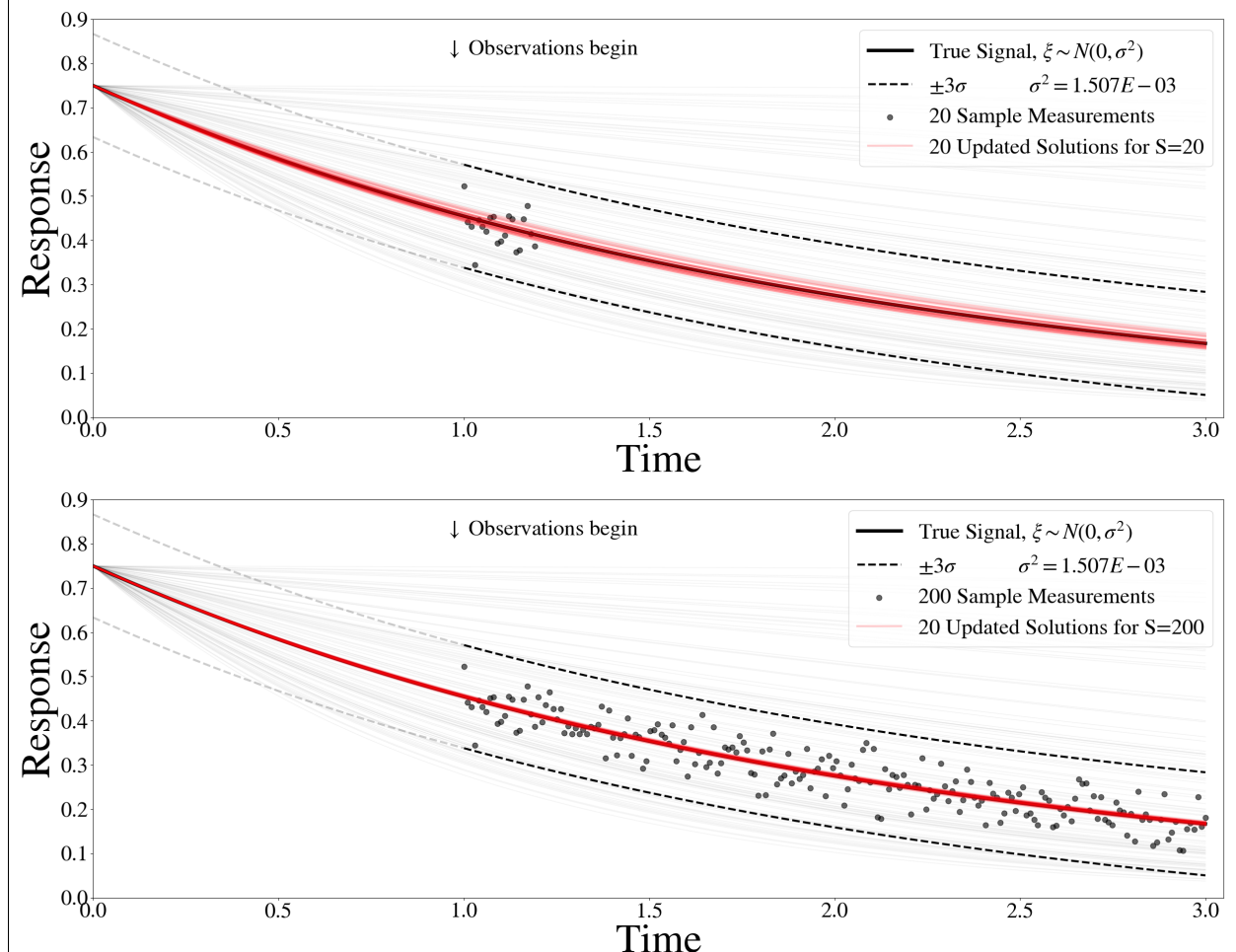


Figure 2.3: Curves for exponential decay model with various decay coefficients. Dashed curves denote 99% probability intervals for noise. The true signal is shown in solid black. Curves associated with the MUD estimates for the decay coefficient computed from 20 trials are shown in light red. Both sets of these curves encompass the true signal for $N = 20$ (top plot) and $N = 200$ (bottom plot) data points. The light red curves are almost indistinguishable in the bottom plot as they all lie nearly on the true signal which demonstrates the overall reduction in variance in MUD estimates around the true signal when using $N = 200$ data points.

For 20 different realizations of $N = 5, 10, 15, 20, 25, 50, 100$, and 200 noisy measurement data, we construct Q_{WME} with $u(t; \lambda)$ replacing $M_j(\lambda)$ in (2.3.2), estimate λ^{MUD} , and analyze the statistical error in these estimates of λ^\dagger . In the left plot of Figure 2.4, we observe that as more data are used that the accuracy (defined by the mean error between λ^{MUD} and λ^\dagger) decreases.

The right plot demonstrates that the precision (i.e., the variance in the error) is also reduced by using more data. These results are also visualized in the plots of Figure 2.3 where the distinct red curves

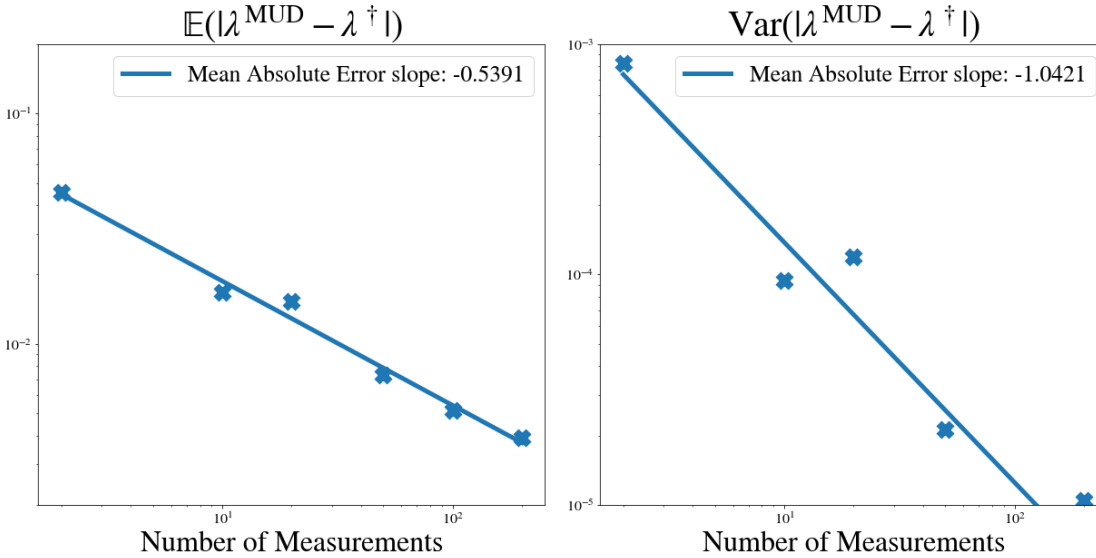


Figure 2.4: The mean (left) and variance (right) of absolute errors in MUD estimates as a function of the number of data points used. These statistics are computed over 20 trials.

in the top plot are the signals associated with the 20 λ^{MUD} estimates associated with the 20 independent trials of $N = 20$ noisy measurements. However, in the bottom plot, these 20 red curves are fairly indistinguishable to the naked eye from the true signal when using $N = 200$ noisy measurements. In Appendix B, we repeat this problem with measurement equipment that operates at double the temporal frequency and show how this change impacts the MUD solutions.

2.4.2 PDE Example

In this problem, the uncertain model parameter is now described by an unknown function defining the boundary data to a stationary PDE. The focus is on demonstrating that a vector-valued QoI can be constructed from noisy data to produce a MUD point that more accurately reconstructs features of the unknown function. As described below, there is an intuitive way to separate the spatial data to construct the distinct components of the vector-valued QoI map. While beyond the scope of this work, a future work will consider how to incorporate clustering analysis on the data for less obvious cases where we seek to determine which data points should be utilized to construct the various components of a vector-valued QoI map. In the interest of clarity, we present representative results for a fixed finite-dimensional representation of the parameter space and forgo the more complicated convergence analysis that requires increasing both the number of data available as well as the dimension of the parameter space.

Consider the Poisson problem:

$$\left\{ \begin{array}{ll} -\nabla \cdot \nabla u &= f(x), \quad \text{on } x \in \Omega, \\ u &= 0, \quad \text{on } \Gamma_T \cup \Gamma_B, \\ \frac{\partial u}{\partial \mathbf{n}} &= g(x_2), \quad \text{on } \Gamma_L, \\ \frac{\partial u}{\partial \mathbf{n}} &= 0, \quad \text{on } \Gamma_R, \end{array} \right. \quad (2.4.2)$$

where $x = (x_1, x_2) \in \Omega = (0, 1)^2$ is the spatial domain; Γ_T , Γ_B , Γ_L , and Γ_R , denote the top, bottom, left, and right boundaries of this domain, respectively, and $\frac{\partial u}{\partial \mathbf{n}}$ denotes the usual outward normal derivative. The forcing function f is taken to be $10 \exp(\|x - 0.5\|^2 / 0.02)$.

Here, we assume that $g(x_2)$ is unknown, and the goal is to use noisy data to estimate this unknown boundary data. In other words, the parameter λ now represents an uncertain function. To generate the noisy data, we use a reference $g(x_2) \propto x_2^2(x_2 - 1)^5$ with a constant of proportionality chosen to produce a minimum of -3 at $x_2 = \frac{2}{7}$. Then, we compute a reference solution using piecewise-linear finite elements on a triangulation of a 36×36 mesh. Random noise is then added to every degree of freedom of this reference solution, and the spatial data are subsequently computed from a fixed set of 100 randomly placed sensors in the subdomain $(0.05, 0.95)^2 \subset \Omega$. This process is repeated 20 times to study the subsequent variation in MUD points due to different realizations of noisy data. See the plot of Figure 2.5 for a representative noisy response surface and location of spatial data used across all 20 trials.

To construct a finite-dimensional parameter space describing the initial uncertainty of $g(x_2)$, we first assume that it is known that g is non-positive and bounded below by -4 . We further assume that g is smooth enough to be reasonably approximated by a piecewise-linear continuous spline with four knots and that $g(0) = g(1) = 0$. Thus, the uncertainty is described by the values of the splines at the two interior knot points chosen as the equispaced points $1/3$ and $2/3$. This defines a finite-dimensional parameter space described by $\Lambda = [0, -4]^2$. We generate 1000 samples from an initial uniform density on Λ to (1) generate random spline functions and compute the (noise-free) data from solutions associated with these splines; and (2) estimate the push-forward and updated densities along with the MUD estimate of $g(x_2)$. The randomly generated splines are shown in the left plot of Figure 2.6 along with the reference g and its interpolant on these spline knots. These same 1000 samples are used across all 20 realizations of random noisy data.

Two separate types of data-constructed Q_{WME} maps are constructed from the data. The first map, which for simplicity we denote by Q_{1D} , uses all 100 spatial data points to construct a scalar-valued

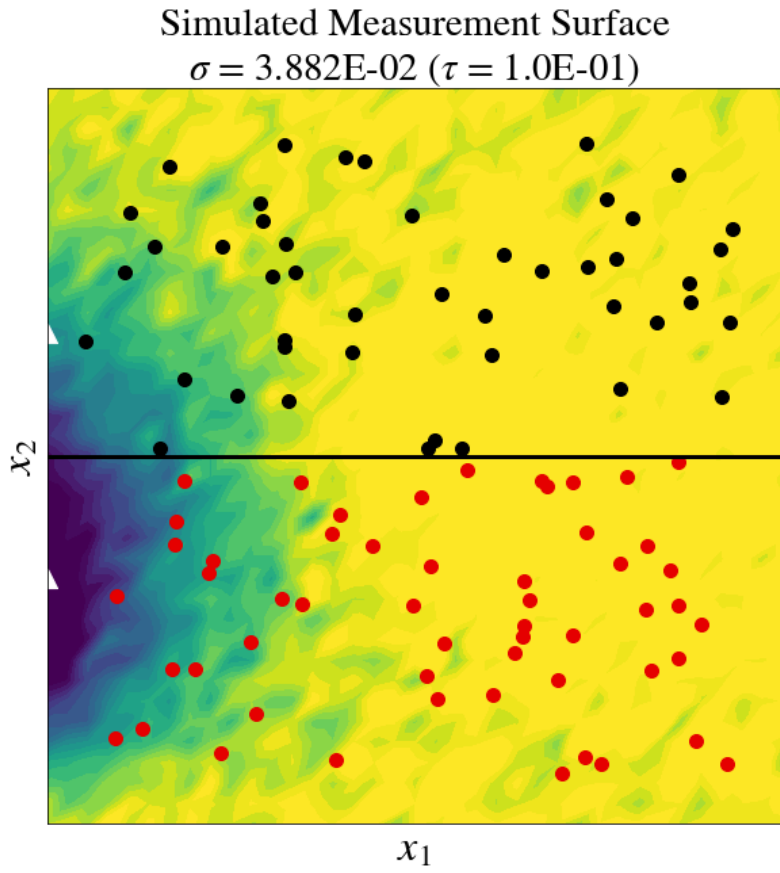


Figure 2.5: A representative noisy perturbation of the reference response surface. Locations of the randomly chosen spatial data used to construct both Q_{1D} and Q_{2D} are shown as black and red dots.

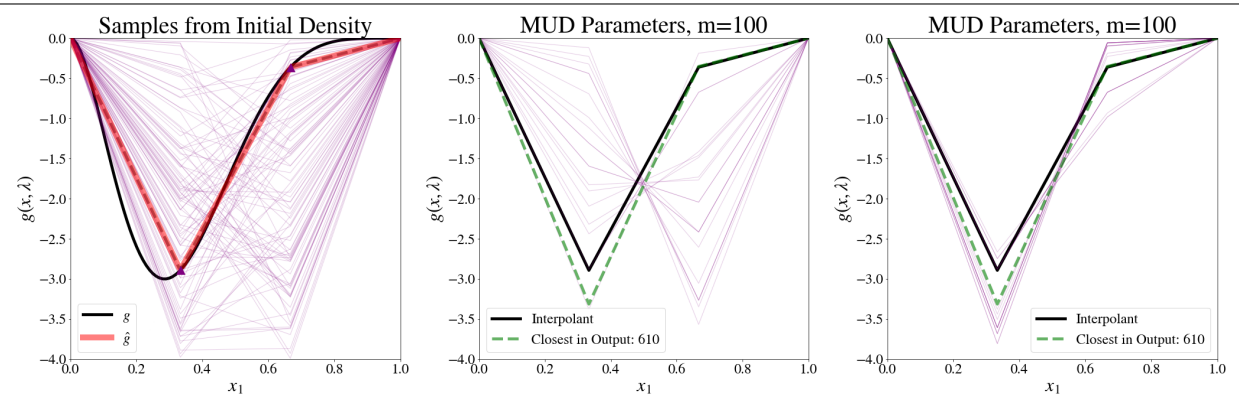


Figure 2.6: In the left plot, the reference $g(x_2)$ is shown as the solid black curve with its interpolant onto the spline basis shown as a dotted red curve. The dashed blue line represents the sample from parameter space which most closely predicts noiseless data, which we refer to as the projection of g . The purple curves in the center and right plots show the variability in MUD estimates of $g(x_2)$ for the 20 different realizations of noisy data. The center plot uses Q_{1D} and the right plot uses Q_{2D} to construct the MUD estimates.

QoI map. Given the location of the spline knots, a second map, which for simplicity we denote by Q_{2D} , uses the data points above (below) the mid-line of the spatial domain to form the first (second) component of the 2-dimensional vector-valued QoI map. This separation of spatial data is illustrated in the top-left plot in Figure 2.5. For reference, the interpolant of the reference $g(x_2)$ on the spline basis is also shown in these plots. The sample from Λ which best predicts the hundred noiseless measurements (in 2-norm) is also shown, referred to as the projection of $g(x_2)$.

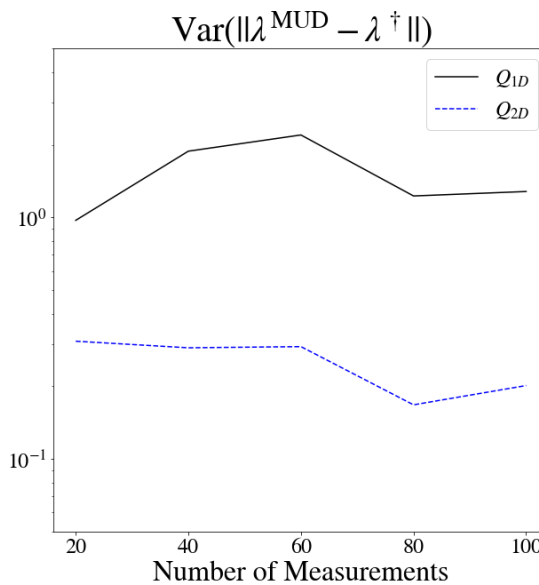


Figure 2.7: A plot of the variance in 2-norm of MUD solutions acquired from solving the SIP with Q_{1D} and Q_{2D} as more measurements are incorporated. The solid black line represents Q_{1D} and the dashed blue line represents Q_{2D} .

The center and right plots in Figure 2.6 shows the variability in the 20 MUD estimates of $g(x_2)$ obtained from the different realizations of noisy data using Q_{1D} and Q_{2D} , respectively. A comparison of these plots suggests the MUD estimates associated with Q_{2D} have less spatial variability than those associated with Q_{1D} , while also being better point-wise estimates for the interpolant or projection of $g(x_2)$. To quantify this reduction in variability, the convergence with respect to the number of measurements incorporated is illustrated in Figure 2.7. There we see that using Q_{2D} for inversion results in a slow but noticeable reduction in variance while Q_{1D} exhibits a slight upward trend. The MUD solutions for Q_{1D} appear unable to resolve which of the two parameters represents a minimum value of g , while Q_{2D} MUD solutions concentrate around the λ_i which best predicts the measurements. The latter solution captures more features of the solution we seek (an estimate of g).

2.4.3 Conclusions

We demonstrate that the QoI map and π_{up} can be modified so that the Data-Consistent SIP can be used for parameter estimation. Specifically, the definition of a particular form of QoI map is utilized that can incorporate an arbitrary stream of data. Then, we recast the problem of solving for a true parameter estimate into one involving the accurate identification of a distribution on the residuals errors predicted by a single parameter. The role of the QoI is central in accomplishing this reformulation, as the distribution being estimated is a direct consequence of the statistical properties of the form of the QoI map.

In Chapter III, we study in abstract the role of QoI maps on the solution to the SIP in the natural context of distribution-estimation. We introduce measures of the QoI map's geometric properties that are directly related to our ability to accurately approximate the distribution using numerical methods. Later, in Chapter IV we leverage this awareness of the geometric properties of the QoI maps and connect them to the goal of parameter identification in the context of the map given in (2.3.2). We demonstrate that the way in which we aggregate available data to construct the QoI map has a direct consequence on the accuracy of the parameter estimate as more data are incorporated, which is hinted at by the last example above.

CHAPTER III

GEOMETRY OF OUTPUT QUANTITIES AND CONSISTENT SOLUTIONS

Here, we describe how the relationship of a geometric quantity called *skewness* in QoI maps impacts the accuracy of consistent solutions to SIPs approximated with random sampling. While prior work has addressed skewness in the context of solving the SIP, its impact on parameter estimation problems formulated within the Data-Consistent framework has not been previously studied. We demonstrate that the skewness of a map impacts the *precision* of a parameter estimate. This is subsequently utilized in Chapter IV to aggregate data into different components of a QoI map to more precisely estimate parameter values.

In this chapter, we begin with a definition of skewness and overview of a set-based approach for constructing consistent solutions to SIPs in 3.1. That review is followed by a series of numerical examples which establish fundamental connections between the skewness of QoI maps and the difficulty of accurately approximating solutions with finite sampling. Namely, we establish that in addition to the implied invariability of skewness to translations, rotations of maps have no impact on solution accuracy. Furthermore, we show that the number of samples required to achieve a predefined level of error is directly proportional to the skewness of the QoI map used to solve the inverse problem.

3.1 A Brief Literature Review of Skewness

In Butler *et al.* (2015), the concept of skewness in a QoI map Q is introduced, quantified, and related to the accuracy in solving the stochastic inverse problem with a finite number of samples. In effect, skewness is a geometric property that describes how the right angles in generalized rectangles belonging to \mathcal{B}_D are transformed by Q^{-1} . An a priori analysis demonstrated that the number of samples from a *regular uniform grid* in Λ required to approximate the μ_Λ -measure of $Q^{-1}(E)$ to a desired level of accuracy is proportional to the skewness of Q raised to the $(d - 1)$ power where d is the dimension of \mathcal{D} . This is a version of the so-called curse-of-dimension for the set-based approach.

Skewness is explored further in Walsh (2017) in the context of optimal experimental design. There, an additional geometric property of Q related to the *precision* in the solution of the associated stochastic inverse problem is introduced and quantified. For completeness, we define skewness below and refer the interested reader to Butler *et al.* (2015); Walsh (2017) for more details.

Definition 11. For any QoI map Q , $\lambda \in \Lambda$, and a specified row vector \mathbf{j}_k of the Jacobian $J_{\lambda, Q}$, we define

$$S_Q(J_{\lambda, Q}, \mathbf{j}_k) := \frac{|\mathbf{j}_k|}{|\mathbf{j}_k^\perp|}. \quad (3.1.1)$$

We define the **local skewness** of a map Q at a point Λ as

$$S_Q(\lambda) := \max_{1 \leq k \leq d} S_Q(J_{\lambda,Q}, \mathbf{j}_k). \quad (3.1.2)$$

Definition 12. The **average (or expected) skewness** is defined as

$$\overline{S_Q} := \frac{1}{\mu_\Lambda(\Lambda)} \int_\Lambda S_Q(\lambda) d\mu_\Lambda \quad (3.1.3)$$

In Walsh (2017), it is shown that $S_Q(\lambda)$ is efficiently computed using a singular value decomposition (SVD) of the Jacobian $J_{\lambda,Q}$, i.e., we randomly sample $J_{\lambda,Q}$ and compute the SVDs. In general, we approximate $\overline{S_Q}$ with Monte Carlo approximations.

We demonstrate that the number of samples required to approximate densities using uniform i.i.d. sampling is proportional to the skewness of the map used for inversion, though the convergence rate of the algorithm used to solve the SIP is unaffected. We focus on the accuracy of the consistent solutions to the SIP. It is illustrative to begin with the original set-based approximations to solutions developed in Breidt *et al.* (2011), Butler *et al.* (2012), and Butler *et al.* (2014a) as the dependence of solutions on skewness is more explicit than in the density-based approach. While the content of this chapter is concerned with estimating distributions and not individual parameter estimates, we remind the reader that the solutions to the SIP are inherently densities. In Chapter II, we used these densities to produce a parameter estimate, and so we are motivated to study the accuracy of these solutions to the SIP.

3.2 Set-Based Inversion for Consistent Measures

To properly summarize the set-based solution, we define several measure/probability spaces and refer to the schematic given in Figure 3.1 in order to illustrate the steps and spaces required in the formulation and solution of the SIP. For a more extensive review, we refer the reader to Butler *et al.* (2014a); Mattis *et al.* (2015b); Breidt *et al.* (2011); Butler *et al.* (2012, 2014a), and Butler *et al.* (2015).

The initial measure/probability spaces involved in the formulation of the SIP are summarized in step (S1) of Fig. 3.1, starting with measure space $(\Lambda, \mathcal{B}_\Lambda, \mu_\Lambda)$. The assumption that Q is at least piecewise-differentiable implies the measurability of the QoI map, so that the space \mathcal{D} induced by Q is equipped with the Borel σ -algebra $\mathcal{B}_\mathcal{D}$ (Hunter and Nachtergael, 2001). The push-forward measure $\mu_\mathcal{D}$ on $(\mathcal{D}, \mathcal{B}_\mathcal{D})$ is defined as

$$\mu_\mathcal{D}(A) = \int_A d\mu_\mathcal{D} := \int_{Q^{-1}(A)} d\mu_\Lambda = \mu_\Lambda(Q^{-1}(A)) \quad \forall A \in \mathcal{B}_\mathcal{D}, \quad (3.2.2)$$

$$\begin{array}{c}
\text{(S1): Stochastic Inverse Problem (SIP)} \\
\overbrace{(\Lambda, \mathcal{B}_\Lambda, \mu_\Lambda) \xrightarrow{Q} (\mathcal{D}, \mathcal{B}_{\mathcal{D}}, \mu_{\mathcal{D}}) \xrightarrow{\mathbb{P}_{\text{ob}}} (\mathcal{D}, \mathcal{B}_{\mathcal{D}}, \mathbb{P}_{\text{ob}}) \xrightarrow{Q^{-1}} (\Lambda, \mathcal{C}_\Lambda, \mathbb{P}_{\mathcal{C}_\Lambda})}^{\text{(S2): Solution to SIP Satisfying Eq. (3.2.2)}} \xrightarrow{\{\mathbb{P}_\ell\}_{\ell \in \mathcal{L}}} (\Lambda, \mathcal{B}_\Lambda, \mathbb{P}_\Lambda) \\
\text{(S3): Unique Solution to SIP by Eq. (3.2.5) and Ansatz}
\end{array} \quad (3.2.1)$$

Figure 3.1: The first step (S1) defines (i) the formulation of the SIP by specification of the model, (ii) the measure spaces of parameters and (iii) observable outputs, and (iv) the probability measure on the latter. The second step (S2) defines a unique solution to the SIP on the space Λ equipped with the contour σ -algebra \mathcal{C}_Λ using the definition of the push-forward measure. In (S3), the Disintegration Theorem and and Ansatz are applied to define a unique solution on the space of interest $(\Lambda, \mathcal{B}_\Lambda)$ equipped with a probability measure \mathbb{P}_Λ .

which defines the measure space $(\mathcal{D}, \mathcal{B}_{\mathcal{D}}, \mu_{\mathcal{D}})$ ¹. In practice, when $\mu_{\mathcal{D}}$ is absolutely continuous with respect to the D -dimensional Lebesgue measure, we substitute the Lebesgue measure for $\mu_{\mathcal{D}}$.

The final step in (S1) involves the specification of a probability measure \mathbb{P}_{ob} on $(\mathcal{D}, \mathcal{B}_{\mathcal{D}})$ to model the uncertainty in data. This leads to the SIP from Def. (2): determine a probability measure \mathbb{P}_Λ on $(\Lambda, \mathcal{B}_\Lambda)$ such that

$$\mathbb{P}_\Lambda(Q^{-1}(E)) = \mathbb{P}_{\text{ob}}(E) \quad \forall E \in \mathcal{B}_{\mathcal{D}}. \quad (3.2.3)$$

This equation implies that any solution is uniquely determined on the induced contour σ -algebra

$$\mathcal{C}_\Lambda = \{Q^{-1}(E) : E \in \mathcal{B}_{\mathcal{D}}\} \subset \mathcal{B}_\Lambda, \quad (3.2.4)$$

which is summarized as step (S2) of Fig. 3.1. However, for sets $A \in \mathcal{B}_\Lambda \setminus \mathcal{C}_\Lambda$, more information is required than is provided in Eq. (3.2.3) in order to determine $\mathbb{P}_\Lambda(A)$. When solutions to the SIP are given by densities, we form a family of conditional densities using an initial density. In the set-based approach, we do not assume an initial density on $(\Lambda, \mathcal{B}_\Lambda)$. Instead, we consider approximations of contour events. Below, we describe these structures and the relationship to the Disintegration theorem.

By the Implicit Function Theorem, if $Q(\lambda) \in C^1(\Lambda)$ and we let $\mathbf{d} \in \mathcal{D}$ be a fixed datum, $Q^{-1}(q)$ exists as a $(P - D)$ -dimensional manifold (possibly piecewise-defined) that we refer to as a *generalized contour* Butler *et al.* (2014a). These generalized contours can be indexed by a D -dimensional manifold (also possibly piecewise-defined) of dimension D called a *transverse parameterization* that intersects each contour once and only once. In Butler *et al.* (2014a), it is shown that transverse parameterizations are guar-

¹When referring to properties of the data space that are not unique to the choice of map used to induce \mathcal{D} , we will drop the subscript notation and assume the dependence is understood, as expressed in Fig. 3.1.

anteed to exist and can be approximated by a finite number of D -dimensional hyperplanes when Λ is compact. In general, the transverse parameterization is not unique.

We let \mathcal{L} denote any particular transverse parameterization. Each $\ell \in \mathcal{L}$ corresponds to a unique generalized contour $\mathcal{C}_\ell \in \Lambda$ and each point $\lambda \in \Lambda$ belongs to a unique $\mathcal{C}_\ell \in \Lambda$. Thus, a transverse parameterization defines a bijection between the manifold \mathcal{L} and the partitioning of Λ into generalized contours that decomposes Λ in terms of equivalence classes. The induced σ -algebra \mathcal{C}_Λ and this bijection can then be used to define the measurable space $(\mathcal{L}, \mathcal{B}_\mathcal{L})$.

We denote the projection map $P_\mathcal{L} : \Lambda \rightarrow \mathcal{L}$, and let $\{\mathcal{C}_\ell\}_{\ell \in \mathcal{L}}$ represent the family of generalized contours indexed by \mathcal{L} , yielding the associated family of measurable spaces $\{(\mathcal{C}_\ell, \mathcal{B}_{\mathcal{C}_\ell})\}_{\ell \in \mathcal{L}}$. By the Disintegration Theorem (Butler *et al.*, 2012; Dellacherie and Meyer, 1978), any \mathbb{P}_Λ is now defined completely in terms of structures embedded in $(\Lambda, \mathcal{B}_\Lambda)$ as a (marginal) probability measure $\mathbb{P}_\mathcal{L}$ on $(\mathcal{L}, \mathcal{B}_\mathcal{L})$ and a family of (conditional) probability measures $\{\mathbb{P}_\ell\}_{\ell \in \mathcal{L}}$ on $\{(\mathcal{C}_\ell, \mathcal{B}_{\mathcal{C}_\ell})\}_{\ell \in \mathcal{L}}$ such that

$$\mathbb{P}_\Lambda(A) = \int_{P_\mathcal{L}(A)} \left(\int_{P_\mathcal{L}^{-1}(\ell) \cap A} d\mathbb{P}_\ell(\lambda) \right) d\mathbb{P}_\mathcal{L}(\ell), \quad \forall A \in \mathcal{B}_\Lambda \quad (3.2.5)$$

The disintegration of Eq. (3.2.5) implies that a specification of a family of conditional probability measures $\{P_\ell\}_{\ell \in \mathcal{L}}$ gives us a unique solution to the SIP on $(\Lambda, \mathcal{B}_\Lambda)$ since the marginal $\mathbb{P}_\mathcal{L}$ on $(\mathcal{L}, \mathcal{B}_\mathcal{L})$ is uniquely determined by \mathbb{P}_{ob} on $(\mathcal{D}, \mathcal{B}_\mathcal{D})$.

The conditional measures are not determined by the specification of \mathbb{P}_{ob} . We follow the work of Butler *et al.* (2014a) and adopt the *standard ansatz* determined by the disintegration of the measure μ_Λ to compute probabilities of sets contained within contour events whenever $\mu_\Lambda(\Lambda) < \infty$, e.g. when μ_Λ is the P -dimensional Lebesgue measure and $\Lambda \in \mathbb{R}^P$ is precompact. The standard ansatz is given by

$$\mathbb{P}_\ell = \mu_{\mathcal{C}_\ell} / \mu_{\mathcal{C}_\ell}(\mathcal{C}_\ell), \quad \forall \ell \in \mathcal{L}, \quad (3.2.6)$$

where $\mu_{\mathcal{C}_\ell}$ is the disintegrated volume measure on generalized contour \mathcal{C}_ℓ . Thus, we have defined a unique solution to the SIP on $(\Lambda, \mathcal{B}_\Lambda)$, completing step (S3) in Fig. 3.1.

In the absence of other information about differences in relative likelihoods of parameters, the standard ansatz effectively implies a uniform distribution describing the initial state of uncertainty about the input parameters². In the vocabulary of the density-based approach, the measure \mathbb{P}_Λ can be viewed as updating an initial uniform measure on Λ in directions informed by the Quantity of Interest map, given uncertain data characterized by \mathbb{P}_{ob} .

²In the event that Λ is compact.

However, unlike the density-based approach that utilizes the pushforward of an initial density in the construction of a solution, the ansatz is imposed only on contours in Λ . Moreover, this does not assume any absolute continuity of probability measures. We next turn our attention to the numerical approximation of the solutions to the SIP that follow from the set-based method.

3.2.1 Numerical Approximation and Analysis

We present a non-intrusive algorithm based on Monte Carlo sampling—initially introduced in Butler *et al.* (2014a) and further analyzed in Butler *et al.* (2014b)—that is structured in four stages (written as four independent for-loops), that are linked to the stages in Fig. 3.1. We direct the interested reader to Butler *et al.* (2014b) for more detailed information and analysis of this algorithm, e.g., on the requirement of a sampler being “ \mathcal{B}_Λ -consistent” to ensure convergence.

Algorithm 2: Numerical Approximation of the Inverse Density

```

Choose a discretization partition  $\{D_k\}_{k=1}^M$  of  $\mathcal{D}$ .
for  $k = 1, \dots, M$  do
    | Compute  $p_{\mathcal{D},k} = \mathbb{P}_{\text{ob}}(D_k)$ .
Choose samples  $\{\lambda^{(i)}\}_{i=1}^N \subset \Lambda$ , which implicitly defines a Voronoi-cell partition  $\{\mathcal{V}_i\}_{i=1}^N$  of  $\Lambda$ .
for  $i = 1, \dots, N$  do
    | Compute  $Q_i = Q(\lambda^{(i)})$ .
    | Let  $\mathcal{O}_k = \{i : Q_i \in D_k\}$ .
    | Compute approximations  $V_i \approx \mu_\Lambda(\mathcal{V}_i)$ .
for  $k = 1, \dots, M$  do
    | Compute  $\mathcal{C}_k = \{i : Q_i \in D_k\}$ .
for  $i = 1, \dots, N$  do
    | Compute  $p_{\Lambda,i} = \left(V_i / \sum_{j \in \mathcal{C}_k} V_j\right) p_{\mathcal{D},\mathcal{O}_i}$ .

```

For any $A \in \mathcal{B}_\Lambda$, compute

$$\mathbb{P}_{\Lambda,M,N}(A) = \sum_{i=1}^N p_{\Lambda,i} \chi_{\mathcal{V}_i}(A) \quad (3.2.7)$$

The first two stages correspond to formulating the discretized version of the SIP given in step (S1) in Fig. 3.1. We first discretize the probability space $(\mathcal{D}, \mathcal{B}_\mathcal{D}, \mathbb{P}_{\text{ob}})$. Then, we simultaneously discretize the measure space $(\Lambda, \mathcal{B}_\Lambda, \mu_\Lambda)$ and construct a simple-function approximation to the map Q . These stages introduce the primary sources of error, and the third and fourth stages may be thought of as solving the discretized SIP exactly. The samples that are used to describe Λ implicitly define a set of Voronoi cells $\{\mathcal{V}_i\}_{i=1}^N$, which can be seen in Figure 3.2. Each sample set defines a fundamentally different geometry.

The third stage then identifies the collection of Voronoi cells in Λ that approximate the contour events in \mathcal{C}_Λ defined by $Q^{-1}(D_k)$ for $k = 1, \dots, M$. This allows us to formulate the consistent solution to the discretized SIP on $(\Lambda, \mathcal{C}_\Lambda, \mathbb{P}_{\mathcal{C}_\Lambda})$ as illustrated in step (S2) of Fig. 3.1. The fourth stage, associated

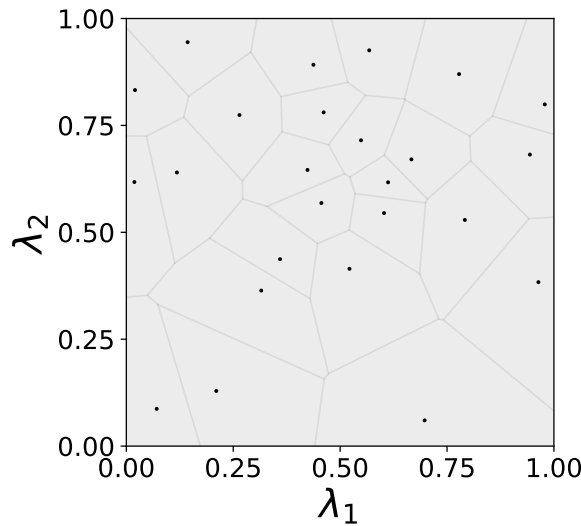


Figure 3.2: Voronoi-cell discretization (partition) induced by $N = 25$ uniform i.i.d. random samples in $\Lambda = [0, 1]^2$.

with step (S3) in Fig. 3.1, uses a discrete version of the ansatz to approximate the probability of \mathcal{V}_i for $i = 1, \dots, N$. This results in an approximate probability measure, denoted by $\mathbb{P}_{\text{up},N,M}$, which produces the same probability estimates for events A and $A \setminus \{\lambda^{(i)}\}_{i=1}^N$, which are identical almost everywhere with respect to μ_Λ .

Note that Algorithm 2 makes no mention of the method by which the samples $\{\lambda^{(i)}\}_{i=1}^N$ were generated or sets in $\{D_k\}_{k=1}^M$ are chosen. $\{\lambda^{(i)}\}_{i=1}^N$ may be generated using uniform random sampling, Latin-hypercube sampling, or even regular grids. A thorough discussion of the choices involved in making such decisions is beyond the scope of this work, though we touch briefly on the discretization of \mathcal{D} in the following section.

3.2.2 Descriptions of Error

If we assume π_{ob} is absolutely continuous with respect to $\mu_{\mathcal{D}}$, we can describe π_{ob} with a density \mathbb{P}_{ob} . Then, for any partition $\{D_k\}_{k=1}^M$ of \mathcal{D} ,

$$\pi_{\text{ob}}(D_k) = \int_{D_k} \pi_{\text{ob}} \, \mu_{\mathcal{D}}, \quad \text{for } k = 1, \dots, M.$$

We often use Monte Carlo approximations to compute the approximations $p_{\mathcal{D},k} = \pi_{\text{ob}}(D_k)$ in the first for-loop in Algorithm 2. These samples are generated on \mathcal{D} and do not require numerical solutions to the model. We therefore assume that for any discretization of \mathcal{D} , these approximations can be made sufficiently accurate and neglect the error in this computation.

We denote the exact solution to the SIP associated with this partitioning of \mathcal{D} by $\mathbb{P}_{\Lambda,M}$. In situations where $Q(\lambda^{(i)})$ is estimated (e.g. by application of a functional on a finite-element solution to a PDE), the approximate solutions to the SIP given in the final for-loop of Algorithm 2 are denoted by $\mathbb{P}_{\Lambda,M,N,h}$. Here, the h is in reference to a mesh or other numerical parameter that determines the accuracy of the numerical solution $u_h(\lambda^{(i)}) \approx u(\lambda^{(i)})$, and subsequently the accuracy in the computations of $Q_i = Q(\lambda^{(i)})$ in Algorithm 2. Then, by repeated application of the triangle inequality,

$$d(\mathbb{P}_{\Lambda,M,N,h}, \mathbb{P}_\Lambda) \leq \underbrace{d(\mathbb{P}_{\Lambda,M,N,h}, \mathbb{P}_{\Lambda,M,N})}_{(E1)} + \underbrace{d(\mathbb{P}_{\Lambda,M,N}, \mathbb{P}_{\Lambda,M})}_{(E2)} + \underbrace{d(\mathbb{P}_{\Lambda,M}, \mathbb{P}_\Lambda)}_{(E3)}. \quad (3.2.8)$$

The term (E1) describes the effect of the error in the numerically evaluated Q_i on the solution to the SIP. The term (E2) describes the effect of finite sampling error in Λ on the solution to the SIP and (E3) describes the effect of discretization error of π_{ob} on the solution to the SIP.

We assume that h is tunable so that for any $A \in \mathcal{B}_\Lambda$,

$$\lim_{h \downarrow 0} \mathbb{P}_{\Lambda,M,N,h}(A) = \mathbb{P}_{\Lambda,M,N}(A).$$

It is possible to prove the convergence of $\mathbb{P}_{\Lambda,M,N,h}(A) \rightarrow \mathbb{P}_\Lambda(A)$ for some $A \in \mathcal{B}_\Lambda$ and on estimating the error in $\mathbb{P}_{\Lambda,M,N,h}(A)$. For example, in Butler *et al.* (2015), adjoint-based a posteriori estimates in the computed QoI are combined with a statistical analysis to both estimate and bound the error in $\mathbb{P}_{\Lambda,M,N,h}(A)$. In Mattis and Butler (2019), adjoints are used to compute both error and derivative estimates of $Q(\lambda^{(i)})$ to improve the accuracy in $\mathbb{P}_{\Lambda,M,N,h}(A)$. Since the error due to h can be estimated as described in previous studies, and M can be made arbitrarily large, we neglect (E1) and (E3) here. Thus, we limit our focus to (E2), where certain geometric properties of the QoI map (namely, skewness), are known to significantly impact this term.

3.2.3 Convergence

To study the accuracy of the solutions to SIPs using QoI maps with different skewness values (or number of available model evaluations), we need to select a metric on the space of probability measures. Rates of convergence depend on this choice. Since the spaces Λ we are considering are generally bounded and finite, the Total Variation metric metrizes weak convergence (see Thm. 6 in Gibbs and Su (2002)). The latter property of the metric is of notable importance because the QoI maps we study are indeed (component-wise) functionals on the space of model inputs Λ . Thus, convergence of a sequence of probability measures under the Total Variation metric implies that the QoIs will also converge component-wise

in \mathbb{R} . In other words, convergence in the Total Variation metric implies the convergence of the sampled QoI map to the exact QoI map since the map is a linear functional of the probability measure. More formally, if $\mathbb{P}_{\Lambda,M,N,h}$ converges to either $\mathbb{P}_{\Lambda,M,N}$, $\mathbb{P}_{\Lambda,M}$, or P_Λ using the Total Variation metric, this implies that the error converged to zero in the numerically computed $Q(\lambda^{(j)})$. Thus, convergence in the Total Variation metric implies convergence of the numerical method used to construct the QoI map. Furthermore, recall that weak convergence $\mathbb{P}_n \rightarrow \mathbb{P}$ is defined to mean

$$\int f \mathbb{P}_n \rightarrow \int f \mathbb{P} \text{ as } n \rightarrow \infty$$

for bounded Lipschitz functions $f : \Lambda \rightarrow \mathbb{R}$. Taking $f = \chi_A$, this leads to the following implication:

$$\mathbb{P}_{\Lambda,M,N} \rightarrow P_\Lambda \implies \mathbb{P}_{\Lambda,M,N}(A) \rightarrow P_\Lambda(A) \quad \forall A \in \mathcal{B}_\Lambda.$$

We choose Total Variation as the metric used in the numerical results of Section 3.2.4 because of its common use in the literature as the “statistical distance” between densities Gibbs and Su (2002); Silverman (1986), and implications for convergence.

3.2.4 Accuracy of Set-Based Inversion

In this section, we address how to measure the distance between measures that are defined on different discretizations to ensure that the computations make sense mathematically. There is a correspondence between the objects from measure theory that are involved in the SIP, and the finite-state counterparts in the algorithmic implementation. Therefore, we begin by summarizing the relationship between the random samples we generate and the Borel σ -algebra.

The measures computed from Algorithm 2 are defined on a set of samples $S = \{\lambda^{(j)}\}_{j=1}^N$ which implicitly define a Voronoi-cell partition $\{\mathcal{V}^{(j)}\}_{j=1}^N$ of the parameter space Λ . We let $\mathcal{B}_{\Lambda,N}$ denote the *computational algebra* generated by $\{\mathcal{V}^{(j)}\}_{j=1}^N$, i.e., using standard measure theory notation,

$$\mathcal{B}_{\Lambda,N} = \sigma \left(\left\{ \mathcal{V}^{(j)} \right\}_{j=1}^N \right).$$

$\mathcal{B}_{\Lambda,N} \subset \mathcal{B}_\Lambda$ and the events $A \in \mathcal{B}_{\Lambda,N}$ represent the $A \in \mathcal{B}_\Lambda$ for which we can compute probabilities and make inferences. While Algorithm 2 ultimately defines a probability measure implicitly on $(\Lambda, \mathcal{B}_\Lambda)$, computationally this is almost never done; instead, the measures are only interrogated on the computational algebra associated with the finite set of samples.

Different sets $S_k = \{\lambda^{(i)}\}_{i=1}^{N_k}$, where the $\lambda^{(i)}$'s and N_k 's may differ for each k , will lead to different measures computed from Algorithm 2. Each S_k induces a computational algebra which we index using the notation \mathcal{B}_k for simplicity, where it is understood that $\mathcal{B}_k = \mathcal{B}_{\Lambda, N_k}$. The fact that solutions are defined on different sub- σ -algebras poses an immediate problem with respect to a computational approach to computing the distances between measures $\mathbb{P}_{\Lambda, M, N_1}$ and $\mathbb{P}_{\Lambda, M, N_2}$ even if $N_1 = N_2$. See Figure 3.3 for an example illustration of this scenario.

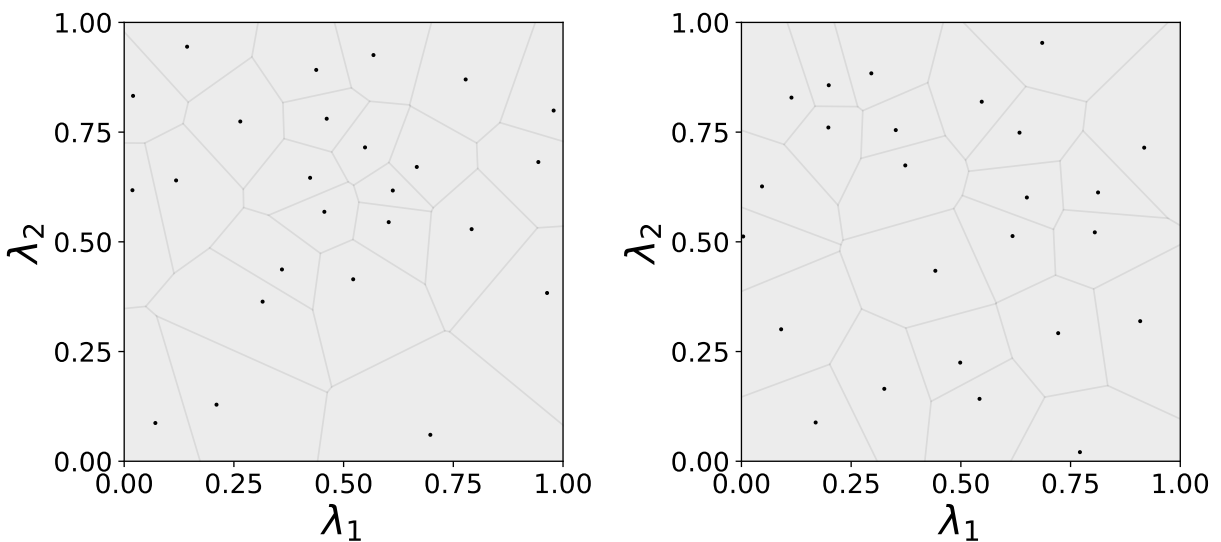


Figure 3.3: Two different Voronoi partitions induced by $N_1 = N_2 = 25$ uniform i.i.d. random samples.

The proof of the following Lemma describes how to extend *any* probability measure defined on a computational algebra to the full σ -algebra \mathcal{B}_Λ , which we exploit in Algorithm 3.

Lemma 1. *Let μ be a measure on $(\Lambda, \mathcal{B}_\Lambda)$, $\{\mathcal{V}^{(j)}\}_{j=1}^N$ be a partition of Λ , and $\mathcal{B}_{\Lambda, N}$ the computational algebra generated by $\{\mathcal{V}^{(j)}\}_{j=1}^N$. Assume $\mu(\mathcal{V}^{(j)}) > 0 \ \forall j = 1, \dots, N$. Then, there exists a probability measure η on $(\Lambda, \mathcal{B}_\Lambda)$ such that $\eta(A) = \eta_N(A) \ \forall A \in \mathcal{B}_{\Lambda, N}$.*

In the proof below, we use η_N and μ to construct a type of discrete Radon-Nikodym derivative of η . This is motivated by the formal structure of solutions given by Algorithm 2. The proof of Lemma 1 can be found in Appendix A, but the two key equations involved are reproduced here for later reference:

$$f_N(\lambda) = \sum_{j=1}^N \frac{\eta_N(\mathcal{V}^{(j)})}{\mu(\mathcal{V}^{(j)})} \chi_{\mathcal{V}^{(j)}}(\lambda). \quad (3.2.9)$$

Then, for any $A \in \mathcal{B}_\Lambda$, define

$$\eta(A) = \int_A f_N(\lambda) d\mu. \quad (3.2.10)$$

We note that in practice, $\chi_{\mathcal{V}^{(j)}}(\lambda)$ requires the use of nearest-neighbor computations, but otherwise evaluation of Eq. (3.2.9) is straightforward.

Algorithm 3: Total Variation Discretization

Let $(\Lambda, B_{\Lambda, N_1}, \eta_{N_1})$ and $(\Lambda, B_{\Lambda, N_2}, \eta_{N_2})$ be given.

Construct f_{N_1} and f_{N_2} and corresponding η_1, η_2 using Eq. (3.2.9) and Eq. (3.2.10), respectively.

Use Monte Carlo sampling to approximate

$$d_{\text{TV}}(\eta_1, \eta_2) = \int_{\Lambda} |f_{N_1}(\lambda) - f_{N_2}(\lambda)| d\mu.$$

Since we now have a way to extend probability measures defined on $(\Lambda, \mathcal{B}_{\Lambda, N})$ to probability measure on $(\Lambda, \mathcal{B}_{\Lambda})$, we can use simple Monte Carlo approximation schemes to the Total Variation distance between two probability measures defined on two separate computational algebras. This is demonstrated in Algorithm 3.

3.3 Numerical Results and Analysis

We first investigate what values of N are appropriate provided the goal is to resolve $d(\mathbb{P}_{\Lambda, M, N}, \mathbb{P}_{\Lambda, M})$ to a desired level of accuracy so that

$$d(\mathbb{P}_{\Lambda, M, N}, \mathbb{P}_{\Lambda, M}) < \tau, \quad (3.3.1)$$

where τ is some designated tolerance. The reason for this is because the choice of Q will influence the number of model solutions necessary to accurately solve the SIP as shown in Butler *et al.* (2015). Different choices for Q may lead to radically different values for N in order to achieve the same bound on $d(\mathbb{P}_{\Lambda, M, N}, \mathbb{P}_{\Lambda, M})$ as we see in the following examples. By phrasing the analysis in terms of metrics, we are able to answer more broadly generalizable questions about error, including those regarding convergence rates and global accuracy of the estimates.

3.3.1 Overview of Examples

We establish some fundamental properties of solutions to the SIP under different QoI maps in terms of the skewness of the Q 's being compared. We seek an estimated probability measure $\hat{\mathbb{P}}_{\Lambda}$ on the parameter space to converge (with respect to the metric d_{TV}) to some reference measure \mathbb{P}_{Λ} as more samples (i.e., model evaluations), N are used. Such a reference measure could be either some known distribu-

tion taken as truth, or another approximation deemed to be sufficiently resolved for the given application or computational budget (i.e. higher-fidelity model, mesh, or Monte Carlo sample-size).³

In Figure 3.4, we illustrate the solution to the problem of comparing measures defined on two different (implicitly-defined) σ -algebras shown in Figure 3.3. By introducing a third set against which both sample sets of size $N = 50$ are compared, we can leverage theoretical results from Lemma 1 to compare solutions to the SIP under different QoI maps.

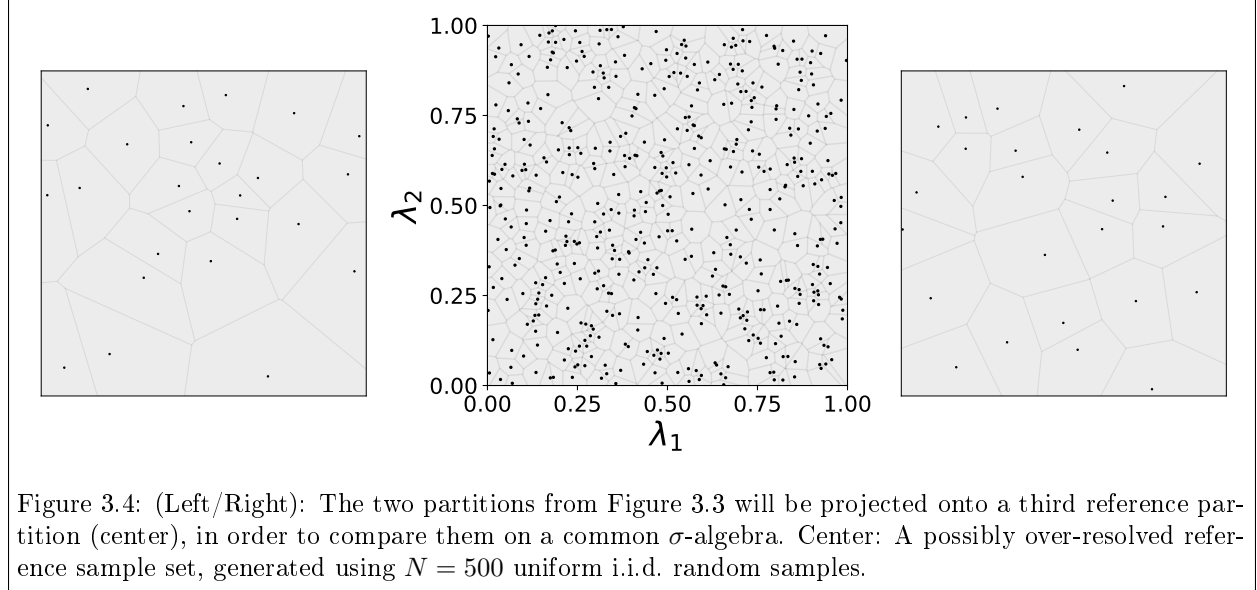


Figure 3.4: (Left/Right): The two partitions from Figure 3.3 will be projected onto a third reference partition (center), in order to compare them on a common σ -algebra. Center: A possibly over-resolved reference sample set, generated using $N = 500$ uniform i.i.d. random samples.

To isolate the effect of skewness on the ability to approximate sets with finite sampling, we choose the maps so that they preserve the sizes of sets between Λ and \mathcal{D} under the push-forward measure given in Eq. (3.2.2). The sizes of these inverse sets correspond to the average precision of maps Q , so we fix the maps to all be equally informative from this perspective; for linear maps, this means they all have the same determinant.

All of our experiments follow the same structure, where \mathcal{Q} denotes a set of QoI maps under consideration in each example:

[0-a] Select $Q \in \mathcal{Q}$ and define $\mathbb{P}_{\mathcal{D}_Q}$ as a uniform distribution centered on a reference QoI value $Q(\lambda^\dagger)$ for λ^\dagger taken as the midpoint of Λ . Note that $\mathbb{P}_{\mathcal{D}_Q}$ is exactly discretized with $M = 1$ sample, so that

$$P_{\Lambda,1} = P_\Lambda.$$

³However, we could also choose to interrogate the push-forward measures given by propagating the $\hat{\mathbb{P}}_\Lambda$ and \mathbb{P}_Λ forward to a data space by a QoI map and taking the distance on the resulting output space. This would measure the ability of the maps to reconstruct the output probability measure.

[0-b] Create a regular grid of samples in $\Lambda = [0, 1]^n$ using $N_{\text{ref},i}$ equispaced points in each dimension. Set $\bar{N} := \prod N_{\text{ref},i}$. Since n is small in the numerical examples shown here, we select $N_{\text{ref},i} = 200 \forall i$ in each example.

[0-c] Use Algorithm 2 to construct a reference solution $\mathbb{P}_{\Lambda, \bar{N}} \approx \mathbb{P}_\Lambda$.

[1] Generate $\left\{ S_k^{(n)} \right\}_{n=1}^{50}$ sets of uniform i.i.d. random samples where $N_k = 25, 50, 100, 200, \dots, 6400$, and n represents the number of repeated trials of a sample size N_k .

[2] Solve the SIPs using Algorithm 2 to construct $\left\{ \mathbb{P}_{\Lambda, M, N}^{(n)} \right\}_{n=1}^{50}$.

[3] Use $1E5$ i.i.d. random samples to estimate $\left\{ d_H^2(\mathbb{P}_{\Lambda, M, N}^{(n)}, \mathbb{P}_{\Lambda, \bar{N}}) \right\}_{n=1}^{50}$.

[4] Average over all trials n for each N to estimate the *expected* Total Variation distance for N samples and analyze convergence to $\mathbb{P}_{\Lambda, \bar{N}}$.

[5] Repeat steps [0-a]–[4] for each $Q \in \mathcal{Q}$ under consideration.

3.3.2 Rotational Invariance

This example shows that if $Q^{(a)}$ is defined by a rotation of $Q^{(b)}$, then the accuracy and convergence rates of $\mathbb{P}_{\Lambda, M, N}^{(a)}$ are identical to $\mathbb{P}_{\Lambda, M, N}^{(b)}$. We expect this to be true since skewness is rotationally invariant, as we summarize in the following Proposition.

Proposition 1. *The quantity $S_Q(\lambda)$ is invariant under rotations performed on Q for any λ .*

Proof. If we apply a rotation Q , then the Jacobians $J_{Q,\lambda}$ are also subject to the same rotation at each λ . Since rotations are unitary operators, the norms given in Eq. (3.1.1) used to define skewness are unaffected. \square

To demonstrate this Lemma numerically, we define the space of QoI maps $\mathcal{Q} = \{Q^{(a)}, Q^{(b)}, Q^{(c)}\}$, where all three are linear maps with the same local skewness $S_Q(\lambda) = 1 \forall \lambda \in \Lambda$. The map $Q^{(a)}$ is the identity and the other two, $Q^{(b)}$ and $Q^{(c)}$ are rotations of $Q^{(a)}$ by randomly chosen angles. Following the algorithmic outline above, we perform a convergence study to $\mathbb{P}_{\Lambda, \bar{N}}$ with results summarized in Figure 3.5. The convergence rates and expected errors in the SIPs associated with each of these maps are virtually indistinguishable. In light of Proposition 1 and these numerical results, we conclude that the accuracy of the numerical solution to the SIP is invariant under rotations to the QoI map.

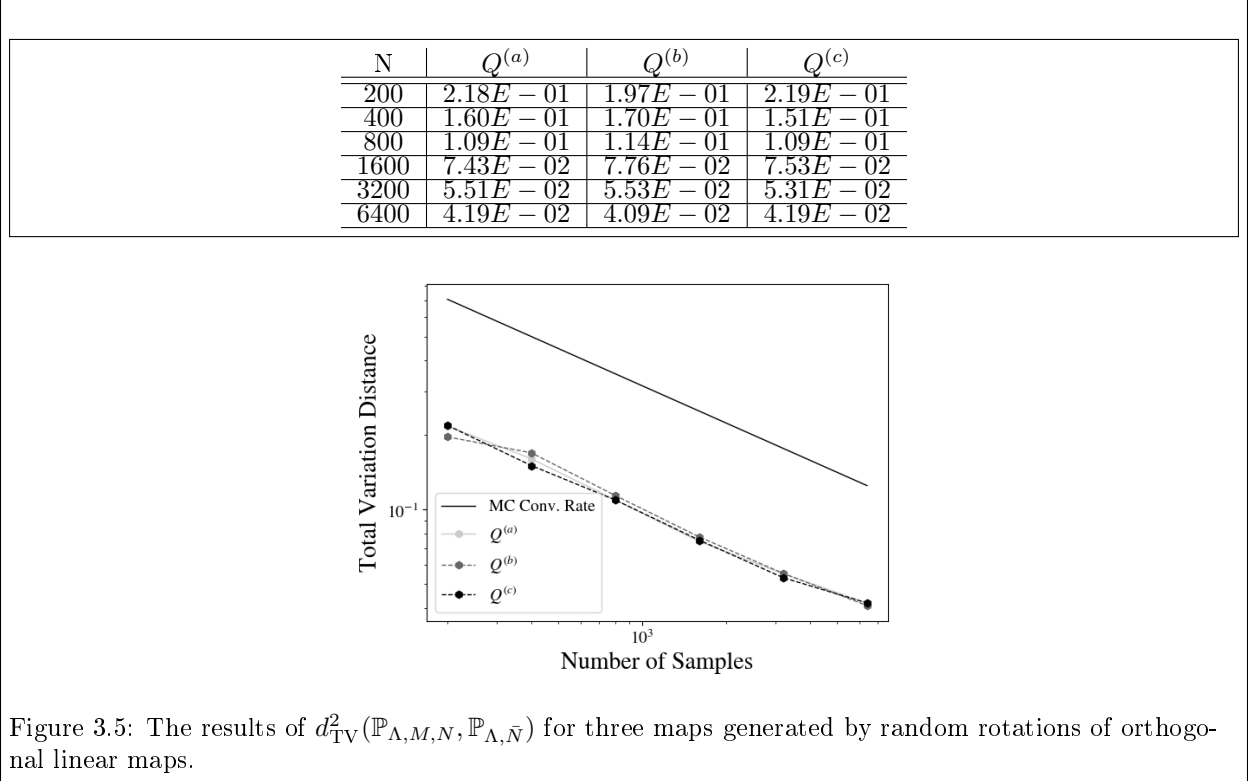


Figure 3.5: The results of $d_{\text{TV}}^2(\mathbb{P}_{\Lambda, M, N}, \mathbb{P}_{\Lambda, \bar{N}})$ for three maps generated by random rotations of orthogonal linear maps.

3.3.3 Impact of Skewness on Accuracy

In this example, we demonstrate the key point of this study: the magnitude of skewness between QoI maps impacts accuracy by orders of magnitude, and thus in optimizing the choice of a QoI map, it is in our interest to pursue the minimization of skewness. This is especially true in problems where the number of random samples we are permitted to use is constrained by the computational cost of model evaluations.

To illustrate this point, we first define the linear maps:

$$Q_S := \left\{ Q^{(s)} = \begin{bmatrix} 1 & 0 \\ \sqrt{s^2 - 1} & 1 \end{bmatrix} \right\}_{s \in S}, \quad (3.3.2)$$

for $S = \{1, 2, 4\}$ because they allow us to control the global skewness (since it is equal to local skewness in a linear map) while preserving the measures of sets between Λ and \mathcal{D} . More specifically, the support of the solution to the SIP associated with each QoI map has equal μ_Λ -measure, which isolates the impact of accuracy solely to the skewness of the QoI map. The skewness of these maps is given by the index s , so $Q^{(1)}$ is 1, the skewness of $Q^{(2)}$ is 2, and $S_{Q^{(4)}} = 4$.

The displaced horizontal lines and accompanying table in Figure 3.6 demonstrate that skewness has a direct impact on the number of samples required to achieve a particular value for the Total Vari-

N	$Q^{(a)}$	$Q^{(b)}$	$Q^{(c)}$
200	$2.02E - 01$	$2.49E - 01$	$3.37E - 01$
400	$1.75E - 01$	$2.16E - 01$	$2.58E - 01$
800	$1.19E - 01$	$1.45E - 01$	$1.81E - 01$
1600	$8.23E - 02$	$9.67E - 02$	$1.29E - 01$
3200	$6.10E - 02$	$7.15E - 02$	$9.22E - 02$
6400	$3.96E - 02$	$5.47E - 02$	$6.39E - 02$

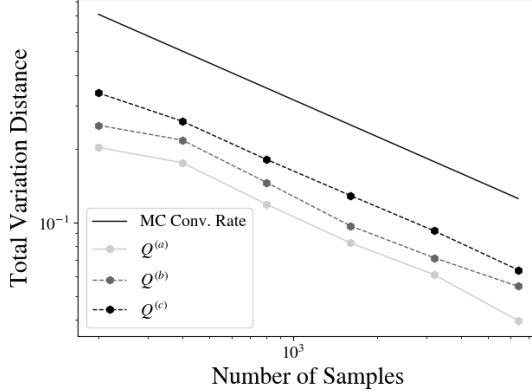


Figure 3.6: The results of $d_{\text{TV}}^2(\mathbb{P}_{\Lambda, M, N}, \mathbb{P}_{\Lambda, M, \bar{N}})$ for $M = 1, \bar{N} = 40,000$, with $a, b, c = 1, 2, 4$ in two dimensions.

ation distance. By comparing adjacent columns in the table, it appears that if the ratio of skewness between two maps is 2, then the more-skewed map will require approximately twice as many random samples to approximate the set on a well-resolved discretization with the same error tolerance. We observe that the measure induced by $Q^{(1)}$ requires fewer than half the number of samples to be as accurately resolved as $Q^{(2)}$ does. The effect is even more pronounced when compared against $Q^{(4)}$.

The fact we can achieve the same accuracy with fewer model evaluations provides a strong motivation for minimizing skewness and reinforces the results from Bryant *et al.* (2015). There, it was demonstrated that a similar relationship existed in the number of samples required to remove error in inverse set approximations quantified by the μ_Λ -measure of the *symmetric difference* of the inverse sets. Rather than study the support of the distributions as was the focus in Bryant *et al.* (2015), we turn our attention to a formal measure of accuracy for the densities or measures involved in the solution to the SIP. We have shown that the skewness has an impact not only on the symmetric difference error, but also on the approximation error as measured by Total Variation.

3.3.4 Dependence on Dimension

To further illustrate that relationship between skewness and accuracy holds as we move towards higher dimensions, we extend the numerical investigation to a three-dimensional parameter space. Gener-

ally, we have fewer QoI than number of uncertain model parameters, so we assume that the potential QoI maps are defined by the 2×3 matrices

$$\mathcal{Q}_S := \left\{ Q^{(s)} = \begin{bmatrix} 1 & 0 & 0 \\ \sqrt{s^2 - 1} & 1 & 0 \end{bmatrix} \right\}_{s \in S}. \quad (3.3.3)$$

Here, as in the previous example, the index s indicates the magnitude of skewness. Furthermore, the results of Example 3.3.2 justify the restriction of the maps to this form since any linear map of skewness s is simply a rotation of maps of this form.

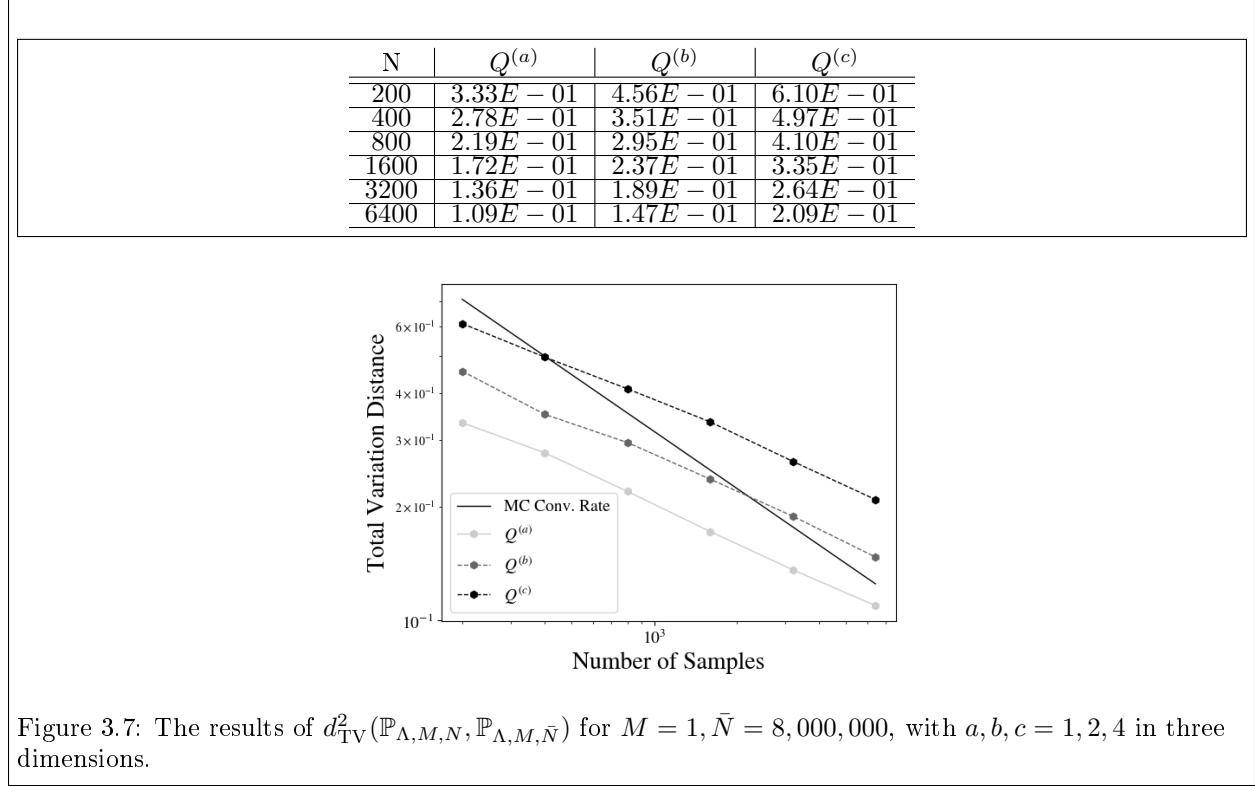


Figure 3.7: The results of $d_{\text{TV}}^2(\mathbb{P}_{\Lambda, M, N}, \mathbb{P}_{\Lambda, M, \bar{N}})$ for $M = 1, \bar{N} = 8,000,000$, with $a, b, c = 1, 2, 4$ in three dimensions.

In Figure 3.7, it appears that the effect of skewness is even more pronounced in higher dimensions, and that the number of samples required to achieve similar levels of accuracy between two maps with a ratio of skewness 2 is now quadrupled. The analysis of Butler *et al.* (2015) suggested a dependence of accuracy related to the skewness raised to a power related to the dimension of the data space.

3.4 Conclusions

In this chapter we reviewed the skewness property of QoI maps and demonstrated that for solutions to the SIP, maps which exhibit lower values of skewness exhibit lower overall finite-sampling approximation error against a reference solution. We saw that the solutions are invariant to transformations such as rotation (which also holds for translations). The latter observation may aid in the selection of optimal

maps (i.e., one can disregard the direction of the maps' contours and focus solely on the angles among the generalized contours). In the following chapter, we show how vector-valued QoI maps such as those in Chapter II constructed from data relate to the geometry of the resulting data-spaces and subsequently impacts the solutions to the SIP. We demonstrate that even a basic awareness and consideration of skewness can aid in the construction of maps which are more informative and thus increase the precision of parameter estimates.

CHAPTER IV

EXTENSIONS AND APPLICATIONS OF MUD POINTS AND SKEWNESS

In Chapter III, we introduced the notion of skewness and showed examples of how it impacts the accuracy of approximating SIP solutions with finite sampling. Here, we demonstrate how an awareness of skewness allows us to a priori define a QoI that will—on average—better resolve λ^\dagger by providing information in mutually distinct directions in Λ . We begin by revisiting the example in Section 2.4.2 involving the Poisson problem and uncertain Neumann boundary condition g . Recall that Q_{2D} is able to better resolve λ^\dagger (in this case, λ^\dagger is defined by a finite-dimensional representation of an exact g), than Q_{1D} . The map Q_{2D} is presented as an alternative option for aggregating the same 100 measurements and using them to construct a more informative 2D map. In this chapter, we present a more detailed study of the construction of this map, and perform a case-study in designing a problem where the data-constructed QoI map is more informative.

4.1 Skewness and Vector-Valued Data-Constructed QoI Maps

In our first example, we show that for the problem in 2.4.2, a small change in the decision of how to aggregate the measurements collected on the response surface can induce a 2-dimensional map Q'_{2D} which is “effectively” one-dimensional; the two components provide highly correlated information. Such a map is, by definition, more skewed than the one we presented with Q_{2D} . Therefore, Q'_{2D} leads to MUD-point solutions that exhibit similar behavior to those obtained with Q_{1D} . This decreased precision demonstrates that skewness—although reviewed and analyzed in the previous chapter within the context of accuracy of set-valued solutions—is a relevant measure of a map’s utility for solving parameter identification problems.

The examples in Sections 2.4.1 and 2.4.2 motivate the use of a data-constructed QoI in order to incorporate an arbitrary number of measurements in a system into a scalar-valued map. These examples are chosen so that $\dim(\Lambda) = 1$ for simplicity and to establish a baseline for convergence results. The linear examples in Section 2.2 demonstrate that the DCI framework maintains the accuracy of least-squares while incorporating initial beliefs for higher-dimensional linear maps. In those examples, we show that the ability to resolve a true parameter improves as the gap between input dimension and operator row-rank decreases.

The rank-deficiency of an operator is attributed to either the ill-conditioning of an operator $A : P \rightarrow P$, or when $P > D$ for a full-rank $A : P \rightarrow D$. In scenarios where $S > P$ observations are available, we are motivated to leverage the form of Eq. (2.3.2) to construct a vector-valued version of the QoI map incorporating subsets of S for each component. For example, a system for which spatial measurements

are available over time may motivate constructing a scalar-valued QoI map using the WME functional for each spatial location. If distinct observable quantities are available (e.g., perhaps with different physical units), then these may be collapsed into each component of the map.

The discussion of how to optimally construct such maps is beyond the scope of this work, and is highly problem specific, requiring nuances involving measurement sensitivities and combinatorial design-spaces. However, we summarize that the extension of the equations presented in Section 2.3.2 follows directly by constructing the resultant $1 \times P$ matrices A and scalar-valued b for each component and then stacking them to form a $D \times P$ system, where we are motivated to minimize $P - D$. The choice of how to form each of the (up to) P components will directly impact the precision of the parameter estimate.

4.1.1 Revisiting Example 2.4.2

Recall that aggregating spatial data into two separate components on Q_{2D} provides a tangible benefit for resolving the uncertainty in the true function g as seen in Example 2.4.2. However, we did not present how the map Q_{2D} was selected. To explore the impact of various choices in how data may be aggregated into components of a QoI map, we propose two methods for splitting the measurements into two subsets to construct the respective components of the map according to (2.3.2). An illustration of the partitioning for both methods is shown in the top half of Figure 4.1; a bisection of Ω into vertically-oriented halves is used to form Q'_{2D} and (as before) horizontal ones for Q_{2D} .

The choice of which partitioning method to use is akin to the following question:

With two possible QoI maps under consideration, which should we use?

We use heuristics and an understanding of skewness to help address this question. For the data-constructed (WME) QoI map, the observed distribution for which we seek a pullback measure is fixed as a standard multivariate Gaussian, independent of the number of measurements that were used. The initial density is also a fixed quantity, implying that any differences in the updated density will be attributed to differences in the predicted density. To understand how the precision of the MUD estimate will change as more measurements are incorporated into the map, we visualize the data spaces induced by the WME QoI for increasing number of measurements $D = 20, 60$, and 100 .

We sample the predicted data spaces using simulated spatial data associated with 1000 parameter samples. To build intuition about how the underlying geometry induced by these maps changes, we plot the scatter-plots representing a visualization of the associated data spaces in the bottom half of Figure 4.1. This figure also shows the associated designs against the noisy response surface as a backdrop. The inclusion of more data points has the effect of dilating (and to some extent rotating) the induced data space

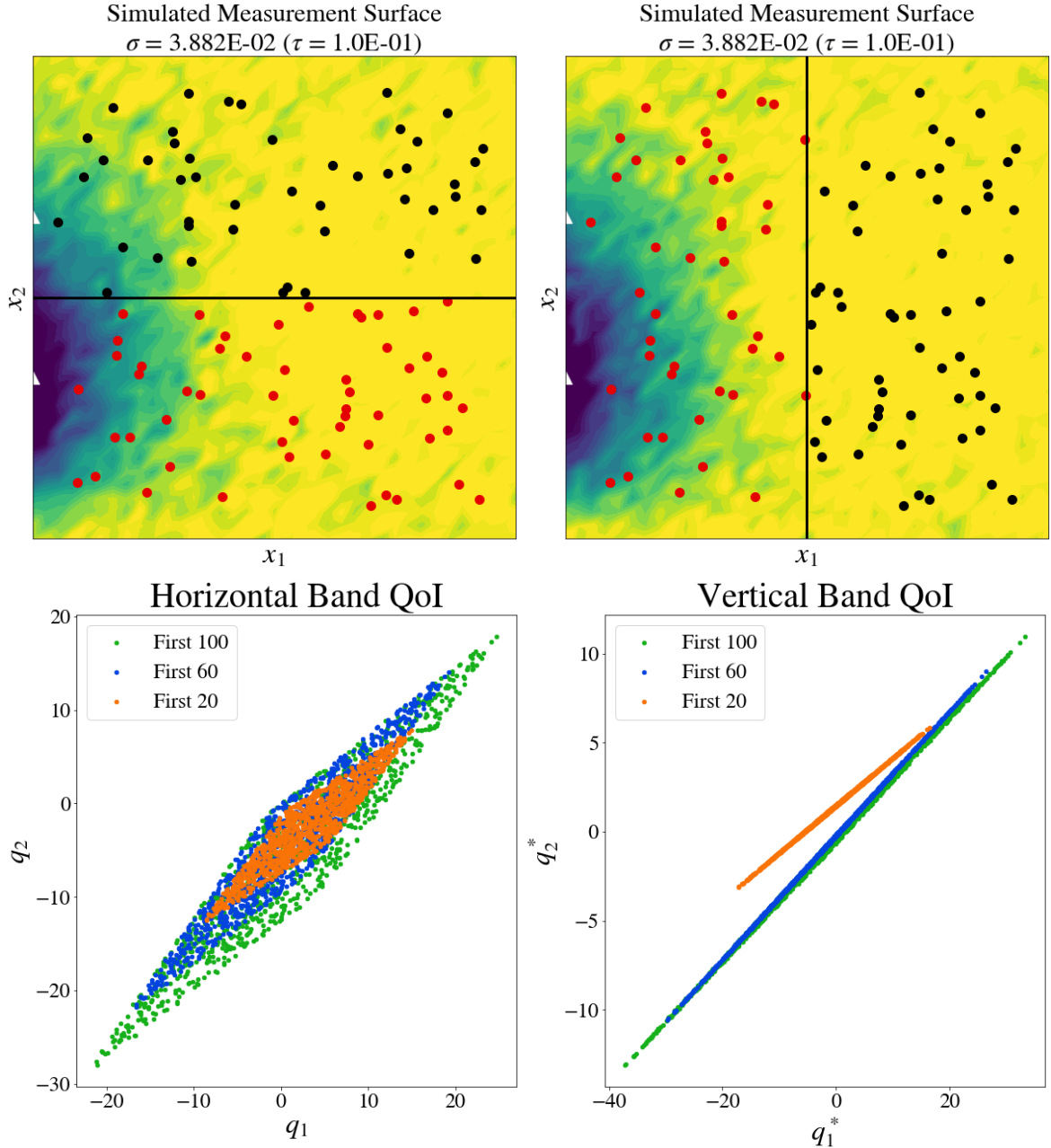


Figure 4.1: Comparison of Q_{2D} (left) and Q'_{2D} (right). Partitioning of Ω into the two components of each map is shown in the top half of the figure. In the bottom half, the vector-valued QoI map is constructed for all $N = 1000$ parameter evaluations using $D = 20, 60$, and 100 measurements, and the two resulting component vectors are plotted against one another for both methods of partitioning Ω .

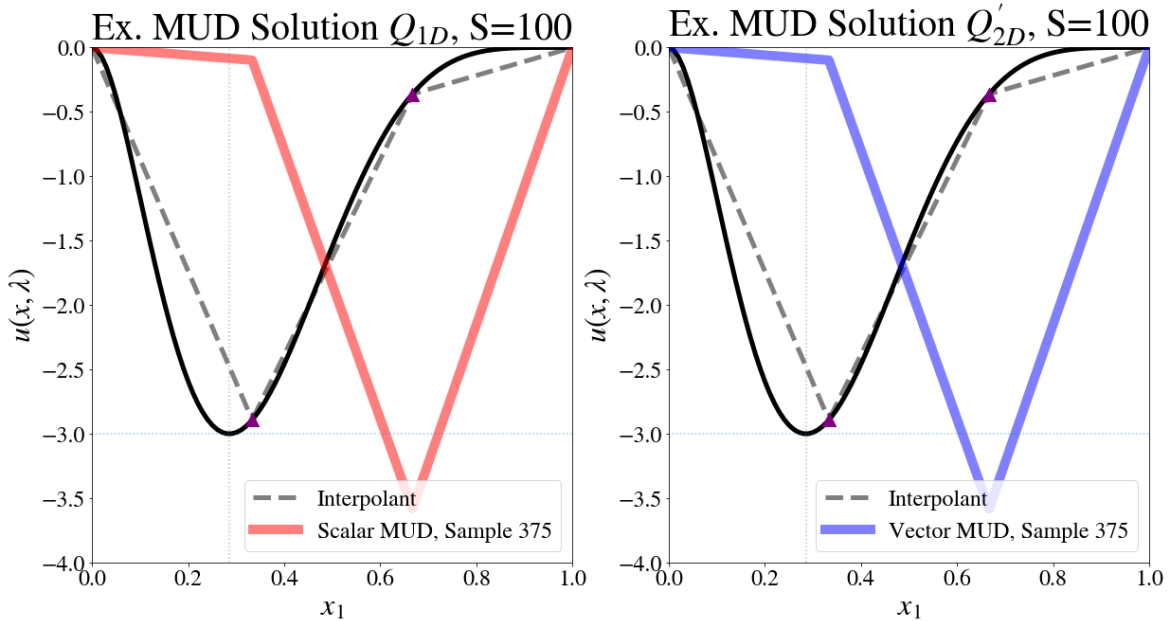


Figure 4.2: Side-by-side comparison of an example solution to the SIP using Q_{1D} (left) compared to using Q'_{2D} , juxtaposed against a plot of g .

for both QoI maps. This dilation is expected based on Corollary 2.3.1 where it is established (for linear maps), that the predictability assumption is satisfied once enough data are obtained.

Q'_{2D} has much higher skewness than Q_{2D} , as is visually evident by the near-perfect correlation between its component values seen in the right plot of Fig 4.1. The most notable difference between the scatterplots is the difference in diameters (reference the axis labels) for each data space, a fact attributable to the difference in skewness. The two component maps of Q'_{2D} contain almost the same information, so we can expect there to be little difference between MUD points arising from using Q'_{2D} when compared to using the scalar-valued map. We compare these two solutions for an instance of the SIP in Figure 4.2.

By contrast, the map induced by a horizontal split (bottom left of Fig. 4.1) provides new information in each component. While there is some correlation (the predicted data spaces are not rectangular), a far greater proportion of samples will fall within the practical support of the observed distribution, which qualifies them as possible solutions to the SIP. More information is learned with the inclusion of each component using this design than would be with the vertical split. Using a quantitative measure such as average skewness allows us to scale the assessment to higher-dimensional parameter and data spaces when visual inspection is not possible.

We focus attention on comparing higher-dimensional QoI maps constructed from aggregating data separated into more horizontal bands to scalar QoI maps (as proxies for highly-skewed maps), and note that a more thorough discussion of constructing QoI maps that induce desirable geometric properties is of

interest for future work. In 4.2 and 4.3, the “vector–valued” map will refer to the one with data aggregated into separate horizontal bands. We note that this design, while not guaranteeing optimality for precision or accuracy’s sake, respects the flow of information in the system being studied. Since the parameter represents the left Neumann boundary condition, information about its state flows from left to right in the horizontal direction.

4.2 Extension to Higher Dimensions

We now show that when the dimension of Λ is higher, the benefit from maximizing the dimension of the QoI map is even more considerable than what we observed in the two-dimensional cases, as long as we aggregate data into components of the QoI map in a purposeful manner. In the first example, we demonstrate the impact of increasing the volume of the parameter space while fixing all other attributes of the inverse problem. In the second example, we illustrate how we could utilize the solution to the SIP for the two-dimensional case from 2.4.2 to improve the MUD estimate in five dimensions.

4.2.1 A SIP with a Naive Initial Density

Consider a naive implementation in five dimensions, where the same prior knowledge on the bounds of g inform the choice of a parameter space. Suppose Λ is given by $[-4, 0]^5$, induced by five regularly-spaced knot points in the interior of $x_2 \in (0, 1)$ for which a uniform density is assumed in each component. In Figure 4.3, we show what one-thousand such initial functions look like, and note that many of them appear to exhibit fluctuating behavior which may require a finer mesh than the one being used to solve the problem (36×36) , in order to reduce numerical errors. This choice of initial density induces a lot of “conceptual” noise into the SIP, since “common sense” from a modeler’s perspective could rule out functions which zig-zag excessively.

We solve the SIP for both scalar– and vector–valued QoI maps. The latter is constructed with horizontal bands—which correspond to the partitioning of Ω into components of the QoI map—shown in the left of Figure 4.4. We refer to this map as Q_{5D} , and Q_{1D} will again represent the scalar–valued map. In the right half of Figure 4.4, the MUD solutions for Q_{5D} and Q_{1D} are shown in parameter space for a representative SIP. The scalar-valued MUD misidentifies the location of g ’s minimum value, but the vector-valued QoI is able to resolve the general qualitative behavior.

In Figure 4.5 we plot the results from twenty repeated trials (perturbations of noise) when using all 100 measurements. We observe, as before, the same difference in going from scalar– to vector–valued solutions that we saw in two dimensions in Fig. 2.6. In the left half of Figure 4.5, the scalar-valued QoI is unable to differentiate between resolving residual discrepancies in different locations in Ω . By contrast, the vector-valued QoI shown to the right is constructed with respect to the flow of information in the sys-

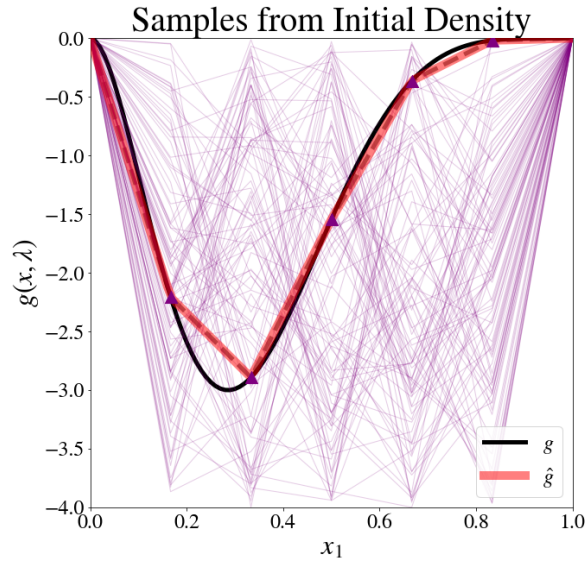


Figure 4.3: One thousand initial parameter samples (our model evaluation “bugdet”) were used to estimate g , constructed by taking independent uniform samples from $[-4, 0]$ for each direction are shown in purple.

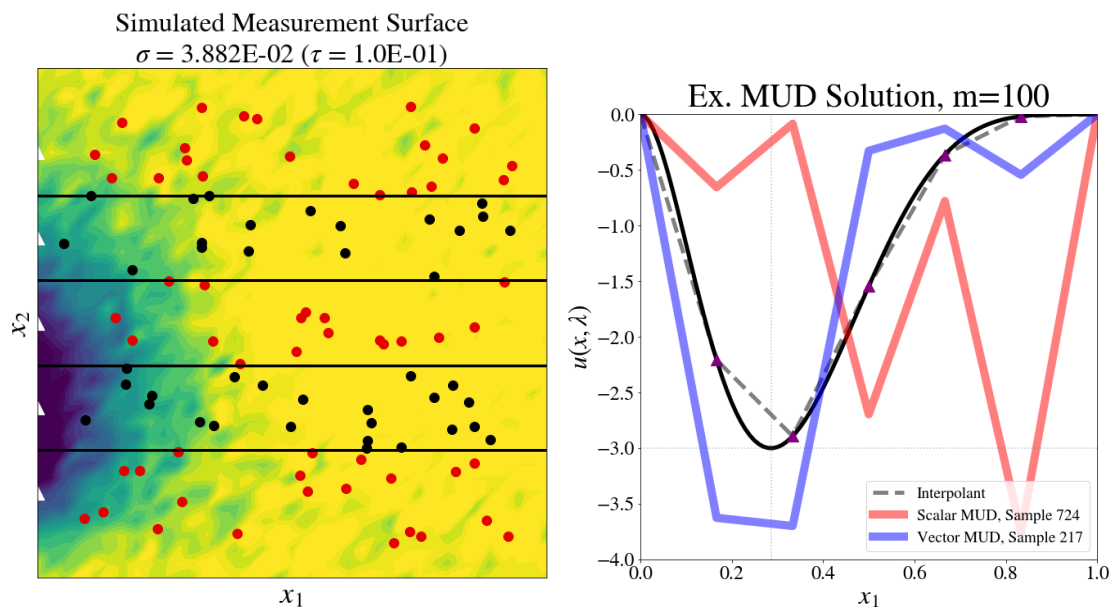


Figure 4.4: (Left): Layout for 5-D vector-valued map and comparison of the two MUD solutions in parameter space. (Right): Example MUD solutions for Q_{5D} and Q_{1D} .

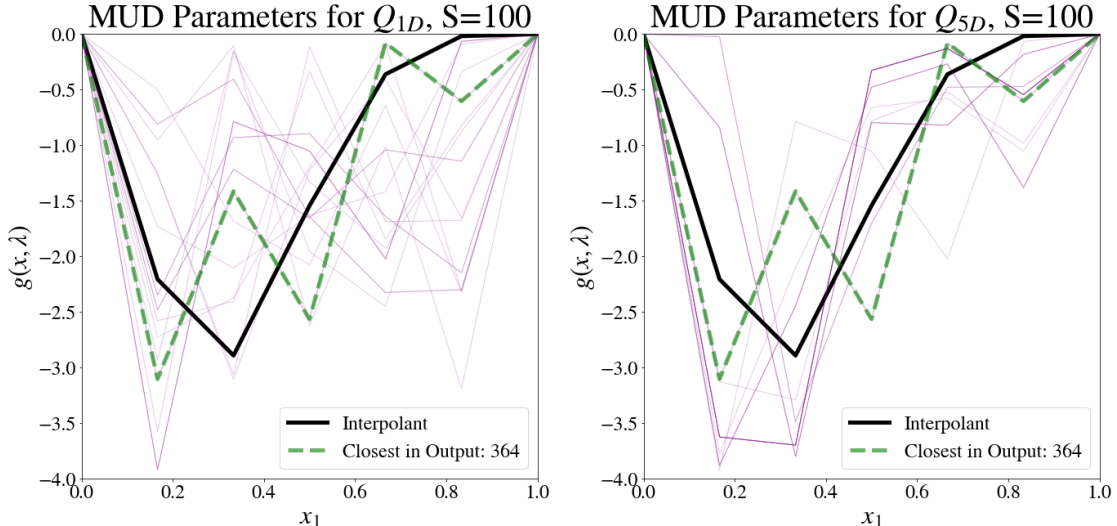


Figure 4.5: SIP solutions using Q_{5D} and Q_{1D} for twenty realizations of noise polluting the hundred measurements used to construct the map. (Left): Scalar-valued solutions. (Right): Vector-valued solutions.

tem, and so many more of the twenty trials land closer to the true minimum value of g . The solutions for the vector-valued approach instead explore the available knots (at $x_2 = 1/6$ and $1/3$), nearest the actual minimum value of $2/7$ instead, a much more valuable area of Λ to explore.

Recall from 2.4.2 that we previously solved a two-dimensional version of this problem. We leverage the effort involved in solving this first problem in order to better refine the approximation of g in 4.3 below. By using the former SIP solution results to define a much smaller region of Λ to explore, the results from the second SIP can improve considerably.

4.3 Improving Parameter Estimates by Solving Sequences of SIPs

When progressing from two dimensions to five in the process of refining our estimate of g , we did so using an equal amount of parameter samples despite the volume of the spaces differing. The measure of Λ (i.e., $\mu_\Lambda(\Lambda)$), increased by a factor of 64 while all else was held constant. Too many of the functions considered by the initial density are impractical to consider because of their roughness. In the linear examples of 2.2, it is shown that initial densities which ascribe higher likelihood to the true parameter lead to MUD estimates that are more accurate. By making better use of our model-evaluation budget of 1000 samples for the PDE example, we find that both Q_{1D} and Q_{5D} perform significantly better in their ability to resolve λ^\dagger .

4.3.1 Motivations for a New Initial Density

Reducing the volume of the support of the initial density will allow the samples drawn from it to better predict the collected data. Recall from Example 2.4.2 that two maps are used to solve the SIP:

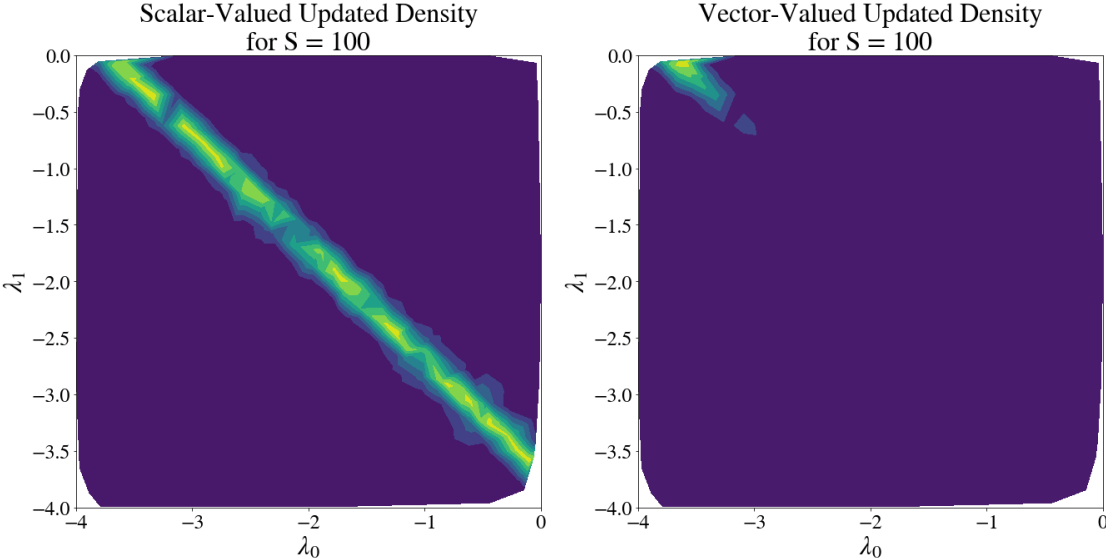


Figure 4.6: 100 measurements are used to solve the SIP for the PDE problem with Q_{1D} and Q_{2D} .

Q_{1D} and Q_{2D} and MUD points are shown for representative examples. We use the solutions from those examples—namely the ratio which updates the initial density—to inform the construction of a new initial density in five dimensions. In Figure 4.6, we plot the initial densities associated with Q_{1D} and Q_{2D} and remark that the scalar-valued QoI map identifies a contour which appears to trace a straight line through Λ . This is helpful for identifying the correlation structure and defining a lower-dimensional subspace to perform rejection sampling. However, the solution that comes from using Q_{2D} is better at reducing uncertainty. Taken together, these observations suggest a number of sampling strategies to generate a new initial density.

By considering the relationship between the parameters and the types of functions that are possible given the solution to a 2-D inverse problem, we are able to create a more restricted parameter space in five dimensions.

For a detailed discussion of how a new initial density is constructed for this example, we refer the interested reader to Appendix C. We summarize the procedure briefly: First we generate uniform i.i.d. samples in the three dimensions associated with the new knot points by defining independent bounds for each and taking samples from the cross-product of the directions.⁴ We generate $N = 1000$ i.i.d. samples from this 2-D uniform density⁵, and join them with the three other directions to form the new initial sample set, the functions from which generate the curves shown in Figure 4.7.

⁴The bounds for each are determined by looking at piecewise-linear estimates of g that come from sampling the updated density for the vector-valued solution.

⁵The (computational) cover is described by a procedure which involves the SVD of samples from the scalar-valued solutions in order to capture the correlation structure. The use of the Q_{1D} solution is due

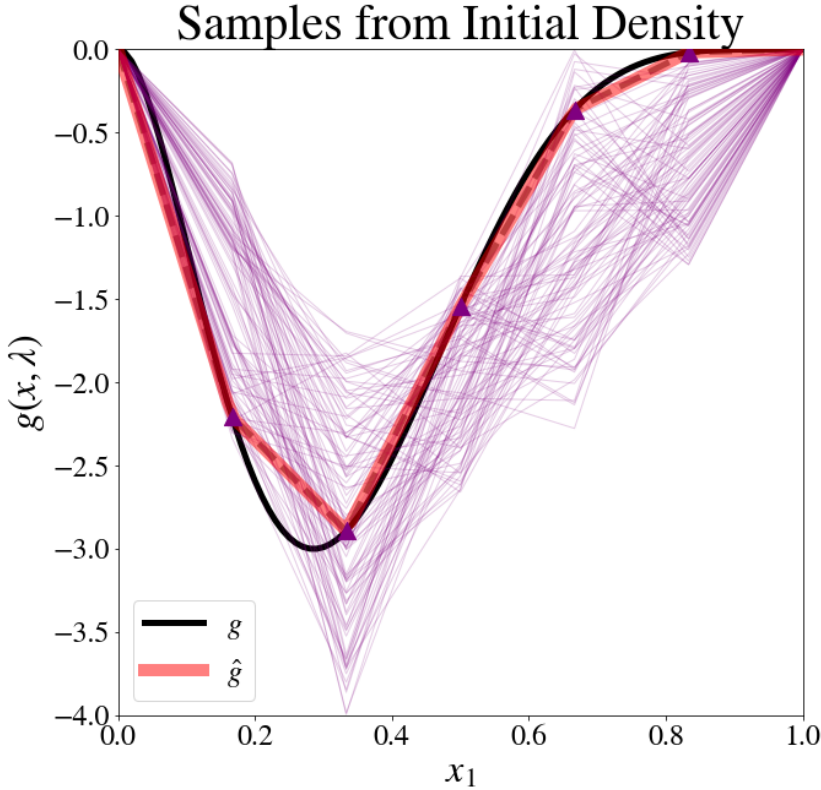


Figure 4.7: Initial density constructed for the second attempt at the five-dimensional inverse problem, with the structure of solutions learned from the 2-D example incorporated into the selection of bounds in each direction.

The new initial curves in 4.7—especially when contrasted to those in Fig. 4.3—represent a far more reasonable set of possibilities. The slope of the functions considered now all only have a single sign change, a marked improvement over the two or three that many samples from 4.3 exhibited. We note that such considerations of smoothness could be avoided by parameterizing g with a basis of some sort, but that problem is beyond the scope of this work.

4.3.2 SIP Solutions using New Initial Density

We now come to the solutions that arise from solving the same five-dimensional inverse problem of interpolating the values of g through equispaced knot points, with both types of maps, in Figure 4.8. The difference in comparison to the solutions in Fig. 4.5 is stark: no longer are the estimated functions dramatically under-estimating the local minimum of g . The inadequacy of approximation error is attributable to the choice of knot points imposing a regular structure. Since g 's minimum lies between two knot points, the best approximation of where this minimum is will by definition still be incorrect.

to the paucity of samples accepted from the vector-valued solution. The structure of the latter updated density is more amenable to form a good estimate of this correlation direction in parameter space.

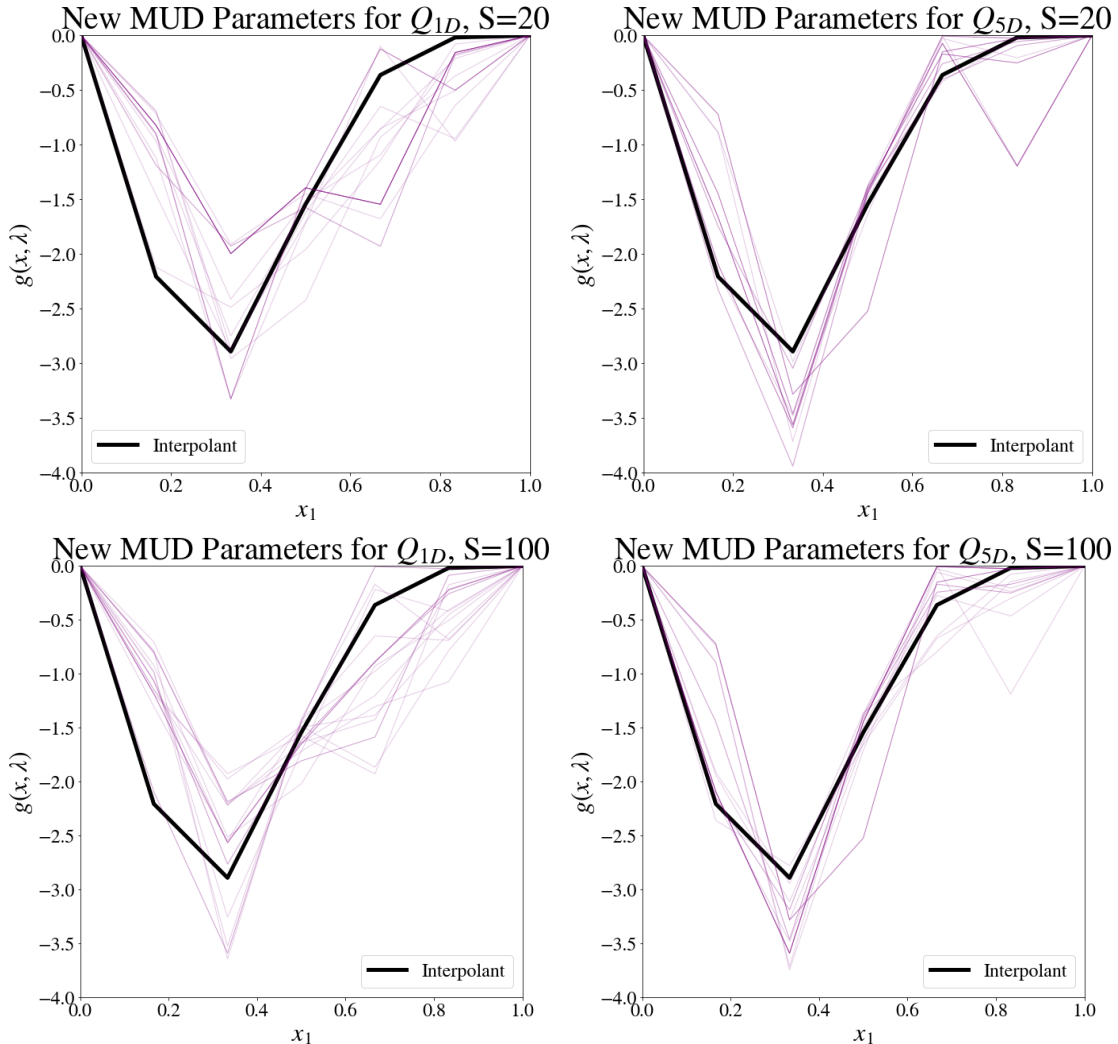


Figure 4.8: Solutions to the SIP using one hundred measurements for $D = 20$ (top) and 100 (bottom). (Left): Scalar-valued solutions for alternative approach to the five-dimensional problem. (Right): Vector-valued solutions.

Even when only 20 measurements are incorporated into constructing the QoI maps, there is a considerable improvement in the predicted boundary conditions when using a better initial density, as seen by comparing the solutions in Fig. 4.8 to Fig. 4.5. Owing to the reduced volume of support for the initial density, both QoI maps resolve the residuals similarly, especially as more data are incorporated (shown in the bottom of 4.8). Since “unreasonable” functions are no longer being considered, both maps produce qualitatively similar estimates.

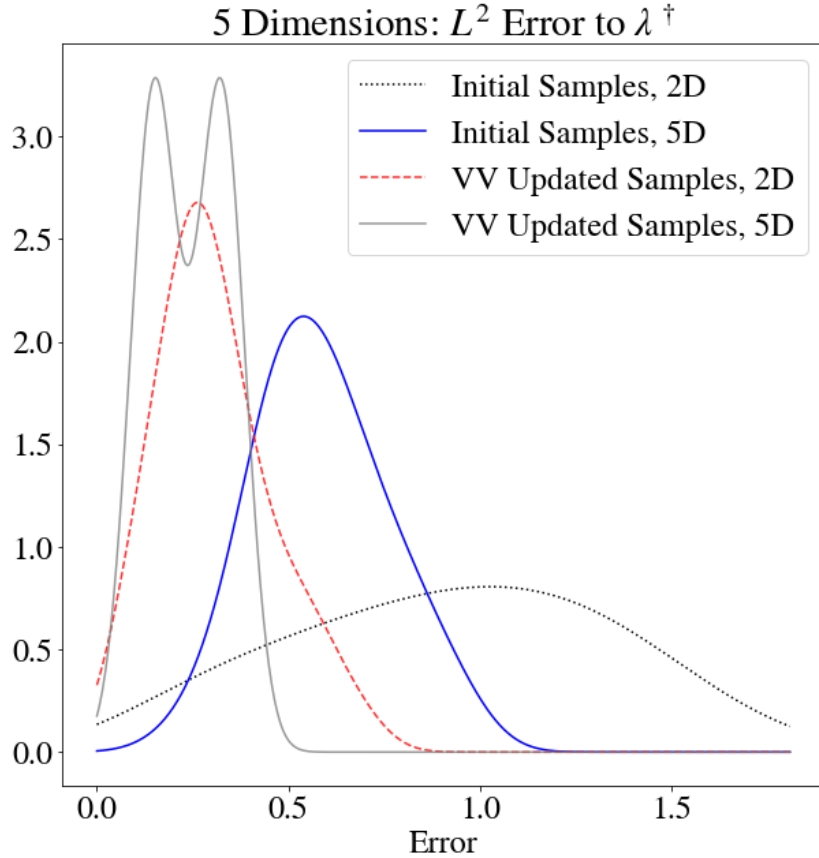


Figure 4.9: Comparison of the 2D initial errors to the 5D ones, as well as the reduction of uncertainty that solving a SIP problem for each provides.

4.3.3 Demonstration of Reduction in Uncertainty

As a final note on this experiment, we contrast the resulting L^2 -errors to g^6 of these MUD solutions, to the previous two examples in Figure 4.9. With each successive problem, our uncertainty is reduced and the MUD solutions have lower variance and improved accuracy. Note that they appear to be moving towards a value away from zero, which represents a fixed bias (five equispaced knots can only approximate this particular g so well).

4.4 Conclusions

We have shown that when posing and solving SIPs, we are motivated to choose data-constructed QoI maps which have (a) as many components as possible (up to the dimension of Λ), and (b) whose components exhibit high-degrees of mutually geometrically distinct information (i.e., low average skewness). There is a dramatic reduction in the sensitivity to the measurement noise when the same hundred measurements are used to construct a map with lower skewness. In the next chapter, we discuss some other

⁶derived from computational approximation with the trapezoidal rule

considerations for constructing SIPs, including measurement precision and placement. We show how different experimental setups can lead to parameter estimates which exhibit different levels of accuracy and precision. We also introduce a novel method for leveraging the results shown here in a sequential manner to gain possible computational efficiency.

CHAPTER V

CONCLUSIONS, FUTURE WORK, AND PRELIMINARY RESULTS

5.1 Concluding Remarks

In the Chapter II we demonstrate that the MUD solution retains the accuracy of least-squares solutions while simultaneously offering the flexibility of specifying initial beliefs. Normally in order to incorporate such beliefs, practitioners in the machine-learning field would perform Tikhonov regularization, usually with the inclusion of a hyper-parameter which scales the additional parameter-space norm in the objective function. Mathematically, this scaling factor applied to the norm is equivalent to scaling the matrix representation of an initial (prior) covariance and searching for the MAP point of a Bayesian posterior. Increasing this scaling factor is interpreted as having less confidence in these initial assumptions. Conversely, decreasing it is equivalent to putting more emphasis on the prior beliefs than the evidence provided by the data, which causes MAP solutions to drift away from the solution contour (equivalence class) to which λ^\dagger belongs.

The MUD point is not impacted by scaling of the initial covariance, providing *consistent* solutions which demonstrate levels of accuracy that MAP points only exhibit for larger values of scaling factors. Not only is it robust to the specification of prior assumptions, but it manages to offer the flexibility of such specifications without paying the additional cost of hyper-parameter optimization that would be required for the Tikhonov solution to achieve comparable results; any choice of α would have sufficed.

By contrast, the Tikhonov-regularized solution selects a point that is biased in directions defined by the initial density (covariance). The data-consistent solution is an update to the initial mean in this same direction but will always exist on the contour $Q^{-1}(\mathbf{y})$, where \mathbf{y} is the mean of the observed density.

We also show that regardless of how well-informed the initial beliefs are, the convergence rate of the MUD solutions as more data are incorporated—either by dimension or rank)—will match those of the Least-Squares solutions. Moreover, unlike MAP solutions, the MUD point is not sensitive to scaling of the initial covariance (how strongly initial beliefs are held). This insensitivity provides a strong motivating factor for the consideration of the data-consistent approach within the standard set of solution methods available to scientists and modelers who seek to perform parameter-identification. We leave the investigation of more connections to the removal of hyper-parameter estimation to future work.

The trouble is, none of these regularization approaches actually guarantee that in under-determined problems, the unique solutions that are selected are close to λ^\dagger . The equivalence-class nature of the solution contour means that by definition there are directions in which uncertainty is unresolved. Thus, the goal is to aggregate data into components of a vector-valued QoI map to improve estimates of λ^\dagger across

more dimensions. We use skewness as a guide for constructing the QoI and demonstrate its utility in improving estimates to a λ^\dagger related to estimating an uncertain function.

5.2 Future Work and Preliminary Results

5.2.1 Optimal Experimental Design Considerations

In this section we return to the nonlinear examples presented in the previous chapter and address some choices made in how the experiment was performed. By revisiting the examples, we demonstrate that the decisions made regarding measurement equipment and/or location have an impact on the reduction of uncertainty and accuracy of the MUD point. Furthermore, we show that the choices made in the experimental design of previous examples are made for reasons of convenience of exposition. Changing these assumptions does not alter the viability of the MUD point as an alternative estimator for use parameter identification problems. We study the impact of more precise measurement devices on the convergence rates for the parameter estimates in Appendix B for the problem in 2.4.1 of estimating the rate of exponential decay. To complement these results, we show them alongside ones generated with equipment that measures at twice the temporal frequency.

In Section 5.2.2, we also highlight how an awareness of another geometric property of QoI maps—relating to their sensitivity with respect to λ —can help improve the accuracy of the MUD estimate. By placing sensors in locations which exhibit greater sensitivity to the parameter for which the SIP is solved, experimenters can achieve a considerable improvement in the precision of estimating λ^\dagger with an equal number of measurements collected. A similar complementary problem is solved where information about the sensitivity of measurement locations is used to inform improved placement of a hundred sensors. In this example, we walk through the sorts of analyses a modeler might conduct in order to select an experimental design through simulation and show a significant improvement in the accuracy of the MUD point.

5.2.2 Elliptic PDE Example

We make a slight modification to the Poisson problem from 2.4.2 to make it into a one-dimensional parameter identification problem. This choice is primarily motivated by the goal of using visual aids to demonstrate slopes corresponding to different measurement locations. We briefly summarize the experimental set-up again for the reader’s convenience. Consider the following Poisson problem defined on a unit

domain Ω :

$$\left\{ \begin{array}{ll} -\nabla \cdot \nabla u &= f \quad \text{on } \Omega \\ u &= 0 \quad \text{on } \Gamma_T \cup \Gamma_B \\ \frac{\partial u}{\partial \mathbf{n}} &= g(x, \lambda) \quad \text{on } \Gamma_L \\ \frac{\partial u}{\partial \mathbf{n}} &= 0 \quad \text{on } \Gamma_R \end{array} \right. \quad (5.2.1)$$

where $(x_1, x_2) \in \Omega = (0, 1)^2$, Γ_T is the top, Γ_B is the bottom, Γ_L and Γ_R left and right, respectively. $\frac{\partial u}{\partial \mathbf{n}}$ denotes the outward normal direction. We select g as before in 2.4.2, and show the response surface for λ^\dagger in the left of Figure 5.1, with darker colors representing more negative values. Now, g will be parameterized by a scalar instead of a vector, representing the leading coefficient in the polynomial. In other words, we presume knowledge of the structure of g but not its exact values. The initial density is again chosen to be uniform over the interval $\Lambda = (-4, 0)$, and f is chosen to be $10 \exp\{-\frac{(x_1 - 0.5)^2 + (x_2 - 0.5)^2}{0.02}\}$.

We demonstrate the impact of incorporating more measurements on the ability to estimate λ^\dagger . In Walsh (2017), the geometric quantity known as *scaling* inherent to QoI maps is studied with respect to its impact on the precision of solutions to SIPs. This property corresponds to the average local linear response of the QoI map with respect to changes in λ . In short, if a QoI map (such as one induced by a single measurement), exhibits larger slopes on average over Λ , then it has greater scaling and by implication, more predictive precision. We demonstrate how an awareness of the QoI's scaling can inform the construction of a more optimal QoI map by way of better selecting the locations of measurement devices. Here, the assessment of a map's average scaling is identified heuristically through visual inspection of slopes. Such a graphical comparison of QoI maps can be done without prior knowledge of the scaling property and is not outside the scope of analysis that could be performed during initial investigation into an inverse problem.

5.2.2.1 Uninformed Sensor Placement

First we show that using the sensor-placement strategy introduced in 2.4.2 results in many locations that provide little information to reduce uncertainty in the parameter space. We consider a selection of $S = 1000$ measurement locations in the interior of the response surface chosen by sampling a uniform density over the set $(0.05, 0.95)^2 \subset \Omega$. We show only the first 100 measurement locations in plots for visual clarity. In the rightmost histogram of Figure 5.1, we plot the data generated by each simulated sensor location, and note that many values are near zero as a result of being near boundaries or the right-side of Ω .

The measurement response as a function of λ is plotted next to it in the center of 5.1, and suggests that the sensors each exhibit linear responses to changes in the parameter. This observation can be

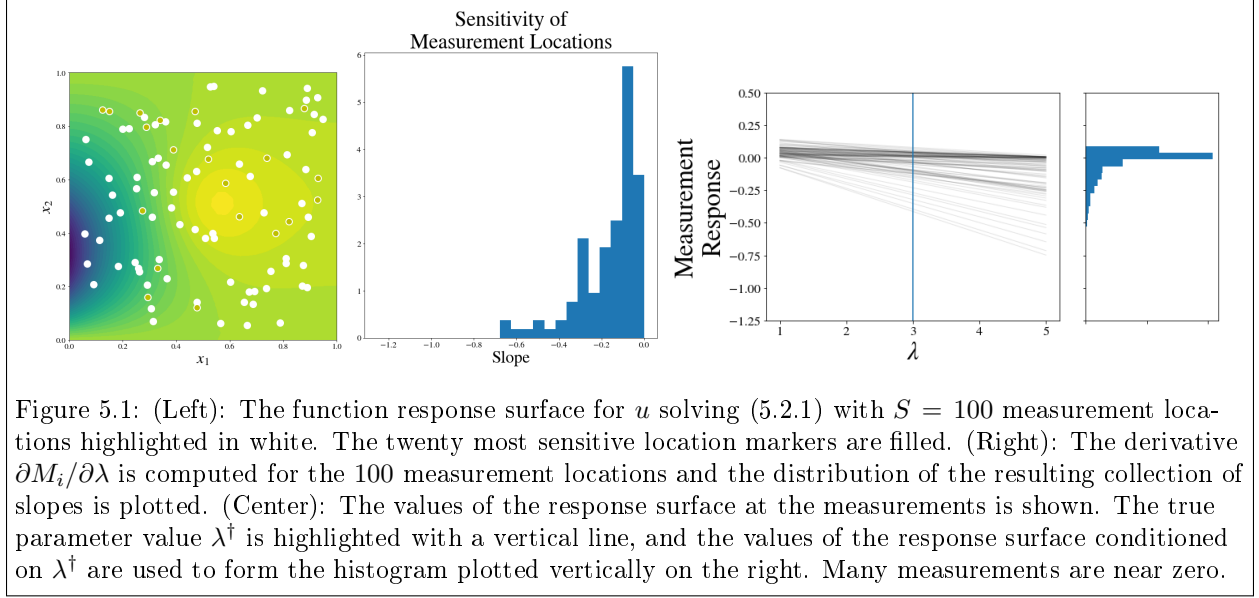


Figure 5.1: (Left): The function response surface for u solving (5.2.1) with $S = 100$ measurement locations highlighted in white. The twenty most sensitive location markers are filled. (Right): The derivative $\partial M_i / \partial \lambda$ is computed for the 100 measurement locations and the distribution of the resulting collection of slopes is plotted. (Center): The values of the response surface at the measurements is shown. The true parameter value λ^* is highlighted with a vertical line, and the values of the response surface conditioned on λ^* are used to form the histogram plotted vertically on the right. Many measurements are near zero.

used to visually identify that some measurements are more sensitive than others since the lines from certain sensors have steeper slopes than the majority of locations. The majority of measurements exhibit almost no sensitivity to changes in λ , visually represented by the density of nearly horizontal lines (slopes of zero). However, some of the sensors have steep slopes, which suggests higher sensitivity to changes in λ . To quantify the variability in the slopes across different sensor locations, we use the smallest and largest samples values of $(\lambda, u(\lambda))$ to make a global linear estimate of each one's slope. We plot the distribution associated with the collection of these slopes in the center histogram of 5.1.

5.2.2.2 Informed Sensor Placement

Instead of placing sensors throughout the square interior of Ω given by $(0.05, 0.95)^2$, we consider how the convergence results would compare if the subdomain for sensors was better selected. In the left panel of Figure 5.1, the most sensitive measurements are highlighted and appear near the left boundary. Furthermore, the response surface exhibits horizontal symmetry, so we restrict locations to the bottom half of Ω . These two observations can inform a new bounding box for consideration of where measurements should be taken. We perform the same experiment for sensors placed in $(0.05, 0.25) \times (0.05, 0.5)$ (measurement locations drawn from a uniform distribution over this region), and refer to this as the *alternative* experimental design. The first 100 of the 1000 sensor locations sampled is shown in the left panel of 5.2 and we remark that the most sensitive ones (highlighted) cluster near the center of the left boundary, where the response surface is most negative.

For this alternative design, we show the sensitivity of sensors in the center of 5.2 and note that there are fewer sensors which exhibit low sensitivity to changes in λ^* in contrast to 5.1. The slopes are

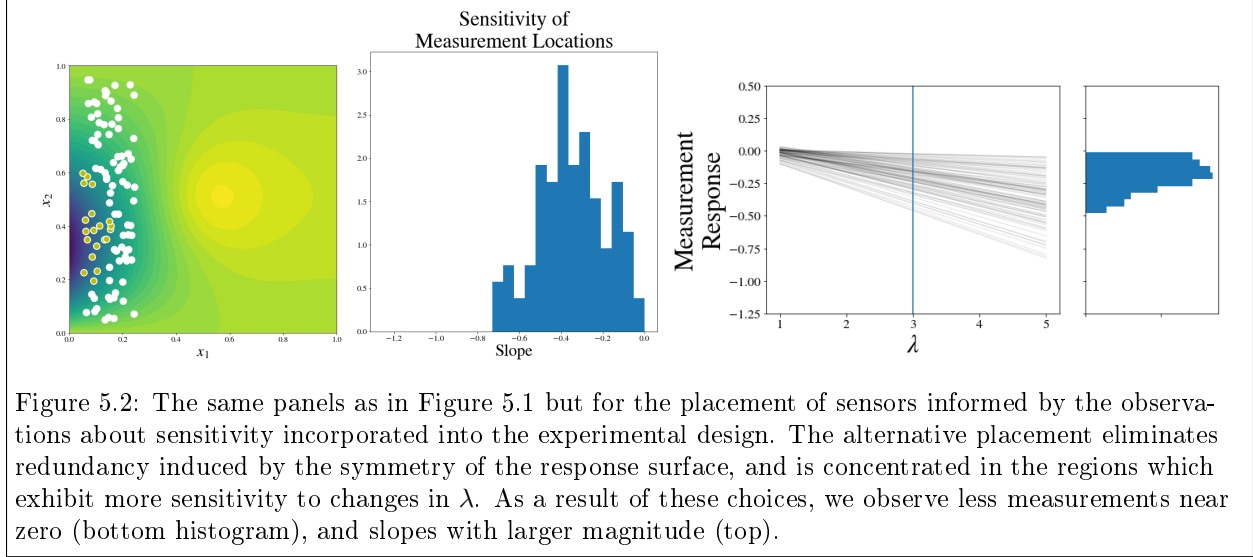


Figure 5.2: The same panels as in Figure 5.1 but for the placement of sensors informed by the observations about sensitivity incorporated into the experimental design. The alternative placement eliminates redundancy induced by the symmetry of the response surface, and is concentrated in the regions which exhibit more sensitivity to changes in λ . As a result of these choices, we observe less measurements near zero (bottom histogram), and slopes with larger magnitude (top).

again shown in the center of the figure and exhibit a bimodal distribution with a larger portion of the measurements having slopes with magnitude 4-6 times greater than the mode in the center of 5.1. There are also less measurements which take values near zero as well, shown in the rightmost panel of the figures. The original design exhibited a strong decay in its distribution of measurement values, while the alternative design results in a much more symmetric distribution.

5.2.2.3 Comparison of SIP Solutions with Different QoI Maps

We are interested in knowing how the uncertainty around the parameter estimate (the MUD point) changes as we incorporate more (noisy) data. To generate convergence plots, we solve the problem repeatedly for $S = 10, 50, 100, 250, 500$, and 1000 and take the mean and variance of the twenty trials for each value of S . Consider the convergence plots in Figure 5.3, which demonstrates the impact of increasing S on our ability to resolve λ^\dagger .

We show the mean absolute error in the left half of Figure 5.3 and remark that two decimal places of accuracy can be achieved with approximately 250 measurements instead of the 1000 required in the left-half.

The convergence results for the original experimental design demonstrate that even randomly placed sensors in the interior of Ω are suitable for parameter estimation. However, when we considered sensors that are placed with knowledge about the physical system being studied, more information is learned from the measurement equipment by placing sensors in different locations. Using the alternative experimental design, we see a reduction of uncertainty in the panels of Figure 5.3, represented by the persistent vertical displacement between the regression lines for convergence.

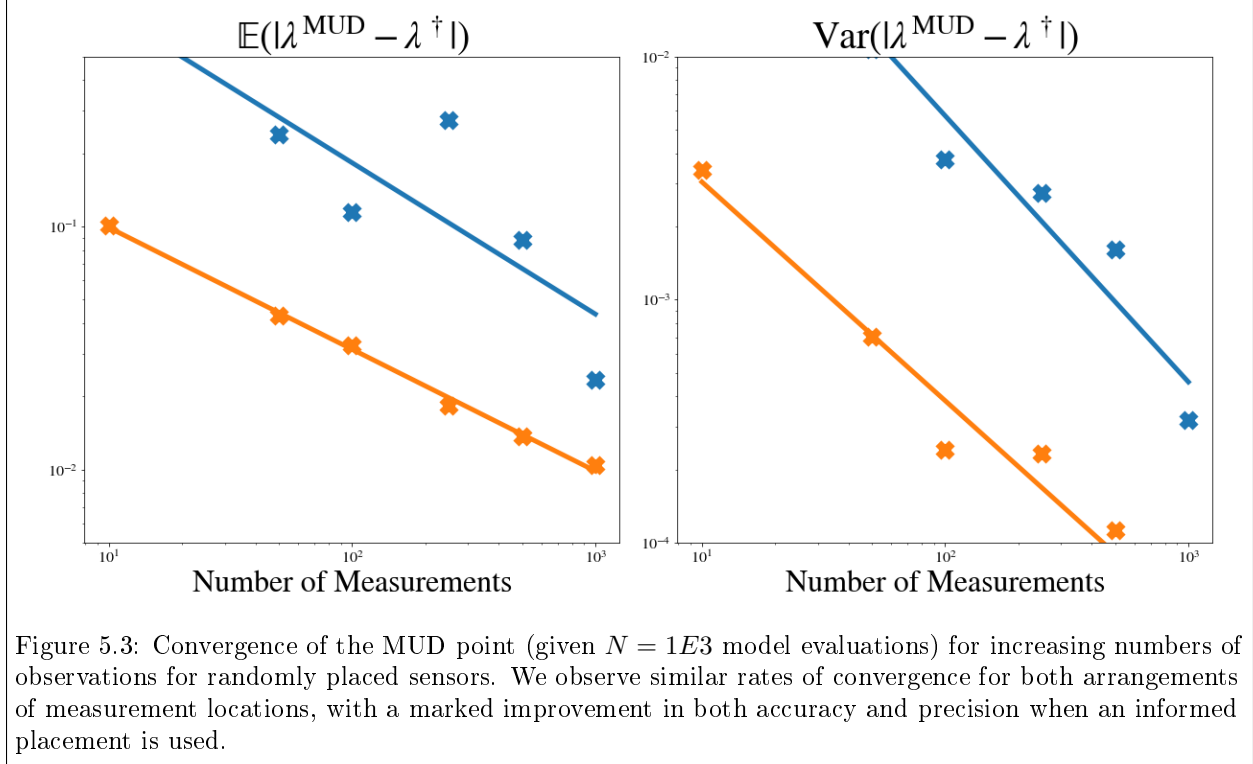


Figure 5.3: Convergence of the MUD point (given $N = 1E3$ model evaluations) for increasing numbers of observations for randomly placed sensors. We observe similar rates of convergence for both arrangements of measurement locations, with a marked improvement in both accuracy and precision when an informed placement is used.

5.3 Sequential Inversion

The DCI framework relies on evaluating the ratio function $r(\lambda)$ in D -dimensional QoI space, so we turn our attention to addressing the challenges associated with the growth of this space. As D increases, we must approximate a push-forward distribution with perhaps a fixed number of samples (from model evaluations) N , which represents a considerable source of error since the convergence rate for kernel density estimation with Gaussian kernels is $\mathcal{O}(N^{2+D})$.

For example, consider a time-dependent problem for which hundreds of spatial sensors are providing streams of data. Approximating a 100-dimensional space with $N = 1E3$ or $1E4$ samples (as we have been using for demonstrations), poses a problem for any density approximation method. However, either of these values for N are generally sufficient to estimate a one-dimensional distribution. In some sense, approximating a QoI at each location over time is reasonable, but doing so for all of them simultaneously is not. To this end, we propose an approach to solving the parameter estimation problem by performing inversion through a sequence of scalar-valued QoIs rather than employ a vector-valued approach.

Any choice of dimension below D would suffice, but this sequential-scalar-valued approach provides a starting place and admits a simplicity in exposition. By choosing a dimension of one, the focus of the examples is restricted to solely the order in which the QoIs are inverted; it avoids the additional complexity of enumerating the combinations of QoI when dimensions can vary. We also choose to use a linear

map for convenience so that we can use the analytical solutions presented in Chapter II without concern for approximation error. Furthermore, we omit measurement error from polluting the observations so that all the inverse contours intersect at a point. In the event that there is measurement error, each contour will be displaced, so the collection of contours will form a convex hull whose volume is proportional to the approximation error. By omitting measurement error, we simulate scalar-valued QoI which are constructed with sufficient number of measurements so as to ameliorate the impact of misidentifying each contour's location in Λ .

With each iteration in the sequence of inverse problems, we explain measurements that constitute a single QoI at the expense of accuracy in others. By contrast, the vector-valued approach seeks accuracy in all of the directions of observations simultaneously. This trade off is all about efficiency, since 1-dimensional problems are computationally “cheap,” we can iterate through many more of them for the same computational cost. By the time we finish iterating through all available QoI, the estimate obtained from $Q^{(1)}$ may have drifted significantly away from its solution contour through the sequence of inverting through $Q^{(1)}, Q^{(2)}, \dots, Q^{(100)}$. To address this, we perform multiple passes through the set of QoI. Borrowing from other sequential algorithms, these “epochs” will allow us to iterate until the solution stops changing by some predefined relative threshold, representing a lack of “learning” through continued effort.

5.3.1 Motivating Linear Example

We study the following motivating two-dimensional example with QoI defined by 10 equispaced rotations of the unit vector $[0, 1]$ through the first two Euclidean quadrants. We first plot the result of a single epoch in the left panel of Fig. 5.4.

The spiral shape is a result of the underlying geometry of this QoI map defined by rotations. The successive rows are so similar to each other that very little is “learned” between each iteration; the projection doesn’t cover a large distance in Λ . At the end of these epochs, the estimate in the right panel of 5.4 is still far off from the true parameter value (the intersection of the contours).

To further underscore the lack of mutually distinct information in successive rows of the QoI, we choose two pairs of indices from among the ten available in order to define two QoI maps, the contours for which we plot in different colors in Fig. 5.5. We solve a total of ten 1-D inverse problems for each of them (five epochs) to match the budget of the previous example in the left panel of 5.4 (with ten maps and one epoch).

We observe that in Fig 5.5, that there is much greater accuracy in estimating the true parameter value than in the case of Fig 5.4. The reason for this difference is that there is more mutually distinct in-

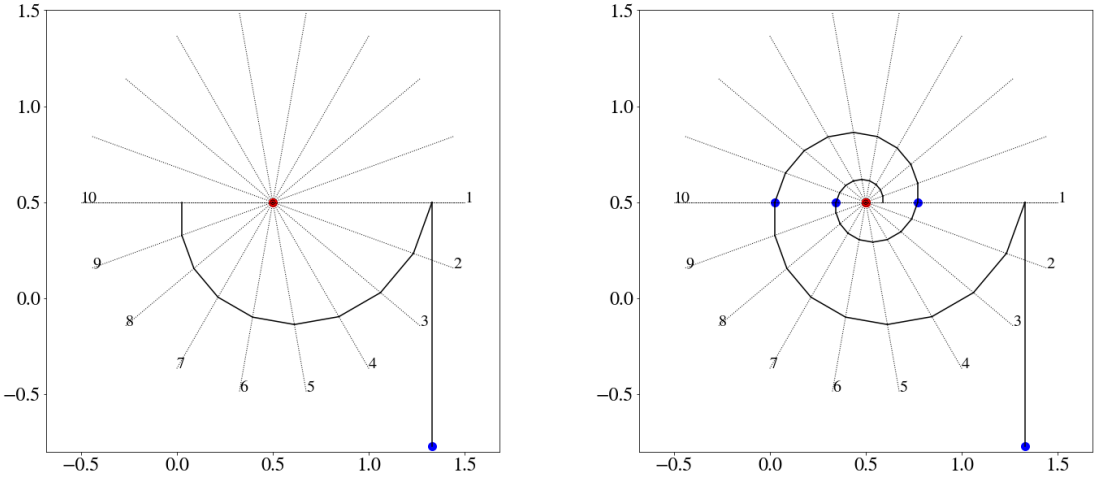


Figure 5.4: Dotted lines show the solution contours for each row of the operator A . (Left): First epoch for iterating through 10 QoI. (Right): Three more epochs allows our estimate to get much closer to the true value.

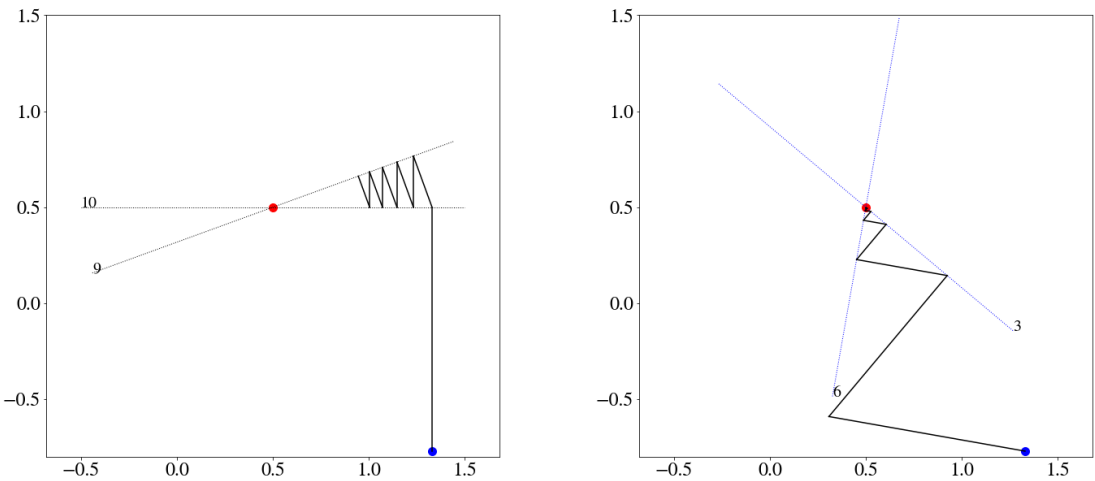


Figure 5.5: Iterating through five epochs of two QoI, each formed by picking two of the ten available rows of A at random. The random directions chosen on the left exhibit more redundancy than those on the right, so the same amount of iteration results in less accuracy.

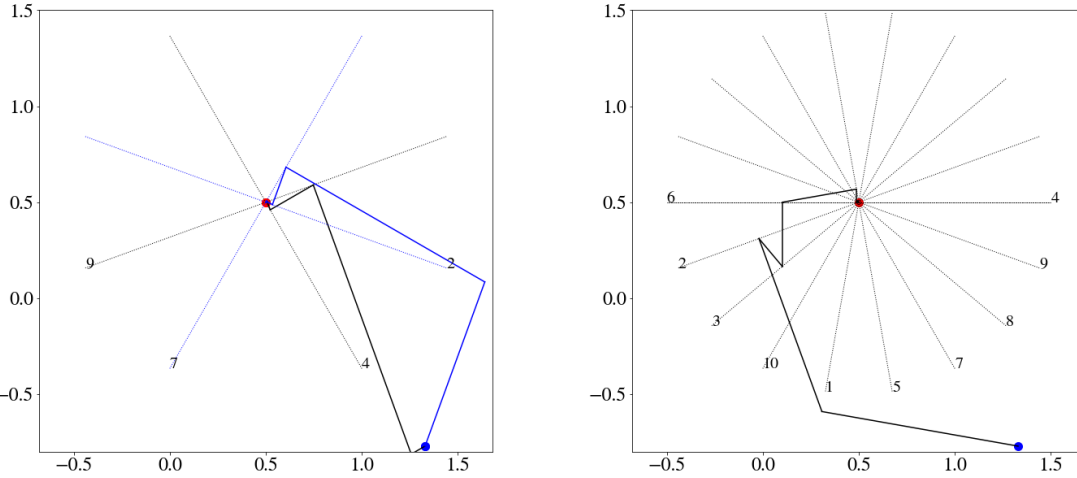


Figure 5.6: (Left): Iterating through a single epoch with a QoI formed by picking rows of A which exhibit mutual orthogonality. (Right): Iterating through the rows of A at a random order for a single epoch results in considerably more accuracy than doing so in the original order of rows of A .

formation between successive iterations of a pair of random rows of A than there is between adjacent rows, as measured by the angle between the solution contours.

5.3.2 Connection to Skewness

If we are careful with how we construct maps or choose an iteration strategy, we can achieve considerably more accurate solutions with the same computational cost. Had the choice of QoI components corresponded to a pair of rows that were orthogonal, the initial mean would converge to the reference value in a single epoch (two iterations), since there is no redundancy in information whatsoever. This is equivalent to saying that we have an incentive to select rows that induce a QoI map with unit skewness.

We show this in the left half of Figure 5.6 for two QoI maps with orthogonal pairs of components. If instead no a priori analysis of the rows of A and iteration through the available QoI at random is the chosen ordering, more accuracy is achieved with only ten iterations. We show this in the right-half of Figure 5.6, which exhibits a more accurate estimate compared to 5.4 at the same computational cost.

5.3.3 Comparisons and Convergence Results

To make these results more concrete, we propose the following example: We limit ourselves to solving 100 inverse problems (i.e. up to ten epochs for this map), with the *only* difference between approaches being the order in which the rows of A are used. First, we use the QoI as they are presented: in order with respect to increased rotation angle (which defines the rows of A). Next, we shuffle the rows of

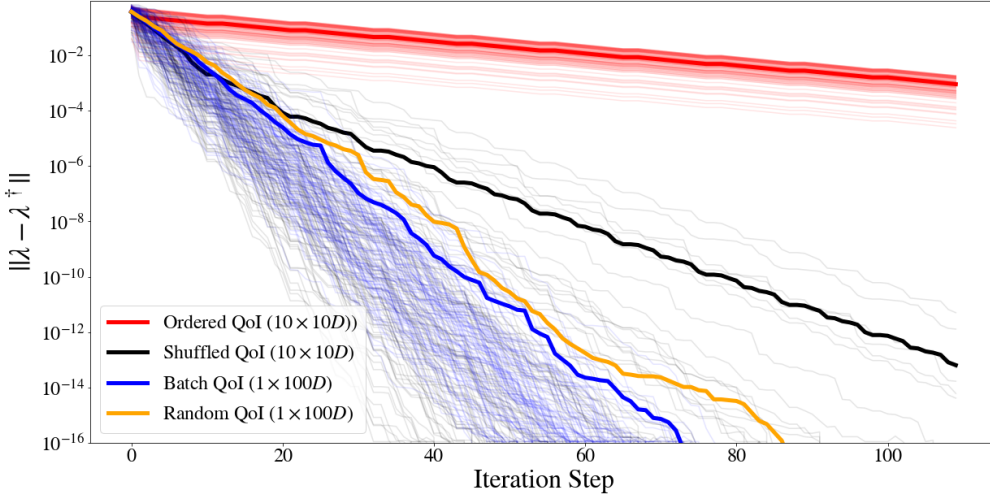


Figure 5.7: Twenty different initial means are chosen and iterated on for three approaches. Individual experiments are transparent and the mean error is shown as solid lines. In the *Ordered* approach, we iterate through the rows of A as they are given to us for ten epochs. *Shuffled QoI* refers to establishing a different random ordering of the rows of A for each trial, and then using this ordering for ten epochs. Finally, in the *Random QoI* approach, we choose a QoI at random for each of 100 iterations, where the ordering still ensures each row gets used ten times, representing the same overall set of inverse problems solved as the other two.

A and then perform ten epochs using this permuted map. Lastly, we create an ordering based on a random shuffling of ten sets of indices representing the rows of A . The latter approach is similar to the second in that the same problems are solved the same number of times overall, but it lifts the restriction that a row must only be used once in each successive set of ten iterations (equal computational effort).

In Figure 5.7, it is shown that using the rows of A sequentially performs very poorly (the error struggles to get past a single decimal place of accuracy), which aligns with “spiraling” seen in Figure 5.4 where the first few epochs are plotted. Shuffling the rows but requiring that every tenth iteration to use the same row (i.e., ensure same ordering for each epoch), leads to a considerable improvement by which sixteen decimal places of accuracy are achieved in under 100 iterations. In a few instances, the shuffled approach stumbles on an ordering that accelerates convergence, likely due to orthogonal pairs of rows in the shuffled order. These cases exhibit the kind of behavior seen in the left panel of Fig 5.6; in other words, sometimes random shuffling finds the “smart” rows to iterate through. Since the ordering has no dependence on iteration number in the approach where we use random rows, we have more opportunities to find these successive orthogonal pairings, and so we see that on average, it takes fewer iterations to achieve the same accuracy.

REFERENCES

- Alexanderian A, Petra N, Stadler G, Ghattas O (2014). “A-optimal design of experiments for infinite-dimensional Bayesian linear inverse problems with regularized ℓ_0 -sparsification.” *SIAM Journal on Scientific Computing*, **36**(5), A2122–A2148. doi:10.1137/130933381.
- Allmaras M, Bangaren W, Linhart J, Polanco J, Wang F, Wang K, Webster J, Zedler S (2013). “Estimating Parameters in Physical Models through Bayesian Inversion: A Complete Example.” doi:10.1137/100788604.
- Barron A, Schervish MJ, Wasserman L (1999). “The consistency of posterior distributions in nonparametric problems.” *Ann. Statist.*, **27**(2), 536–561. doi:10.1214/aos/1018031206.
- Berger J (1985). *Statistical Decision Theory and Bayesian Analysis*. Springer-Verlag. ISBN 0387960988. doi:10.1007/978-1-4757-4286-2.
- Breidt J, Butler T, Estep D (2011). “A Measure-Theoretic Computational Method for Inverse Sensitivity Problems I: Method and Analysis.” *SIAM Journal on Numr. Anal.*, **49**(5), 1836–1859. doi:10.1137/100785946.
- Bryant CM, Prudhomme S, Wildey T (2015). “Error Decomposition and Adaptivity for Response Surface Approximations from PDEs with Parametric Uncertainty.” *SIAM/ASA Journal on Uncertainty Quantification*, **3**(1), 1020–1045. doi:10.1137/140962632. <http://dx.doi.org/10.1137/140962632>.
- Bui-Thanh T, Ghattas O (2014). “An analysis of infinite dimensional Bayesian inverse shape acoustic scattering and its numerical approximation.” *SIAM Journal of Uncertainty Quantification*, **2**(1), 203–222. doi:<http://dx.doi.org/10.1137/120894877>.
- Butler T, Estep D (2013). “A numerical method for solving a stochastic inverse problem for parameters.” *Ann. Nucl. Energy*, **52**(0), 86–94. doi:10.1016/j.anucene.2012.05.016.
- Butler T, Estep D, Sandelin J (2012). “A Computational Measure Theoretic Approach to Inverse Sensitivity Problems II: A Posteriori Error Analysis.” *SIAM Journal on Numr. Anal.*, **50**(1), 22–45. doi:10.1137/100785958.
- Butler T, Estep D, Tavener S, Dawson C, Westerink J (2014a). “A Measure-Theoretic Computational Method for Inverse Sensitivity Problems III: Multiple Quantities of Interest.” *SIAM/ASA Journal on Uncertainty Quantification*, **2**(1), 174–202. doi:10.1137/130930406. doi:10.1137/130930406, <http://dx.doi.org/10.1137/130930406>.
- Butler T, Estep D, Tavener S, Wildey T, Dawson C, Graham L (2014b). “Solving Stochastic Inverse Problems using Sigma-Algebras on Contour Maps.” doi:arXiv:1407.3851. In preparation.
- Butler T, Graham L, Estep D, Dawson C, Westerink J (2015). “Definition and solution of a stochastic inverse problem for the Manning’s n parameter field in hydrodynamic models.” *Advances in Water Resources*, **78**(0), 60 – 79. ISSN 0309-1708. doi:doi:10.1016/j.advwatres.2015.01.011.
- Butler T, Jakeman J, Wildey T (2018a). “Combining Push-Forward Measures and Bayes’ Rule to Construct Consistent Solutions to Stochastic Inverse Problems.” *SIAM Journal on Scientific Computing*, **40**(2), A984–A1011. doi:10.1137/16M1087229. <https://doi.org/10.1137/16M1087229>.
- Butler T, Jakeman J, Wildey T (2018b). “Convergence of Probability Densities Using Approximate Models for Forward and Inverse Problems in Uncertainty Quantification.” *SIAM Journal on Scientific Computing*, **40**(5), A3523–A3548. doi:10.1137/18M1181675. <https://pubs.siam.org/doi/abs/10.1137/18M1181675>.
- Butler T, Wildey T, Yen TY (2020). “Data-Consistent Inversion for Stochastic Input-to-Output Maps.” *Inverse Problems*. doi:10.1088/1361-6420/ab8f83.

- Calvetti D, Kaipio J, Somersalo E (2014). “Inverse problems in the Bayesian framework.” *Inverse Problems*, **30**(11), 110301.
- Change J, Pollard D (1997). “Conditioning as disintegration.” *Statistica Neerlandica*, **51**, 287–317.
- Cockayne J, Oates C, Sullivan T, Girolami M (2017). *Probabilistic numerical methods for PDE-constrained Bayesian inverse problems*, p. 060001. AIP Publishing. doi:10.1063/1.4985359.
- Cotter S, Dashti M, Stuart A (2010). “Approximation of Bayesian Inverse Problems.” *SIAM Journal of Numerical Analysis*, **48**, 322–345.
- Cui T, Marzouk YM, Willcox KE (2016). “Scalable posterior approximations for large-scale Bayesian inverse problems via likelihood-informed parameter and state reduction.” *Journal of Computational Physics*, **315**, 363–387.
- Dellacherie C, Meyer P (1978). *Probabilities and Potential*. North-Holland Publishing Co., Amsterdam.
- Ernst O, Sprungk B, Starkloff H (2014). *Bayesian Inverse Problems and Kalman Filters*, pp. 133–159. Springer International Publishing, Cham. ISBN 978-3-319-08159-5. doi:10.1007/978-3-319-08159-5_7.
- Fitzpatrick B (1991). “Bayesian analysis in inverse problems.” *Inverse Problems*, **7**(5), 675.
- Gibbs AL, Su FE (2002). “On choosing and bounding probability metrics.” *INTERNAT. STATIST. REV.*, pp. 419–435.
- Harp D, Vesselinov V (2013). “Contamination remediation decision analysis using information gap theory.” *Stoch. Environ. Res. Risk Assess.*, **27**, 159–168.
- Hunter J, Nachtergael B (2001). *Applied Analysis*. World Scientific. ISBN 9789810241919.
- Kennedy MC, O’Hagan A (2001). “Bayesian calibration of computer models.” *Journal of the Royal Statistical Society: Series B (Statistical Methodology)*, **63**(3), 425–464. ISSN 1467-9868. doi:10.1111/1467-9868.00294.
- Marzouk YM, Najm HN, Rahn LA (2007). “Stochastic Spectral Methods for Efficient Bayesian Solution of Inverse Problems.” *J. Comput. Phys.*, **224**(2), 560–586. ISSN 0021-9991. doi:10.1016/j.jcp.2006.10.010.
- Mattis S, Butler T, Dawson C, Estep D, Vesselinov V (2015a). “Parameter estimation and prediction for groundwater contamination based on measure theory.” *Water Resources Research*, **51**.
- Mattis SA, Butler T (2019). “Enhancing piecewise-defined surrogate response surfaces with adjoints on sets of unstructured samples to solve stochastic inverse problems.” *International Journal for Numerical Methods in Engineering*, **119**(10), 923–940. doi:10.1002/nme.6078. <https://onlinelibrary.wiley.com/doi/pdf/10.1002/nme.6078>.
- Mattis SA, Butler TD, Dawson CN, Estep D, Vesselinov VV (2015b). “Parameter estimation and prediction for groundwater contamination based on measure theory.” *Water Resources Research*, **51**, 7608–7629. doi:10.1002/2015WR017295.
- O’Aguilar M Allmaras WB, Tenorio L (2015). “Statistics of Parameter Estimates: A Concrete Example.” doi:10.1137/130929230.
- O’Malley D, Vesselinov V (2015a). “Bayesian-information-gap decision theory with an application to CO₂ sequestration.” *Water Resources Research*, **51**, 7080–7089.
- O’Malley D, Vesselinov V (2015b). “A Combined Probabilistic/Nonprobabilistic Decision Analysis for Contaminant Remediation.” *SIAM Journal on Uncertainty Quantification*, **2**, 607–621.
- Pilosov M (2020). “dissertation.” <https://github.com/mathematicalmichael/thesis>.
- R Walpole R Myers SM, Ye K (2007). *Probability & Statistics for Engineers & Scientists*. Pearson Education. ISBN 9788131715529.

- Silverman B (1986). *Density Estimation for Statistics and Data Analysis*. Chapman and Hall. ISBN 0412246201.
- Smith RC (2013). *Uncertainty Quantification: Theory, Implementation, and Applications*. Society for Industrial and Applied Mathematics, Philadelphia, PA, USA. ISBN 161197321X, 9781611973211.
- Stark PB, Tenorio L (2010). *A Primer of Frequentist and Bayesian Inference in Inverse Problems*, pp. 9–32. John Wiley & Sons, Ltd. ISBN 9780470685853. doi:10.1002/9780470685853.ch2.
- Stuart AM (2010). “Inverse problems: A Bayesian perspective.” *Acta Numerica*, **19**, 451–559. doi:10.1017/S0962492910000061.
- Tarantola A (2005). *Inverse Problem Theory and Methods for Model Parameter Estimation*. siam.
- von Mises R, Doob JL (1941). “Discussion of Papers on Probability Theory.” *Ann. Math. Statist.*, **12**(2), 215–217. doi:10.1214/aoms/1177731750.
- Walsh S (2017). *Simulation-based optimal experimental design: theories, algorithms, and practical considerations*. Ph.D. thesis, University of Colorado, Denver. [Http://digital.auraria.edu/AA00006563/00001](http://digital.auraria.edu/AA00006563/00001).
- Wikle CK, Berliner LM, Cressie N (1998). “Hierarchical Bayesian space-time models.” *Environmental and Ecological Statistics*, **5**(2), 117–154. ISSN 1573-3009. doi:10.1023/A:1009662704779.

APPENDIX A

Proof of Lemma 1

Proof. Let

$$f_N(\lambda) = \sum_{i=1}^N \frac{\eta_N(\mathcal{V}^{(i)})}{\mu(\mathcal{V}^{(i)})} \chi_{\mathcal{V}^{(i)}}(\lambda). \quad (1.0.1)$$

Then, for any $A \in \mathcal{B}_\Lambda$, define

$$\eta(A) = \int_A f_N(\lambda) d\mu. \quad (1.0.2)$$

We verify that η is a probability measure on $(\Lambda, \mathcal{B}_\Lambda)$ and that $\eta(A) = \eta_N(A) \forall A \in \mathcal{B}_{\Lambda, N}$ below:

(i) [Positive] Let $A \in \mathcal{B}_\Lambda$.

$$\begin{aligned} \eta(A) &= \int_A f_N(\lambda) d\mu \\ &= \int \chi_A \sum_{i=1}^N \frac{\eta_N(\mathcal{V}^{(i)})}{\mu(\mathcal{V}^{(i)})} \chi_{\mathcal{V}^{(i)}}(\lambda) d\mu \\ &= \sum_{i=1}^N \left(\frac{\eta_N(\mathcal{V}^{(i)})}{\mu(\mathcal{V}^{(i)})} \int \chi_{A \cap \mathcal{V}^{(i)}}(\lambda) d\mu \right) \\ &= \sum_{i=1}^N \left(\frac{\eta_N(\mathcal{V}^{(i)})}{\mu(\mathcal{V}^{(i)})} \mu(A \cap \mathcal{V}^{(i)}) \right) \geq 0 \end{aligned}$$

(ii) [Definite]

$$\eta(\emptyset) = \int_\emptyset f_N(\lambda) d\mu = \int \chi_\emptyset f_N(\lambda) d\mu = \mu(\emptyset) = 0$$

(iii) [Countably Additive] Let $\{A_k\}_{k=1}^\infty \subset \mathcal{B}_\Lambda$.

$$\begin{aligned} \eta(\cup_k A_k) &= \int_{\cup_k A_k} f_N(\lambda) d\mu = \int \chi_{\cup_k A_k} f_N(\lambda) d\mu \\ &= \int \left(\sum_k \chi_{A_k} \right) f_N(\lambda) d\mu = \sum_k \int \chi_{A_k} f_N(\lambda) d\mu \\ &= \sum_k \int_{A_k} f_N(\lambda) d\mu = \sum_k \eta(A_k) \end{aligned}$$

Finally, let $A \in \mathcal{B}_{\Lambda, N} \subset \mathcal{B}_\Lambda$. Then there exists some $i^* \in \{1, 2, \dots, N\}$ such that $\mathcal{V}^{(i^*)} = A$. We have that

$$\begin{aligned}\eta(A) &= \int_A f_N(\lambda) d\mu = \int \sum_{i=1}^N \left(\frac{\eta_N(\mathcal{V}^{(i)})}{\mu(\mathcal{V}^{(i)})} \chi_{\mathcal{V}^{(i)}} \right) \chi_{\mathcal{V}^{(i^*)}} d\mu \\ &= \int \frac{\eta_N(\mathcal{V}^{(i^*)})}{\mu(\mathcal{V}^{(i^*)})} \chi_{\mathcal{V}^{(i^*)}} d\mu = \frac{\eta_N(\mathcal{V}^{(i^*)})}{\mu(\mathcal{V}^{(i^*)})} \mu(\mathcal{V}^{(i^*)}) \\ &= \eta_N(\mathcal{V}^{(i^*)}) = \eta_N(A).\end{aligned}$$

□

APPENDIX B

ODE Example Revisited

One way by which modelers can improve the quality of parameter estimates is by collecting more data. We consider what would happen if our measurement equipment were able to capture twice as many observations. Furthermore, we verify computationally that using more precise measurement equipment improves the precision of the MUD estimate.

2.1 Different Measurement Equipment

Instead of using equipment that operates at 100Hz, we take 200 measurements every second, resulting in 400 equispaced observations for $t \in (1, 3)$. All other choices involved in the experiment (assumed equipment tolerance, number of trials, parameter samples), are kept the same. We refer to this setup with faster measurement equipment as the “alternative” design.

We show the resulting predictions for the signal using MUD points from twenty repeated trials in Figure 2.1 using the first twenty (middle) and all of the measurements (bottom). The top of the figure shows the solution from the original setup 2.3 for visual comparison. The true signal is well-recovered even with a small subset of the data collected. By the time all measurements are used, the stability of the solutions—with respect to the noise that may have polluted them—is evidenced by the fact that the red lines representing solutions disappear against the backdrop of the true signal in black.

To quantify accuracy and stability of the MUD solutions, we solve the problem for the same choices of S as the original problem (with the addition of $S = 400$). We show the resulting error plots for convergence in the right half of Figures 2.2, juxtaposed against the original experimental design with 100Hz equipment.

The convergence rates are similar (shown in the legend of 2.4), and reduction in uncertainty is almost negligible at a given S . However, we note that in the alternative setup, for an equal number of measurements, the time elapsed is half of that in the original due to the different equipment being used. To this end, we estimate convergence rates with respect to the time elapsed in the experiment rather than number of measurements used, and notice that the alternative setup (orange) exhibits much lower error at a given point of time. This implies that we can achieve similar results with a shorter observational window by using equipment that allows for faster observations.

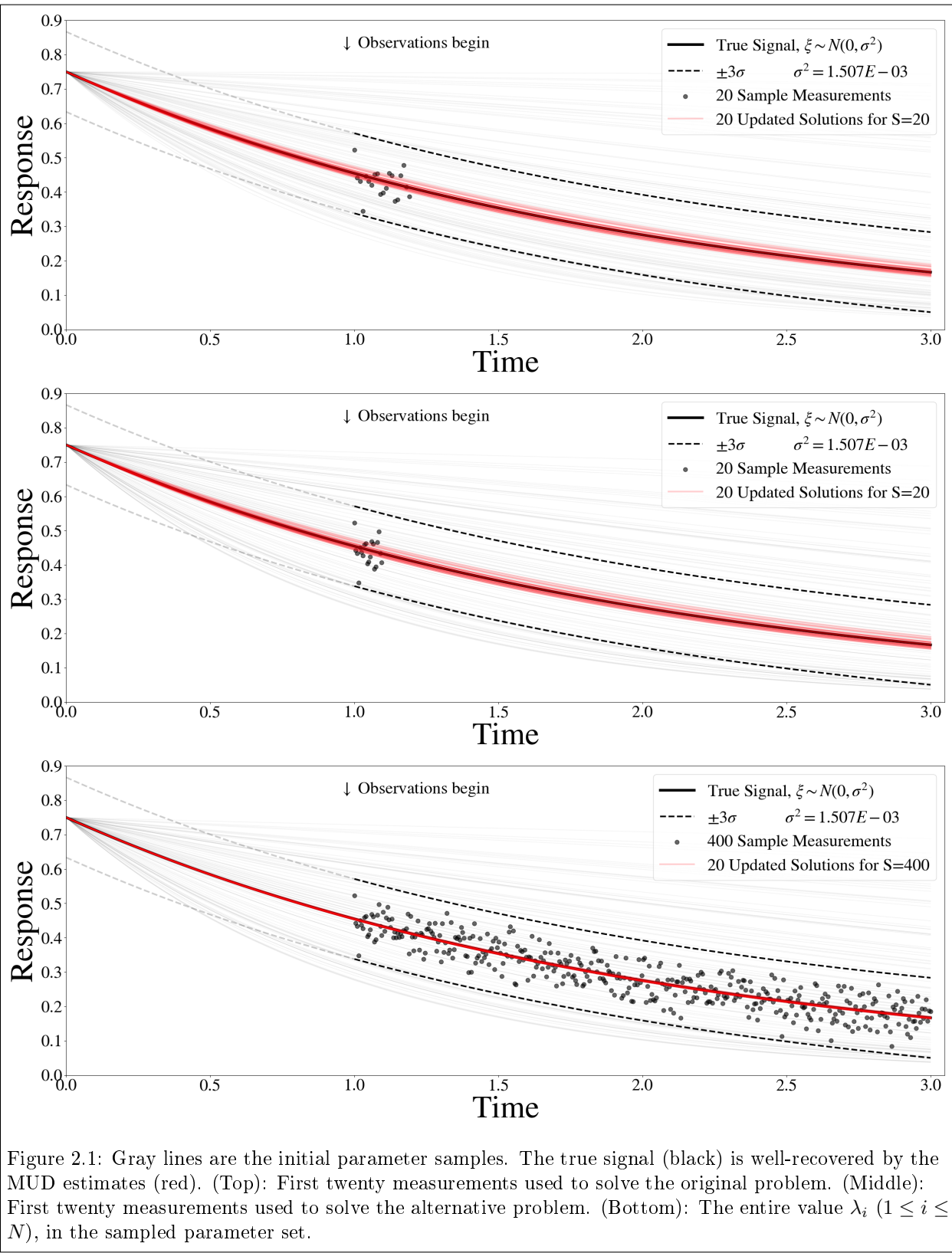


Figure 2.1: Gray lines are the initial parameter samples. The true signal (black) is well-recovered by the MUD estimates (red). (Top): First twenty measurements used to solve the original problem. (Middle): First twenty measurements used to solve the alternative problem. (Bottom): The entire value λ_i ($1 \leq i \leq N$), in the sampled parameter set.

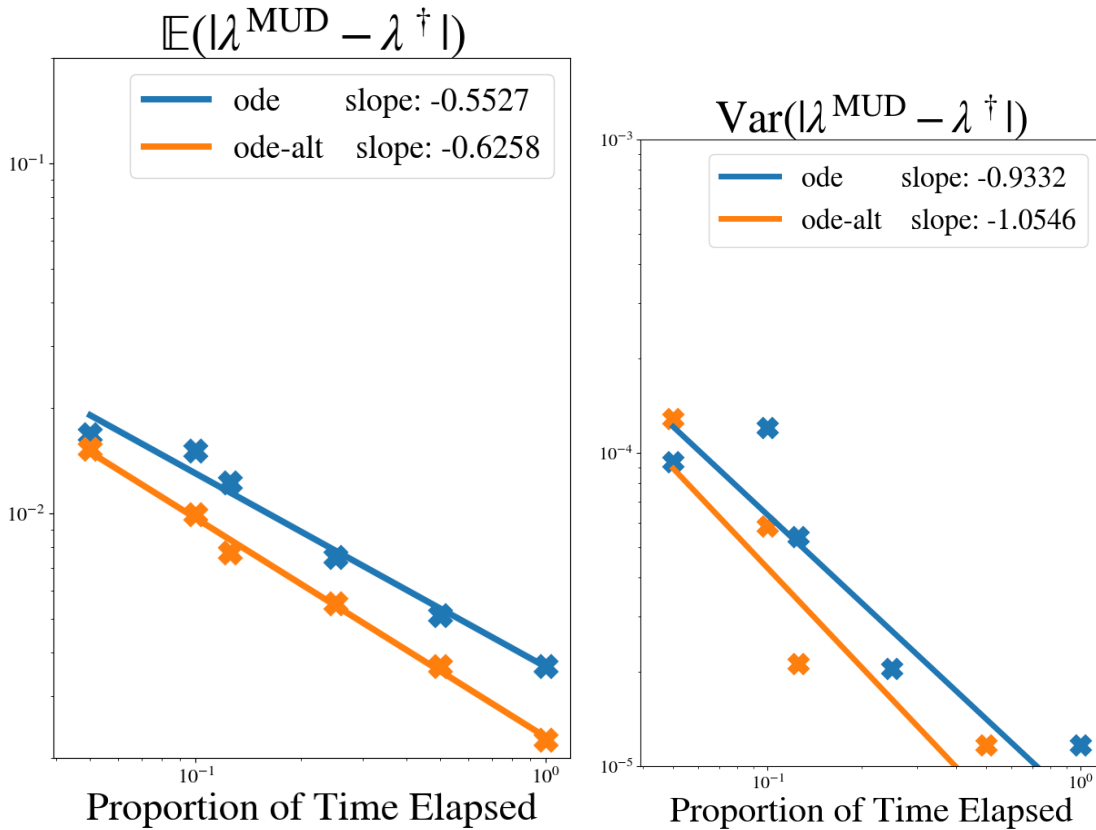


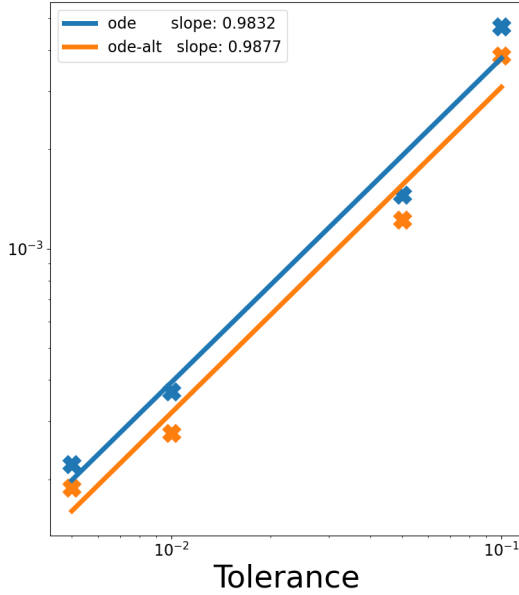
Figure 2.2: Convergence of the MUD point given $N = 1E3$ model evaluations for increasing numbers of observations for randomly placed sensors. Convergence rates are estimated using first-order linear regressions in \log_{10} -space. 100Hz equipment demonstrates a reduction of uncertainty and improvement in precision as S increases towards 200. We observe the same rates of convergence for the alternative equipment and note the (slightly) lower overall error for equal numbers of measurements ($S = 200$ corresponding to $t \in (1, 2)$ in this formulation).

2.1.1 Impact of Equipment Precision

To achieve higher precision in the estimate of the MUD point, one can use more precise measurement equipment. We expect that a method designed to address parameter estimation would see an improvement in accuracy if the data is collected with more precise instruments. Here we show that this is indeed the case for the time-series example introduced earlier by considering choices of $\tau = 0.1, 0.05, 0.01$, and 0.005 for $\mathbb{P}(|\xi| < \tau) = 99\%$ to select our σ in our normal additive noise model. We sequentially incorporate $S = 5, 10, 15, 20, 25, 50, 100$, and 200 measurements and study the error in our estimate of λ^\dagger .

In Figure 2.3, we study the absolute error's mean and variance as our measurement equipment gets more precise (lower tolerance), for both the 100Hz (ode) and 200Hz (ode-alt) variants of sensors we are simulating. In the left half of the figure, we find that the convergence rates for the two designs are

Mean of MUD Error for S=400



Variance of MUD Error
for t=1.375s

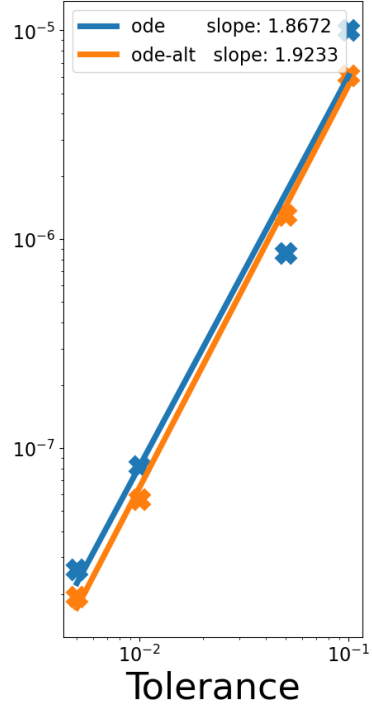


Figure 2.3: Convergence of the MUD point given $N = 1E3$ model evaluations incorporating measurements at a fixed point in time. As more precise measurements are incorporated, the accuracy and precision of the MUD solution improves.

nearly identical but the equipment which records twice as many measurements has a persistent reduction in error. The right half shows the convergence in variance of the absolute error, and the vertical displacement between the two designs is visually difficult to distinguish. However, as evidenced in the legend annotations of Fig 2.3, the alternative design (faster equipment) exhibits an increase in the rate of convergence from 1.87 to 1.92.

We have shown that the Data–Consistent approach to solving parameter identification problems manages to generalize to problems involving time-series data from a single Quantity of Interest. We now turn our attention to an example where instead of temporal measurements, we incorporate spatial data to solve another 1-D parameter identification problem.

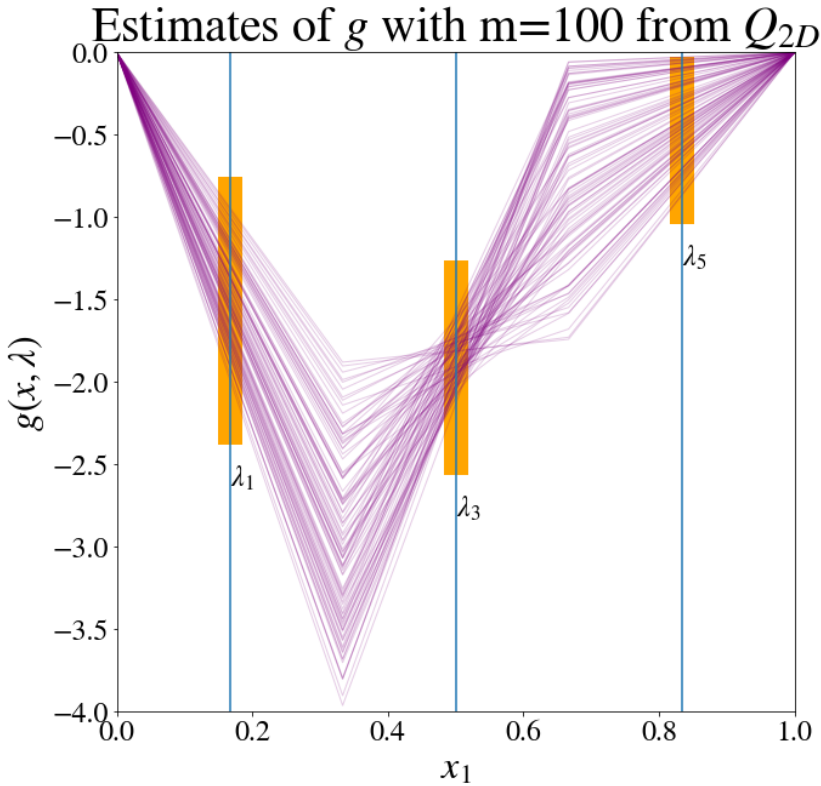


Figure 3.1: Knowledge of the behavior of g at the boundaries allows for more than half of each of the three remaining intervals in five dimensions to be ruled out as infeasible regions when we look at high-probability samples from the 2-D SIP solution.

APPENDIX C

Description of Alternative 5-D Initial Density

In Figure 3.1, we plot the parameter samples whose relative ratios exceeded 1/1000 and note that they sweep out a family of curves that can be used to estimate bounds not only on λ_2 and λ_4 (the previous λ_1 and λ_2 from the 2-D problem)—which exhibit correlation structure—but also on the remaining three knots. To form the intervals shown in orange in Fig. 3.1, we take the upper and lower bounds of the curves passing through the vertical lines drawn at the three new knot values. To be conservative, we multiply our lower bound by 1.2 and the upper by 0.8. With these choices, we are still more than halving the interval-length in each direction as compared to the previous 5-D problem. One could establish a lower tolerance for accepting likely samples and avoid the multiplication factor, or make any number of other choices for a refined initial density. However, a thorough exploration of how to best leverage the ratio of observed to predicted densities is left to future work, and will always be highly problem-dependent.

For the two remaining directions, we want to capture the correlation structure that we were able to visually identify in Fig. 4.6 and impose a uniform density over the support of the set. To achieve this

desired refinement of an initial density, we perform a singular-value decomposition on the likely samples from the scalar-valued 2-D solution, since there are so many more samples⁷. The singular vectors are used to transform the vector-valued samples, and a uniform sampling is performed over the rectangular bounding box for these points, shown in the center of Figure 3.2. These generated samples, however, leave Λ when transformed back to their native space, as seen in the left panel. To ameliorate this problem, we instead perform sampling in a while-loop, sampling from this uniform box and rejecting any that would get mapped back outside Λ , until we reach our desired thousand samples.

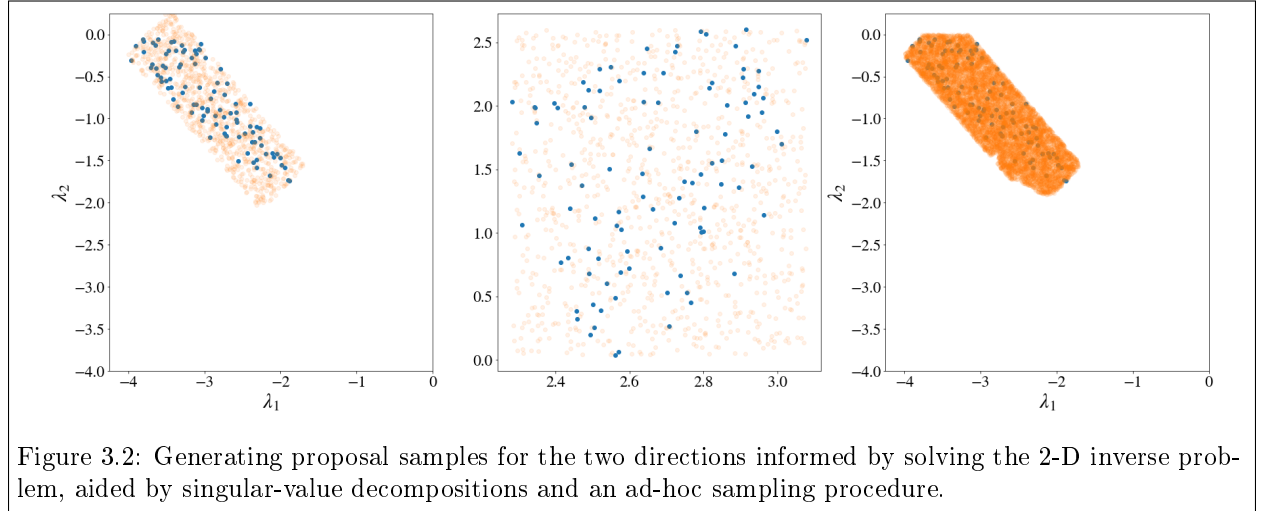


Figure 3.2: Generating proposal samples for the two directions informed by solving the 2-D inverse problem, aided by singular-value decompositions and an ad-hoc sampling procedure.

Analogously speaking, we set out to define a computational open cover for the relatively high-probability samples. In the center panel of Fig 3.2, there are corner-regions of the space we want to avoid wasting samples on as well, so we reject samples that have squared two-norm greater than 0.05 from their nearest vector-valued sample. This sampling procedure produces the set shown in orange on the right side of the figure (ten thousand shown to demonstrate coverage). One thousand of these samples are kept at random and joined with the samples generated from the three other directions.

⁷The scalar-valued contour was found to better characterize the direction of the equivalence class, suggesting perhaps a justifiable use for solving the problem with it. We could have formed an estimate of the updated density from using the vector-valued QoI and sampled from that instead. Many such approaches can be looked into in the future and are briefly discussed in the last section of this chapter.